# THÈSE POUR OBTENIR LE GRADE DE DOCTEUR DE L'UNIVERSITÉ DE MONTPELLIER

**En Physique**

**École doctorale : Information, Structure, Systèmes**

**Unité de recherche UMR 5221**

# Défauts dans le silicium : vers une nouvelle plateforme pour les technologies quantiques


**Présentée par Yoann BARON**
**Le 14 décembre 2022**

**Sous la direction de Guillaume CASSABOIS et Anaïs DRÉAU**


**Devant le jury composé de**

| | |
|---|---|
| Nicolas CHAUVIN, Chargé de recherche, INL - Lyon | Rapporteur |
| Christophe COUTEAU, Chargé de recherche, L2N UTT - Troyes | Rapporteur |
| Éric TOURNIÉ, Professeur, IES - Montpellier | Président |
| Jean-Sébastien LAURET, Professeur, LuMIn - Paris-Saclay | Examinateur |
| Hanna LE JEANNIC, Chargée de recherche, LKB - Paris | Invitée |
| Loic RONDIN, Maître de conférences, LuMIn - Paris-Saclay | Invité |
| Anaïs DRÉAU, Chargée de recherche, L2C - Montpellier | Co-encadrante de thèse |
| Guillaume CASSABOIS, Professeur, L2C - Montpellier | Directeur de thèse |

UNIVERSITÉ DE MONTPELLIER

# Remerciements

Il n'est pas particulièrement facile, du moins pour moi, de partager et de décrire l'appréciation que l'on peut avoir pour des individus, mais c'est un exercice auquel je vais m'essayer à travers ces remerciements.

Je tiens à remercier mes deux directeurs de thèse, Anais Dréau et Guillaume Cassabois, pour (entre autres) leur gentillesse, leur patience et leur vaste apport scientifique qui m'ont permis de passer trois superbes et enrichissantes années de thèse. J'étends ces remerciements au reste de l'équipe du S2QT, à commencer par les autres membres permanents du groupe : Bernard Gil, Isabelle Philip, Pierre Valvin, Vincent Jacques et Aurore Finco. Être dans cette équipe, c'est travailler chaque jour avec des personnes pleines de passion, de partage (avec beaucoup de goûters) et d'humour. Petite mention à Pierre qui a su nous partager son enthousiasme pour l'astrophysique, avec ses superbes observations de la voûte céleste.

Je tiens aussi à remercier tous les doctorants avec lesquels j'ai travaillé au cours de ces trois dernières années. En particulier Alrik Durand, avec qui j'ai eu la chance de partager l'étude des défauts ponctuel dans le silicium, mais aussi les deux compères bretons Maxime Rollo et Florentin Fabre, ainsi que l'éminent responsable du journal club Adrien Rousseau. Également Angela Haykal, Rana Tanos et Christine Elias, qui ont su apporter toute la saveur du Liban dans l'équipe, les post-doctorants Pawan Kumar et Zhao Mu, ainsi que la nouvelle vague, Juliette Plo, Tristan Clua-Provost, Elias Sfeir et Felix Cache.

Cette thèse n'aurait pas été possible sans l'aide de nos nombreux collaborateurs. En premier lieu, Jean-Michel Gérard au CEA Grenoble pour ses simulations concernant l'émission des différents défauts étudiés dans cette thèse et les précieux échantillons de silicium purifié. Tobias Herzig et Sébastien Pezzagna de l'université de Leipzig pour la création par implantation des défauts ponctuels. Marco Abbarchi de l'université de Marseille pour son aide avec le recuit flash. Enfin, Adam Gali et Péter Udvarhelyi de l'université de Budapest pour la modélisation théorique des centres G et W ainsi que les nombreux échanges.

Mes remerciements vont également à Nicolas Chauvin, Christophe Couteau, Éric Tournié, Jean-Sébastien Lauret, Hanna Le Jeannic et Loïc Rondin pour m'avoir fait l'honneur de participer au jury de soutenance de ma thèse. Je remercie Éric Tournié d'avoir présidé ce jury, ainsi que Nicolas Chauvin et Christophe Couteau d'avoir accepté d'en être les rapporteurs.

Parmi toutes les personnes du L2C, je tiens particulièrement à remercier Christian Lhenoret et Thomas Cohen de l'atelier mécanique, Laurent Nehlig pour le support informatique, et

les nombreuses personnes qui ont soutenu mes activités, notamment Béatrice Tomberli, Jean-Christophe Art et Stéphanie Martegoutes.

Enfin, je voudrais terminer en adressant mes remerciements éternels à ma famille pour leur soutien indéfectible.

# Contents

**Contents** ii

**Introduction** 1

**1 Silicon for quantum technologies** 5
- 1.1 The Silicon crystal . . . 5
  - 1.1.1 Properties of intrinsic silicon . . . 6
  - 1.1.2 Defects in silicon . . . 9
  - 1.1.3 Silicon industrial grade nanofabrication technologies . . . 12
- 1.2 The Silicon platform for quantum applications . . . 14
  - 1.2.1 Electrical qubits . . . 15
  - 1.2.2 Photonic qubits . . . 17
- 1.3 Electron qubits with photonic interfaces . . . 18

**2 Single near-infrared emitters in carbon-implanted silicon** 23
- 2.1 Experimental set-up . . . 24
  - 2.1.1 Low temperature confocal microscope . . . 24
  - 2.1.2 Hanbury Brown and Twiss set-up and autocorrelation function $g^{(2)}(\tau)$ . . . 28
- 2.2 Isolation of single photon emitters . . . 30
  - 2.2.1 Spectral identification of seven families of defects . . . 30
  - 2.2.2 Demonstration of single photon emission . . . 35
- 2.3 Emission properties of single defects . . . 38
  - 2.3.1 Zero-phonon line dispersion between defects . . . 39
  - 2.3.2 Photostability and saturation curves . . . 40
  - 2.3.3 Polarization of the single photons . . . 44
  - 2.3.4 Excited-level lifetimes . . . 46

**3 Creation and detection of single G centres** 49
- 3.1 The G centre in silicon . . . 50
  - 3.1.1 Optical properties . . . 50
  - 3.1.2 Microscopic structure . . . 52
  - 3.1.3 Electronic level structure . . . 54
- 3.2 Single G centres creation by ion implantation . . . 56

3.2.1 Sample fabrication and analysis before the implantation process . . . . . 56
3.2.2 From ensembles to single defects . . . . . 59
3.3 Investigating the photon emission of single G centres . . . . . 64
3.3.1 Single G centre photophysics . . . . . 65
3.3.2 Defect reorientation inferred from the polarization diagram . . . . . 67
3.3.3 Fine structure in the zero-phonon line . . . . . 72
3.4 Conclusion . . . . . 74

**4 Creation and detection of single W centres** **75**
4.1 The W centre in Silicon . . . . . 76
4.1.1 Optical properties of ensembles of W centres . . . . . 76
4.1.2 Microscopic structure . . . . . 77
4.1.3 Electronic level structure . . . . . 79
4.2 Creation of single W centre by ion implantation . . . . . 80
4.2.1 Investigation of the implanted areas . . . . . 80
4.2.2 Detection of single W centres outside the implanted areas . . . . . 82
4.3 Study of W centres at single defect scale . . . . . 84
4.3.1 Investigation of the ZPL of single W centres . . . . . 84
4.3.2 Orientation of the emission dipole of W centres . . . . . 87
4.3.3 Photostability . . . . . 88
4.4 Photodynamics of individual W centres . . . . . 89
4.4.1 Excited state lifetime . . . . . 89
4.4.2 Evolution of the $g^2(\tau)$ function with laser power . . . . . 90
4.4.3 Saturation curves . . . . . 92
4.5 Conclusion . . . . . 95

**Conclusion** **95**

**Bibliography** **99**

**Abstract** **113**

# Introduction

At the beginning of the 20's century, a new physics field has emerged, quantum mechanics, which changed radically science and technology. It was the beginning of the first quantum revolution that would lead to the invention of the laser, the transistor or atomic clocks. In the 1980s, new ideas were pioneered by physicists such as the 2022 Nobel Prize in Physics, Alain Aspect, John Clauser, Anton Zeilinger and their historical experiment on entanglement and non-locality of photons [1, 2], or Richard Feynman and his seminal paper "Simulating Physics with Computers" [3], introducing the notion of a quantum computer. The progress of research and technology allowed to isolate the first quantum systems [4]. This was the beginning of the second quantum revolution, which created a new field, quantum technologies, aiming at exploiting the properties of quantum mechanics to design and build innovative devices.

### Quantum technologies

Among the quantum mechanics properties, there is the phenomenon of quantum entanglement, which allows the state of two or more of quantum objects to share correlations, even when these objects are far apart. It envisioned new applications in the field of quantum communication, which aims at transmitting information over large distances in a secure manner. In particular, new methods of quantum cryptography are being investigated to achieve in the long term the safety of remote communications, in contrast to classical cryptography methods which could be broken by mathematical progress or increase of computation power.

Applications using quantum entanglement are not limited to quantum communications. By analogy to classical bits of information, a quantum bit (qubit) represents the smallest unit to encode quantum information. It consists of a two-level quantum system whose state can be initialised, coherently manipulated and measured. Typical physical qubits are atoms, photons [5], ions [6], superconducting microcircuits [7], quantum dots [8] or point defects in semiconductors [9, 10]. Quantum computing aims to develop large cluster of entangled qubits in order to develop calculation methods that are exponentially more powerful than those used in conventional computers. However, to benefit from this exponential advantage, an immense technological leap would be necessary to move from the about a hundred of entangled qubits currently available [7] to hundreds of thousands of physical qubits. Another application is quantum sensing, which aims to measure physical quantities with unprecedented sensitivity and/or resolution.

### Quantum communications

*Single photon generation*:

Quantum communications aim to send qubits carrying quantum information over large distances. To do this, the preferred medium is the photon, which allows information to be encoded on observables such as the polarisation, frequency or time-bin. Photonic qubits can be generated by single emitters [10] or using non linear optical processes [11]. This is different from fibre-optic telecommunication protocols, where classical information is carried by the modulation of laser light containing several thousand photons. The specific needs of quantum communications have stimulated the development of new optoelectronic components capable of emitting or detecting a single photon almost perfectly. Ideal single photon sources must emit a photon at the chosen time (on-demand), with high purity (no noise or multi-photon events) and efficiency. In addition, one approach to generate a single photon is to exploit the spontaneous emission from an isolated single atom. After the excitation of an atom from its ground state (GS) to its first excited state (ES), for example using a laser pulse, it spontaneously relaxes back to its GS by emitting a single photon. As it is difficult to manipulate individual atoms, a more practical solution is to use solid 'artificial atoms', which mimic their properties, such as individual fluorescent defects embedded into a semiconductor, here silicon.

*Quantum networks*:

The construction of quantum networks, allowing the generation, distribution, manipulation, storage and processing of quantum information, is also being developed with secure communications protocols using individual qubits or pairs of entangled qubits [12]. A secure link over 300 km of optical fibre was recently demonstrated in Geneva [13]. However, this method can currently only work over distances of a few hundred kilometres in the absence of secure repeaters. To make quantum networks more efficient and to extend quantum communication distances, it is necessary to design these devices, making it possible to teleport and store photonic entangled states between two distant locations, and then to synchronise the re-emission of photons. The nodes in the quantum network are either generation stations (sources of single photons or entangled photons), measurement stations or information storage stations. More specifically, quantum memories allow qubits to be stored without revealing or degrading the information they carry, and ideally with very good write and read efficiency. These devices are usually based on a material support, for example, crystals doped with ground-rare ions, atomic vapours at room temperature, cold atoms or artificial atoms.

In the field of quantum communications, there are promising prospects for artificial atoms based on fluorescent defects in semiconductors. The most advanced optically active defects for quantum technologies are currently in diamond [14] and SiC [10]. In this manuscript, however, we will explore these artificial atoms in the key material of microelectronics: silicon.

### Fluorescent defects in silicon for quantum technologies

Silicon is the dominant material in the semiconductor industry. It is the most widely used semiconductor in microelectronics, mainly due to its nanoscale integration, doping control and silicon crystal growth process. The latter has been developed so intensively that today many manufacturers are able to produce very pure (over 99.99999999 %) single-crystal silicon wafers on surfaces of 300 mm (and even up to 450 mm).

Silicon is an indirect bandgap semiconductor. In the near infrared, it absorbs visible light efficiently resulting in the development of the silicon photovoltaic industry and also commercial CCD cameras [15]. Silicon photonics is also well developed, with the creation of integrated photonic components, such as waveguides. Thus silicon benefits from advanced nano-manufacturing processes in optoelectronic. Despite all these qualities, the use of silicon to emit light is limited by the indirect nature of the silicon bandgap. However, artificial atoms embedded in the silicon lattice can serve as light sources.

Point defects can be made of vacancies, impurities or interstitial atoms in the crystal lattice. Among these defects, some are fluorescent with the ability to emit light upon appropriate excitation. They are called colour centres and behave like artificial atoms. As stated previously, individual optically active defects could be used as single photon source for applications in quantum cryptography and quantum communications. In addition, some of these fluorescent defects possess a non-zero electron spin whose magnetic resonance can be detected optically. This spin degrees of freedom of the defect is an additional quantum resource that can be used to locally encode, store and process quantum information [16].

### Thesis outline

The aim of this thesis is to study individual fluorescent defects in silicon in the context of quantum technologies and to examine their potential as single photon sources in silicon-based devices. In particular, the G centre, an isovalent carbon-related impurity, is expected to be a promising candidate for single photon emitters and spin qubit due to: (i) Its emission around 1.3 $\mu$m matching the telecommunication O-band spreading between 1260 to 1360 nm [17]. (ii) A fast radiative recombination time of roughly 6 ns [18]. (iii) The presence of a metastable electron spin triplet (S=1) evidenced by optically-detected magnetic resonance (ODMR) measurements performed on ensembles [19,20] that could allow optical spin control. The analysis of this defect led to the investigation of silicon- and carbon-implanted samples, which in turn led to the study of multiple carbon-related centres and of an intrinsic defect, the W centre.

The first chapter will aim at presenting silicon in the context of quantum technologies. In this chapter, we will look at several aspects. First, we will present the crystallographic, electronic and phononic properties of the silicon crystal. Then we will introduce the notion of defects in silicon and discuss the different use of the silicon substrate in the semiconductor industry. The second part will address the different quantum qubits in the silicon platform. Lastly, fluorescent defects in silicon with potential for quantum applications will be introduced.

The second chapter will cover the discovery of multiple near-infrared single emitters in

carbon-implanted silicon. First, we will present the experimental setup: a low-temperature confocal microscope optimised for the detection of single emitters in the near-infrared with optical excitation above the silicon bandgap. This set-up will allow the isolation of six unidentified single photon emitters in silicon, that will be explored in the second part. Lastly, their spectral properties, single photon emission properties and photodynamics will be analysed in the third part.

The third chapter will focus on the creation and detection of single G centres. After an introduction on the optical, microscopic and electronic properties of this carbon defect, the creation of single G centres by ion implantation will be demonstrated in thin silicon-on-insulator sample in the second part. In the third part, the photon emission of single G centres will be investigated and will allow to demonstrate a reorientation of the defect under optical excitation.

The fourth chapter will focus on an intrinsic defect in silicon, the W centre, in a silicon implanted sample. The optical, microscopic and electronic properties of this interstitial complex will be presented in the first part. In the second part, the first optical isolation of the W centre will be demonstrated in a silicon implanted sample. In addition to spectroscopic studies, single W centre photostability and polarisation will be studied in the third part, with the latter revealing insights on the microscopic structure of the defect. Lastly, the photodynamics and the power dependence of this defect are investigated in the fourth part.

Chapter 1

# Silicon for quantum technologies

Contents


**1.1 The Silicon crystal . . . . . 5**
1.1.1 Properties of intrinsic silicon . . . . . 6
1.1.2 Defects in silicon . . . . . 9
1.1.3 Silicon industrial grade nanofabrication technologies . . . . . 12
**1.2 The Silicon platform for quantum applications . . . . . 14**
1.2.1 Electrical qubits . . . . . 15
1.2.2 Photonic qubits . . . . . 17
**1.3 Electron qubits with photonic interfaces . . . . . 18**


Silicon has enabled a technological revolution with the development of transistors and the rise of the microelectronics industry. It is the dominant material in the semiconductor industry, and is undoubtedly the most important material of our Information Society. In this thesis, we explore a different approach to conventional technologies, and we study single fluorescent point defects embedded within the silicon matrix to obtain quantum light sources.

In the first section, we will recall the intrinsic properties of silicon that have played an important role in its use for classical applications, with an emphasis on point defects. Silicon holds promises for quantum applications as a host for electron and photon qubits, which will be discussed in the second section. Finally, in the last section, we review the promising fluorescent defects in silicon for quantum applications.

## 1.1 The Silicon crystal

The presence of point defects in silicon has historically been detrimental to microelectronics, due to their tendency to capture electrons, thereby reducing electrical conductivity. Their use as light sources is a recent approach that is gaining interest, as evidenced by the first detection of an individual fluorescent defect in silicon [21]. To understand how the presence of point defects in the silicon crystal gives rise to near infrared quantum light sources, the intrinsic properties of the silicon crystal will be described in the first section, followed by the electronic properties of point defects in the silicon lattice in the second section, as well as fluorescent defects. Lastly, the nanofabrication technologies (inherited from the semiconductor industry) that enable the creation, scalability and optimisation of fluorescent defects in silicon, namely defect engineering and integrated photonics, will be introduced in the third section.

### 1.1.1 Properties of intrinsic silicon

In this section, we start by outlining the silicon crystal structure. Then the electronic properties as well as the phononic properties, related to the photoluminescence (PL) in silicon, will be described.

#### Crystal structure

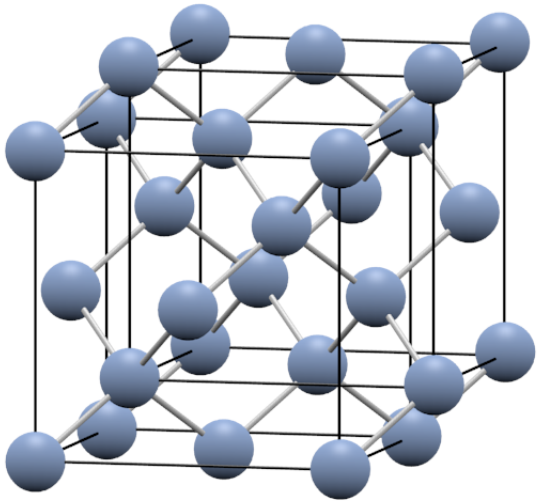

**Figure 1.1:** Silicon crystal structure in real space. The blue spheres are silicon atoms and the gray lines are the tetrahedral bonds. The black lines are guides to the eyes to display the two cubic lattices.

The silicon atom is represented by the symbol Si and has the atomic number 14. Silicon atoms in their neutral form possess four valence electrons. These four electrons form covalent bonding with other nearby silicon atoms by $sp^3$ hybridization, resulting in a tetrahedron geometry. This atomic organization results in the silicon crystal possessing a diamond structure. This crystal structure is displayed in figure 1.1 as two face-centered cubic lattices offset by a quarter of the major diagonal from one another. In this configuration, the lattice parameter is equal to a = 5.43 Å, corresponding to a distance between two neighboring atoms of 2.35 Å. Thus the atomic density of the silicon crystal is very close to $5 \times 10^{22}$ atoms/cm$^3$ [22].

By assuming a "hard-sphere" model for the silicon atoms, we find that the tetrahedral covalent radius of the silicon atom is 1.18 Å. This means that around 34 % of the silicon lattice is occupied by atoms, making the silicon lattice a loosely packed structure which allows incorporation of impurities [22]. The role of these impurities (or defects) is central in the engineering of the silicon crystal as a platform in classical applications (section 1.1.2) but also more recently in quantum applications (sections 1.2 and 1.3).

### Electron properties

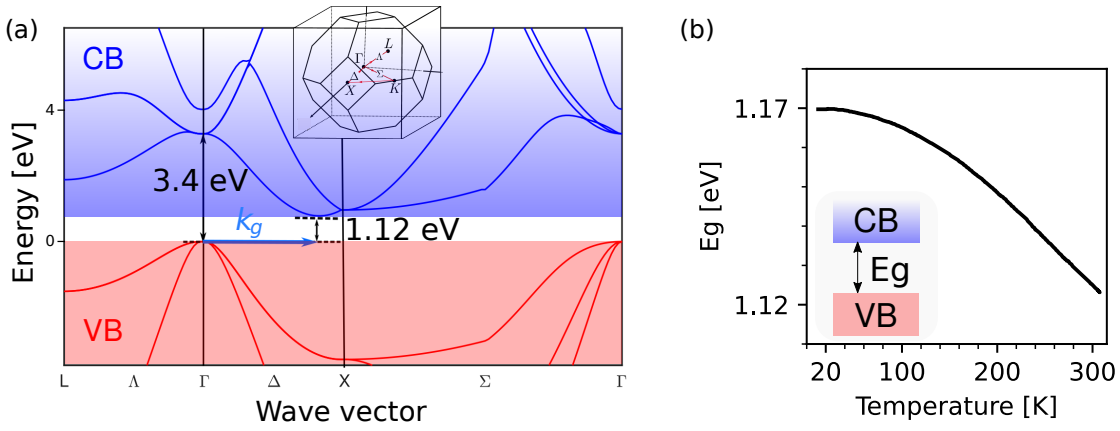


**Figure 1.2:** (a) Calculated electronic band structure of silicon adapted from [23]. VB: Valence band (in red), CB: Conduction band (in blue). The zero energy is defined as the maximum of the valence band. Inset: First Brillouin zone (FBZ) with the high symmetry points and lines indicated in black and red respectively. (b) Silicon bandgap energy as a function of temperature [24].

In a crystal, the accessible electronic energy levels are described by the band structure. These bands result from the hybridization of the atomic orbitals of the atoms of the crystal. Figure 1.2(a) displays the electron energy dispersion curves in silicon, that is the energy of an electron as a function of its wavevector $\mathbf{k}$ limited to the FBZ (displayed in inset). The valence band maximum corresponds to a wavevector $k = 0$ ($\Gamma$ point), and for the same wavevector, it is separated from the conduction band by a direct bandgap of 3.4 eV. However, the conduction band minimum corresponds to $k_g$ at 85 % along the $\Gamma$-X high symmetry line, close to the X valley, with a value $k_g = 4.1{\times}10^9$ m$^{-1}$ [25]. Thus, silicon is an indirect bandgap semiconductor of energy $E_g = 1.12$ eV at ambient temperature, corresponding to the difference between the conduction band minimum and the valence band maximum.

This indirect bandgap evolves with temperature, as seen on figure 1.2(b). It decreases with increasing temperature, from 1.17 eV at cryogenic temperature to reach a value of 1.12 eV at room temperature (T = 300 K). The working temperature regime in this manuscript is below T = 30 K, with most measurements being performed at T = 30 K, and for these temperatures the value of the indirect bandgap can be considered constant.

In a direct bandgap material, PL is generated by the radiative recombination of a photo-excited electron in the conduction band into the valence band. This transition produces a photon with an energy close to the bandgap. In silicon, the bandgap is indirect with $E_g = 1.12$ eV as stated previously. PL generated by the direct electron-hole recombination is close to nonexistent, as the direct bandgap is significantly higher than the indirect one, implying that the electrons and holes relax to the conduction band minima and valence band maxima. The PL in silicon is therefore generated, slightly below the indirect bandgap, by indirect transitions assisted by phonons for wavevector conservation. The phonon-assisted recombination of a free-

exciton occurs with a lifetime close to 200 $\mu$s (at T = 1.8 K [26]), much longer than non-radiative electron-hole recombination processes. This is what makes pure silicon a poor light emitting medium [27].

### Phonon properties

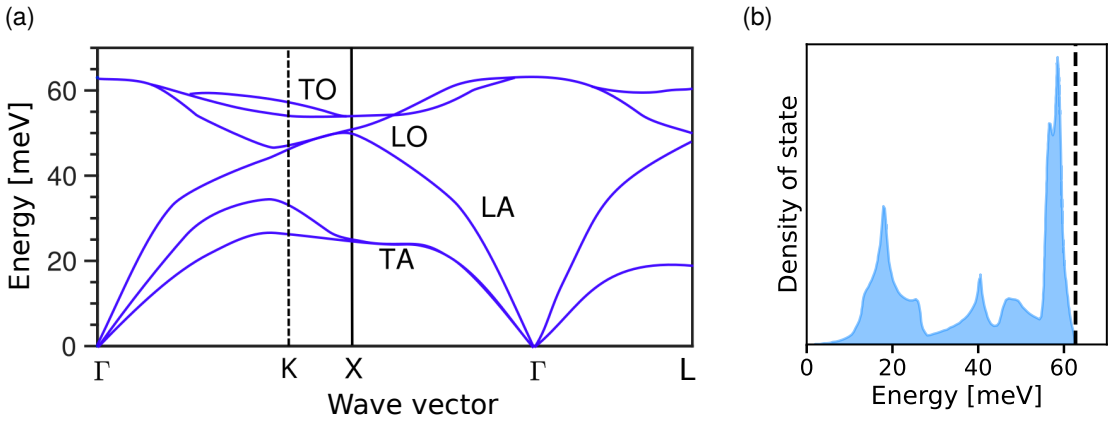


**Figure 1.3:** (a) Phonon dispersion curve from [23]. Γ is the center of the FBZ and X, L and K are at the edges of the zone. (b) Calculated phonon density of states at T = 300 K from [28]. The dashed line represents the maximum phonon energy at 62.7 meV.

The phonon dispersion curves at room temperature (T = 300 K) are plotted in figure 1.3(a). From this dispersion relation, the associated phononic density of states (DOS) can be obtained and is plotted in figure 1.3(b). We note the presence of two maxima located at energies of 20 meV and 60 meV which are respectively related to the TA (transverse acoustic) and TO/LO (transverse/longitudinal optic) phonon modes.

For the PL emitted by defects embedded in the silicon lattice that will be studied in this manuscript, phonons will participate in the PL process. Thus, the comparison of the density of phonon states with the PL of these defects can give information on the symmetry of the defects. In silicon, the maximum energy that a phonon can have is 62.7 meV (dotted line in figure 1.3(b)). Thus, the PL emitted by a defect above this energy may be related to local vibrational modes (LVM), thus helping in the identification of specific defects. We add that LVMs can also be present below the maximum phonon energy.

From this review of the intrinsic properties of silicon, the study and use of silicon as a platform for optical emission applications seems unsuitable. The engineering of defects in silicon developed in the semiconductor industry to control its conductivity opens new prospects in optoelectronics. Indeed, the presence of defects in the silicon lattice can modify locally the electronic structure, to allow a local direct electron-hole radiative recombination. The next section aims at presenting these defects.

### 1.1.2 Defects in silicon

In the previous section, the impact of defects on the electronic and light-emission properties of their host matrix was briefly discussed. However, the definition of a defect has not yet been given. In this section, we discuss the structure of extended and point defects.

#### Extended defects

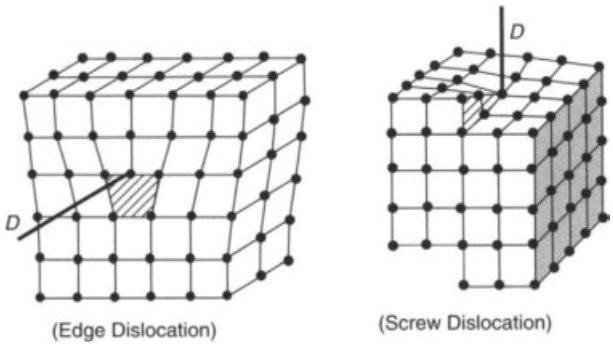


**Figure 1.4:** Two types of dislocations in a cubic lattice, the edge dislocation on the left and screw dislocation on the right, from [29].

Extended defects are irregularities in a crystal lattice that abruptly change the arrangement of atoms. They can be 3D, such as micropipes, 2D, such as grain boundaries or 1D such as line defects or dislocations. In the growth of mono-crystals, the formation of these defects has to be prevented to avoid semiconductor device failure.

The simplest extended defects in silicon crystal growth are dislocations. There are two main dislocation geometries. The first one is edge dislocation which can be depicted as inserting an additional extra row of atoms into the crystal structure (see figure 1.4(a)). The second one is screw dislocation, which can be seen as one atomic plane getting mixed into two atomic ones (see figure 1.4(b). Dislocations have a size of the order of a micrometer.

#### Point defects

Crystallographic structure:

In opposition to dislocations, which are defects spreading over multiple lattice sites, defects can be spatially restricted to one or a few lattice sites. These defects are called point defects and they can be either intrinsic or extrinsic. For a silicon lattice, the simplest intrinsic defect corresponds either to the absence of a silicon atom, called a vacancy (figure 1.5(a)), or to the presence of an additional silicon atom in an interstitial site, i.e. a self-interstitial defect (figure 1.5(b)). An extrinsic defect is made of at least one impurity atom that can be either on a substitutional site (figure 1.5(c)) or on an interstitial site (figure 1.5(d)). Typical impurities can

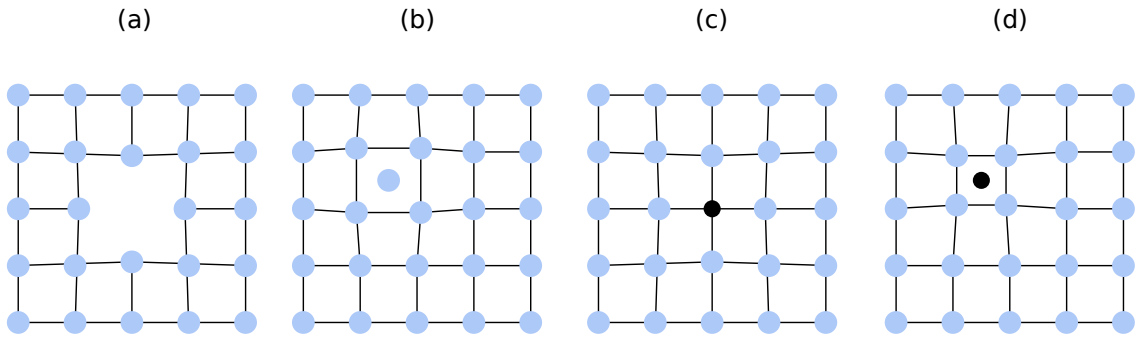


**Figure 1.5:** Representation of the simplest point defects in silicon. The blue spheres are the silicon atoms, and in black the impurities. The lattice in the background represents the sites occupied by the silicon atoms. The different defects are in the order (a) vacancy, (b) self-interstitial, (c) substitutional and (d) interstitial.

be for instance either boron or phosphorus when one wants to achieve p or n doping, respectively (see next section), or any other atomic species such as carbon or oxygen.

All these elementary defects can form complexes. The number of possible combinations of atoms to form these complexes is tremendously high, leading to a vast number and diversity of centers. We can mention for example the G center, which is a complex made up of 2 substitutional carbon atoms with an interstitial silicon atom, as well as the W center which is constituted of 3 interstitial Si atoms. Both defects will be studied in this manuscript in chapter 3 and 4, respectively.

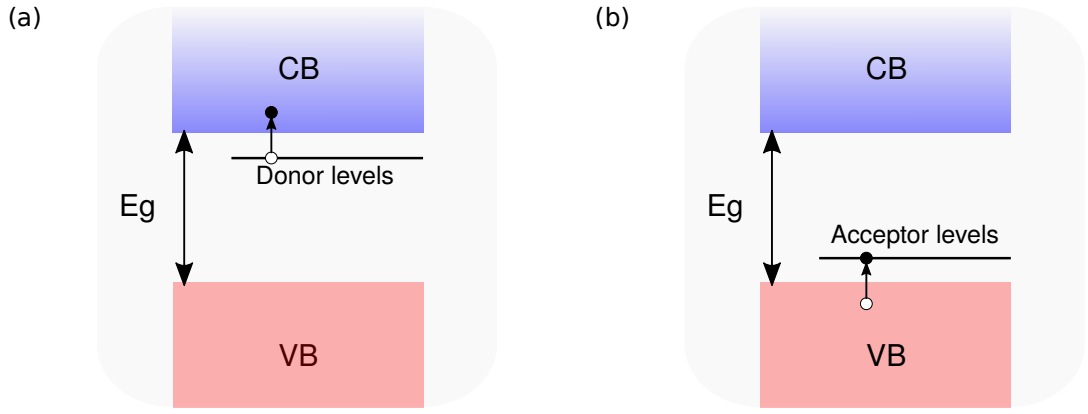


**Figure 1.6:** Energy level scheme for extrinsic semiconductors: (a) n-type and (b) p-type.

Electronic structure:

Point defects impact locally the atomic structure of the crystal, thus inducing a local modification of the electronic wave functions. This results in the introduction of levels in the band

structure, that can be localized inside the bandgap. This property is notably exploited for doping (see section 1.1.3) to increase the electrical conductivity in semiconductors, with defects introducing levels near the CB or VB.

For negative charge carriers, pentavalent impurities (i.e. Group V elements such as phosphorus, arsenic or antimony) are incorporated to have an excess of electrons, hence their name of "donors". These donor impurities introduce new energy levels in the bandgap called donor levels which are close to the conduction band minimum, as displayed in figure 1.6(a). These levels are filled with electrons at low temperature, consequently favoring their excitation in the conduction band by ionization at room temperature, and thus contributing to the extrinsic conductivity of silicon.

In the case of positive charge carriers, trivalent impurities (i.e. Group III elements such as boron and aluminum) are used, and we have in this case a lack of electrons (excess of holes). Such defects are called "acceptors". Similarly, they introduce new energy levels close to the maxima of the valence band, as displayed in figure 1.6(b), easing the creation of holes in the valence band by exciting electrons out of the filled valence band into the new acceptor level.

**Luminescent defects**

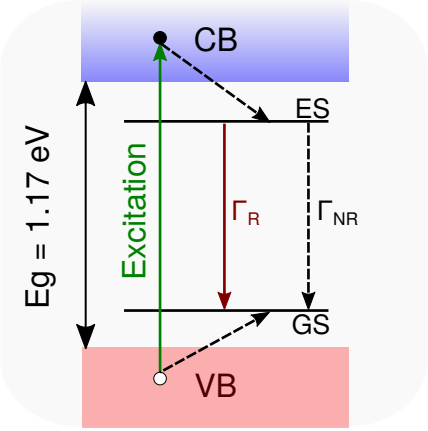


**Figure 1.7:** Energy level structure of a fluorescent defect in silicon. CB: Conduction band. VB: Valence band. GS: Ground state. ES: Excited state. $\Gamma_R$: Radiative transition rate. $\Gamma_{NR}$: Non-radiative transition rate. Dashed arrows represent non-radiative transitions.

A fluorescent point defect has the ability to emit light upon excitation by an optical transition between localized electronic states whose energy levels lie predominantly inside the bandgap of the semiconductor. In a simplified picture, the energy level structure of the defect can be represented by an electronic ground state (GS) and an excited state (ES) inside the bandgap of the semiconductor, as displayed in figure 1.7. Two excitation schemes can be distinguished. (i) An above bandgap excitation consists of a laser delivering photons with energies greater than the bandgap energy, resulting in a photo-excited electron in the conduction band and a vacant state in the valence band, that then relax non-radiatively into the defect, as indicated in figure

1.7. (ii) Resonant excitation directly excites the optical transition of the defect by matching the laser energy to the one of the optical transition. In this manuscript, defects are excited above bandgap by a 532 nm green laser. Once excited, the defect can relax to its stable ground state by emitting a photon of energy close to the energy difference between the two states. The radiative transition without emission of phonon is called the zero phonon line (ZPL), and is accompanied by phonon-assisted emission, called the phonon sideband (PSB). A non-radiative transition can also occur between the two isolated levels as indicated by the dashed arrow in figure 1.7.

### 1.1.3 Silicon industrial grade nanofabrication technologies

In the semiconductor industry, the complementary metal-oxide-semiconductor (CMOS) integrated circuit (IC) manufacturing process is the foundation of modern microprocessors. This manufacturing process was enabled by the ability to create ultra pure mono-crystalline silicon wafers with purity reaching 99.9999 %, and by controlled doping allowing a fine control of the electronic properties to produce semiconductor devices. This doping consists in the intentional introduction of impurities or defects into the semiconductor.

As the silicon wafers used in this manuscript are CMOS compatible, it is relevant to examine the defect engineering carried out in the semiconductor industry, looking first at the ultrapure silicon wafers that are produced and then the doping process. Finally, we present silicon integrated photonics, which exploits the optical properties of silicon in the near infrared, using nanostructuring techniques to design integrated photonic devices operating at the optical telecommunication wavelength compatible with optical fibre communications.

#### Defect engineering

Ultra pure mono-crystalline silicon wafer:



**Figure 1.8:** Silicon ingots and wafers, grown in a cylindrical shape (called boule) then sliced to form standard wafers.

Before the 1950s, measurements of electrical conductivity or optical absorption on natural semiconductor minerals gave non-reproducible results. The cause of this effect was the fluctuation in the composition and purity of these minerals. The presence of defects and impurities

break the periodicity of the crystal lattice and drastically change the properties of the semiconductors (in particular conductivity, free carrier mobility and carrier lifetime), even at the parts per million or billion level [30]. In 1947, the discovery of the transistor motivated novel preparation methods of crystals, with the aim of obtaining pure and structurally perfect crystals to ensure the reproducibility of the intrinsic properties of semiconductors. Efficient and cheap methods of purification and crystallization have been implemented, such as the Czochralski and Float-zone methods. Additionally, methods such as the "Dash" process (or "necking") ensure the growth of dislocation-free crystals. These techniques now enable the production of 300 mm diameter wafers made of 99.99999999 % pure single crystal silicon, corresponding to residual impurities concentration typically inferior to $10^{10}$ cm$^{-3}$ [22].

Impurity doping:

Intrinsic silicon has a low electronic conductivity, as any pure semiconductor. For the purpose of semiconductor device operation, impurities are incorporated in the crystal lattice (post-growth doping), in order to control and enhance the electronic conductivity. The most popular method is the implantation of ions into the Si crystal to incorporate the defects into the lattice (which will also be used in this manuscript). Such semiconductors are called extrinsic semiconductors. Semiconductors with electrons as the dominant carriers are called n-type semiconductors. Semiconductors with conduction through holes are called p-type semiconductors.

Typical doping levels for silicon devices range from $10^{13}$ to about $10^{18}$ dopant atoms per cubic centimeter [22], or approximately one impurity atom per $10^{10}$ to about $10^{5}$ host atoms. The efficiency of this doping positions the silicon platform as an attractive material for electronic defect engineering applications.

### Silicon integrated photonics

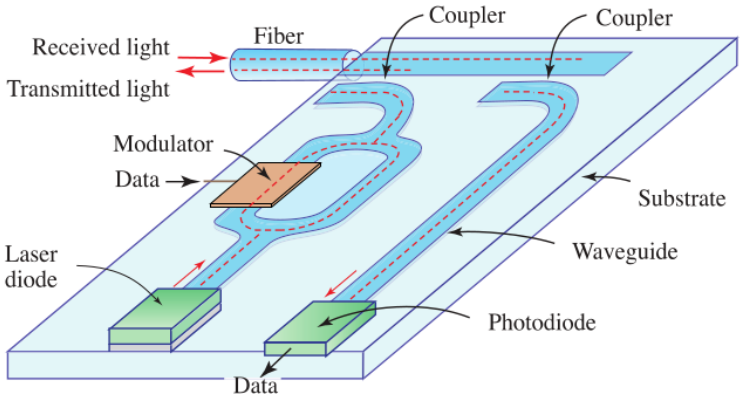


**Figure 1.9:** Schematic of a silicon photonic integrated circuit (PIC). Light enters through a waveguide and is routed to a photodiode where it is detected. A laser diode produces light that is guided, modulated and coupled into an optical fibre for transmission, from [31].

Silicon integrated photonics consist of photon generation, detection, and manipulation using silicon as an optical medium. It has the benefit of lifting some of the limitations of microelectronics, such as heat generation by the Joule effect. Photon generation is usually performed by an external laser injected in the photonic circuit via optical components such as waveguides and couplers or by a range of nonlinear optical phenomena, which produce probabilistic photons. The optical properties of this material in the near infrared make it appropriate for integrated photonic devices at the optical telecommunications wavelength. Silicon is optically transparent above wavelengths $\approx 1.15$ $\mu$m due to the bandgap value $E_g \approx 1.1$ eV, allowing operation at wavelengths commonly used for optical telecommunications ($\approx 1.55$ $\mu$m). Silicon also has a high refractive index of n $\approx 3.5$, well above the one of $SiO_2$ (n $\approx 1.5$).

Photonic circuits consist of silicon-on-insulator (SOI) wafers, with optical components (such as waveguides, lasers, polarizers, and phase shifters) integrated on the top silicon layer by nanostructuring (see figure 1.9). Typically, a 220 nm top layer of Si in SOI is used in Si photonics. Such multilayer allows monomode efficient confinement of light in the planar top silicon layer, due to the high vertical index contrast. Industrial grade nanofabrication facilities routinely provide high quality optical waveguides and cavities operating at telecom wavelength, that can be integrated with superconducting nanowire single photon detectors [32].

Silicon is a monoatomic semiconductor and the maturity of its industry allows the production of crystals of high purity. Moreover, doping and nanofabrication techniques are very efficient on this indirect gap material. All these points are attractive for applications in quantum technologies.

## 1.2 The Silicon platform for quantum applications

Over the past 30 years, interest in quantum technologies has been growing. The building block of quantum technologies is a qubit, a two-level quantum system that can be initialized, coherently manipulated and measured with high fidelity. Four fields of activity are commonly distinguished in quantum technologies, namely sensing, simulation, computation and communication. (i) Quantum communications such as quantum key distribution aim at exchanging information over large distances in a totally secure way thanks to the laws of quantum mechanics and especially the non-cloning theorem. (ii) Quantum computing relies on a succession of quantum logic gates that implement a quantum algorithm to solve problems untrackable on classical computers. (iii) Quantum simulation investigates the evolution of a quantum system that mimics a complex problem to be solved. (iv) Quantum sensing aims to develop novel sensors to measure physical quantities with unprecedented sensitivity and/or with spatial resolution down to the nanometer-scale. Each of these four fields have different desired features.

Many directions have been chosen for the physical implementation of qubits, such as superconducting quantum circuit or trapped ion systems, but our focus here will be solely on silicon-based systems. Indeed, silicon is an attractive material for large-scale integration and for access to isotopically enriched $^{28}$Si offering a low magnetic noise environment that has enabled

very long spin coherence times for nuclear and electron spins [9, 33]. The aim is not to be exhaustive, but to present here the most advanced quantum systems currently available for the development of silicon-based quantum technologies: electrical and photonic qubits.

### 1.2.1 Electrical qubits

Electrical qubits are qubits controlled by electrical means only. Realizations of such qubits rely on the control of the charge or the spin of electrons or holes, to get the two quantum levels needed to encode information. In silicon, there are two main realizations of electrical qubits, in the form of individual shallow dopants and gate-patterned quantum dots (QD), that we will now present.

Gate-defined quantum dots:

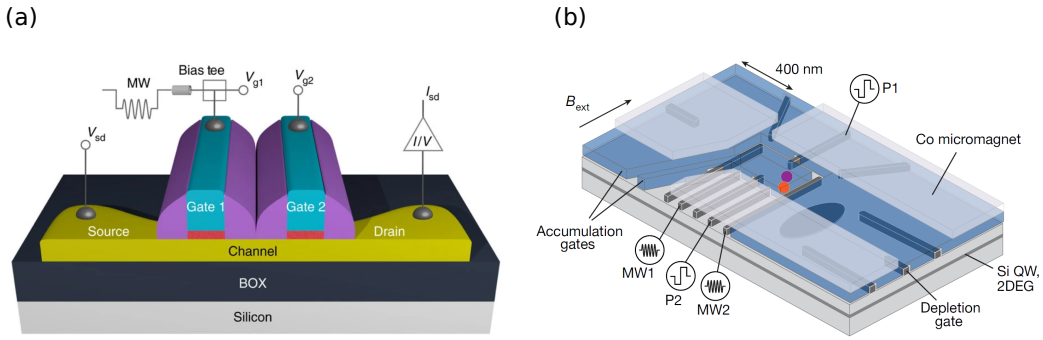


**Figure 1.10:** (a) Simplified three-dimensional schematic of a silicon-on-insulator nanowire field-effect transistor with two gates from [34]. (b) Schematic of a Si/SiGe double-quantum-dot device, from [35].

Through electrostatic gating and confinement, it is possible to control the location of an individual electron or hole in a quantum dot (QD). These semiconductor-based QDs can be measured and used to encode a qubit (by either the charge or the spin degree of freedom) and the initialization, manipulation and measurement are done by electrical means only. Many architectures exist in metal–oxide–semiconductor (MOS) devices with either planar [9] or nanowire [8, 34] structures ensuring the confinement of electrons (or holes).

A gate-addressable spin qubit QD with isotopically purified $^{28}$Si reducing greatly magnetic noise is a promising scalable system. This single electron spin confined in a QD displays a free-induction coherence time of $T_2^* = 120$ $\mu$s, that can be extended to $T_2 = 28$ ms using dynamical decoupling sequences to eliminate the dephasing from the environment [9]. These values are much longer than the manipulation time (typically $\approx 10$ ns).

Entanglement was demonstrated between two spin QD qubits using gate-controlled Si/SiGe double-quantum-dot devices with reliable two-qubit gates with fidelity around 80 % [35] (see figure 1.10 (b)). This system was recently extended to six qubits with coherence times between

3 to 6 $\mu$s for the six qubits, achieving universal operation, state preparation and measurement with state fidelity ranging from 88% to 96% [36]. Also reported recently was the first electronic quantum chip to emerge from an industrial manufacturing line with quantum dots hosted at a $^{28}Si/^{28}SiO_2$ interface [37].

Another promising system consists of a spin qubit in a SOI nanowire field-effect transistor (CMOS nanotransistor) [34]. The nanowire provides the 2D confinement while gates patterned on top of the structure imposes bounds along the nanowire, creating the QD (see figure 1.10 (a)). A relaxation time $T_1$ was reported at around 2.7 $\mu$s [38]. The approach for this particular device was to take existing microelectronics device and try to adapt it for quantum technologies. In this sense, the prospect of scalability is very good, as the fabrication uses foundry-fabricated SOI transistor technology. The performances of these devices make them more appropriate systems for applications in quantum computing.

Individual dopants:

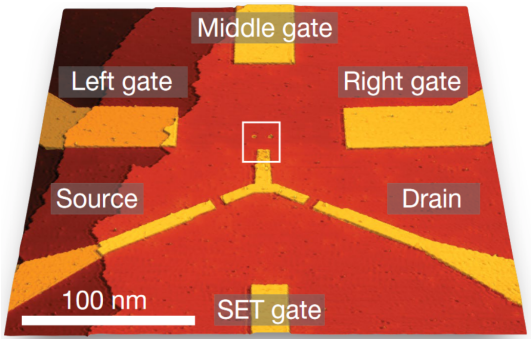


**Figure 1.11:** STM micrograph of the two-qubit phosphorus donor device, from [39].

Some impurities used for doping are also used for quantum technologies. The $^{31}P$ donor atom in silicon is used as a spin qubit and is by far the most studied dopant for quantum applications. Coherent control of both the electron and nuclear spins can be achieved by positioning a single $^{31}P$ atom at the center of an on-chip readout circuitry and a microwave antenna, as displayed in figure 1.11. On isotopically enriched $^{28}Si$ substrates, single-donor qubits coherence time $T_2$ were measured, and in the ionized case ($^{31}P^+$), it gives a $T_2 = 0.56$ s for the electron and a $T_2 = 35.6$ s for the nucleus using dynamical decoupling [40]. Moreover, with the engineering of the qubit position on the atomic scale, a two-qubit gate using phosphorus donor electrons was demonstrated with high fidelity near 94% [39], demonstrating universal control (see figure 1.11).

Despite the predominance of $^{31}P$ dopant in the research on shallow donors, alternative dopants are investigated [41]. Coherent electrical control of a single $^{123}Sb$ nuclear spin (implanted in a MOS nanostructure fabricated on isotopically enriched $^{28}Si$) was reported with a coherent time $T_2^*$ close to 0.1 s [42]. Other defects have been investigated but on ensembles, such as $^{209}Bi$ (Bismuth) [43] and acceptor boron atoms [44], but the longest coherence time is still the one obtained on the $^{31}P$ donor.

All these results show that electrical qubits in silicon, from their coherence properties, scalability and ability to make small-scale quantum processors, are moving towards quantum computing as their main longterm applications. In quantum sensing, magnetic sensing or strain sensing using single donors can be found [41]. Although electron spin qubits benefit from long coherence time and universal control, they cannot be used for quantum communications due to the lack of optical interface [13].

### 1.2.2 Photonic qubits

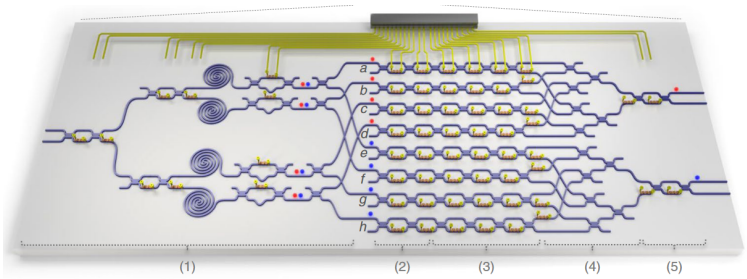


**Figure 1.12:** Schematic of a silicon quantum photonic chip, from [45]. Such quantum information processing circuits is here divided into five parts. The part (1) generates entanglement while the part (2) is preparing initial single-qubit states. The part (3) implements single-qubit operations with the part (4) realizing linear combination, then the part (5) changes the measurement basis. On this chip, photons generation is ensured by an external tunable continuous-wave laser and photons are detected by two fibre-coupled superconducting nanowire single-photon detectors (SNSPDs).

Photonic qubits use the photon as a physical medium, and the encoding of the information can be done by different means, such as the polarization, frequency or in time-bin. To accommodate these qubits, silicon, owing to its well-established and developed integrated photonics, is a promising candidate.

In silicon, light generation is obtained by using third-order ($\chi^{(3)}$) non linear optical processes, enabling efficient photon generation at relatively low power inside SOI waveguide (efficiency of about 0.1% in n-type silicon [46]). However, these methods generate single photons probabilistically. For the realization of quantum networks, quantum interference between independent photons is envisioned to achieve teleportation and entanglement exchange for long-distance quantum communications [47]. On this matter, the probabilistic nature of photon emission using non linear optical processes is an issue if one wants the success rate of multi-photon interference to scale down exponentially with the number of photons involved. This problem could be solved by either a 'source multiplexing' configuration [48] or by using single emitters as integrated single photon sources with deterministic and indistinguishable photons.

Envisioned silicon quantum photonic chips consist of an assembly of optical components (see figure 1.12), each having a different function [49]. On this example, an external tunable laser acts as a pump source to generate entangled photons pairs. Photons are then guided and

manipulated by passive and active optics, and measured efficiently by single photons detectors working at cryogenic temperatures. Universal control has been demonstrated with a two-qubit programmable quantum processor fabricated with standard CMOS-based silicon photonics, built on a single silicon photonics chip and operating at the telecommunications wavelength [45] (see figure 1.12). In silicon photonic quantum chips, storing the quantum states is difficult without quantum memory coupling the photon state to a stationary qubit, such as a nuclear spin.

In conclusion, qubits are very advanced in silicon. However, electrical qubits do not possess optical interfaces, while photonic qubits are unable to be stored without an additional memory. Ideally, one would like to have a (stationary) memory qubit on which to process quantum information locally, as well as a coupling to light to propagate the information over long distances. For this purpose, fluorescent defects could be useful as they can emit single photons and sometimes have spin states that can be used as memory qubits. In the following section, we will explore the fluorescent defects that are promising for quantum applications.

## 1.3 Electron qubits with photonic interfaces

Optically active defects are artificial atoms with radiative transitions. The defect spin degrees of freedom can in some cases be used to encode and process information locally, while the transfer between the different nodes of a quantum network is ensured via an efficient spin-photon interface. Despite their solid-state nature, the spin and electronic states of a defect can be well isolated from environmental fluctuations, leading to record coherence times for solid-state qubits (typically 1 $\mu$s [50]). Moreover, complex and scalable on-chip architectures can be explored by direct nanoprocessing of the host material [51, 52].

The exploration of fluorescent defects to develop quantum technologies has so far focused mainly on wide bandgap semiconductors, such as ZnO, hBN, SiC or diamond. The nitrogen-vacancy (NV) defect in diamond has become a highly mature system, which has been used for a large range of applications, including the first generation of kilometre scale entanglement between solid state spin qubits [14], the realization of quantum errors correction protocols [9] and the development of highly sensitive magnetic field sensors [53]. These results have motivated the search for other defects in materials that are compatible with major industries. Along this line, silicon carbide (SiC) has been envisioned as a possible material because it benefits from mature nano-fabrication techniques compatible with industrial standards [54]. Vacancy-related defects in SiC have shown very promising properties, among which near infrared optically detected magnetic resonance (ODMR) of spin ground state and long coherence time [10]. However, although nanofabrication techniques are more developed in SiC than in diamond, they are still not as refined as those used for the main material of modern microelectronics, silicon.

The use of fluorescent spin defects in silicon for quantum applications is quite recent. However, fluorescent defects in silicon have been extensively studied in the last 50 years. Showcasing this effort is the list of more than 150 fluorescent defects in silicon by G. Davies in his review [17], studied only on ensembles and with a majority of them being carbon or oxygen-related defects.

Few color centers in silicon have been investigated for quantum applications, and we will now look at the most studied and relevant ones.

**Fluorescent defects in silicon**

We will first look at the "heavy element defects" made of atoms heavier than silicon. Then, we will focus on carbon-related defects as well as intrinsic defects in silicon with potential for quantum applications.

Heavy elements defects:

Rare-earth erbium ions Er(3+) in silicon display PL with a very sharp ZPL at 1538 nm. This wavelength lies in the telecom C-band, which is a definite asset for quantum communication. However, the excited state lifetime is around 1 ms, resulting in a low emission rate [55]. Its telecom emission wavelength with the prospect of long coherence time on the spin state (in $Y_2SiO_5$) [56] has driven the incorporation of these defects into silicon nanostructures such as resonators [57] or waveguides [58]. The ultra-narrow ZPL combined with the presence of a spin state and the potential for integration on silicon-based chips imply that this defect is a very good candidate for quantum applications.

Another dopant in Si is copper (Cu), forming an isoelectronic center (Cu-IEC) associated to a ZPL emission at 1228 nm and an ES lifetime of 32 ns [59]. Purcell effect was demonstrated in a SOI photonic nanocavity, decreasing the excited state lifetime down to 1 ns with a quality factor (Q) of around 16,000 [59], thereby demonstrating the first cavity-enhanced ultrafast spontaneous emission from dopants in Si. Although the emission of this defect is in the near infrared, no spin state has yet been identified.

Selenium (Se) is a chalcogen and a substitutional donor in silicon. Singly-ionized selenium donors ($^{77}Se^+$) in isotopically purified $^{28}Si$ display a ZPL wavelength at 2904 nm with an excited radiative lifetime of 8 ns [60]. Moreover, this defect possesses a non-zero spin ground state, with Hahn-echo coherence time measurements displaying a $T_2$ of 2 s at T = 1.2 K [61]. The short radiative lifetime (provided that the quantum efficiency is high) together with a long coherence time in silicon are appealing for quantum applications, but the ZPL wavelength in the mid infrared is not adequate for propagation inside optical fibres.

Intrinsic defects:

The W centre is a complex made of three interstitials Si atoms [62]. It is rather well studied due to its detrimental presence in a lot of Si-based structures [63, 64] and can be created by silicon implantation followed by annealing in standard SOI substrates [65]. It is characterized by a bright ZPL emission at 1218 nm (1.018 eV), stemming from a spin-zero to spin-zero transition with a short lifetime of 34.5 ns [65].

We can mention another self-interstitial defect, the X centre which is a tetragonal cluster of

four self-interstitials associated with a ZPL at 1190 nm (1.041 eV) [66,67] which requires further studies to unravel its intrinsic properties and to estimate its possible quantum applications.

Carbon-complex defects:

One of the most common fluorescent defect in manufactured silicon is the G centre. It is composed of two substitutional carbon atoms ($C_s$-$C_s$) interacting with an interstitial silicon ($Si_i$). By combining different experimental techniques, this complex has been demonstrated to be bi-stable, with a A-form converting into a B-form under photoinjection with the B-form being responsible for the ZPL luminescence of the defect [68]. This defect exhibits a ZPL emission at 1279 nm (969 meV) in the telecom O-band, a high temperature emission above liquid nitrogen [69], detection of an ODMR on ensembles [19] indicating the presence of a triplet spin metastable state that could be use for spin manipulation. It has a short excited state lifetime of 6 ns [18].

A defect (attributed to the G centre from the similarity of their ZPL emission) was for the first time isolated in silicon [21]. This bright defect presents a ZPL centered around 1270 nm and an excited lifetime of 32 ns.

The C centre complex, composed of an interstitial carbon and oxygen pair, gives rise to a ZPL emission at 1571 nm (790 meV) originating from a singlet to singlet transition with a ES lifetime of 2.3 $\mu$s at T = 8 K [70,71]. A triplet excited state is also optically active at 1575 nm (787 meV) in the C-band but with an intensity of 0.0079 relative to the normalized ZPL [70]. This intensity ratio suggests that optical spin manipulation will prove to be very challenging.

The T centre is a complex supposed to be made of at least one hydrogen atom and two bonded carbon atoms [72] and it is one of the few damage centers to possess a native electron spin in the ground state. It has a ZPL emission at 1326 nm, in the telecom O-band, with an excited state lifetime of 0.94 $\mu$s [73]. Electron spin coherent control with Hahn echo coherence times $T_2$ of 2 ms was reported in $^{28}$Si SOI, with nuclear spins $T_2$ exceeding the second [73]. In addition, single T centres were recently optically detected and the optical initialization of their electronic spin was demonstrated [16]. These results are promising for the construction of an all-silicon spin-photon interface for distributed quantum computing and global quantum network.

As stated in the introduction, in this thesis, we have initially chosen to focus our study on the G centre (see chapter 3) as it is a promising candidate for quantum applications, mainly due to its emission in the O-band, a fast radiative recombination time (appealing for efficient light emission) and the presence of an electronic spin triplet (S=1) (that could allow optical spin control). This led us to investigate carbon-implanted samples and a silicon-implanted sample, enabling the investigation of multiple carbon-related defects (see chapter 2), as well as an intrinsic defect, the W centre (see chapter 4).

## Conclusion

Silicon is the basis of today's microelectronics and it can also be used for quantum applications. In this chapter, it has been shown that quantum light sources can be obtained in silicon by means of optically active centres embedded in the silicon matrix. Moreover, among the defects studied for quantum applications, an isovalent carbon-related impurity, the G centre, is expected to be a promising candidate for single photon emission and spin qubit. In the next chapter, carbon implanted silicon, initially investigated to study the G centre, has led to the discovery of seven unidentified single defects in silicon, demonstrating that silicon can host multiple optically active defects emitting in the near infrared. These single defects will be investigated using spectroscopic and intensity-correlation measurements.

Chapter 2

# Single near-infrared emitters in carbon-implanted silicon

## Contents


**2.1 Experimental set-up . . . . . 24**
2.1.1 Low temperature confocal microscope . . . . . 24
2.1.2 Hanbury Brown and Twiss set-up and autocorrelation function $g^{(2)}(\tau)$ . 28
**2.2 Isolation of single photon emitters . . . . . 30**
2.2.1 Spectral identification of seven families of defects . . . . . 30
2.2.2 Demonstration of single photon emission . . . . . 35
**2.3 Emission properties of single defects . . . . . 38**
2.3.1 Zero-phonon line dispersion between defects . . . . . 39
2.3.2 Photostability and saturation curves . . . . . 40
2.3.3 Polarization of the single photons . . . . . 44
2.3.4 Excited-level lifetimes . . . . . 46


Colour centres in silicon have been little studied in the context of quantum applications. Recent renewed interest in fluorescent defects, due to advances in single-defect microspectroscopy techniques allowing the study of individual defects, initiated the consideration of using these coloured centres as qubits. This led to a novel approach in their investigation [21]. The properties of colour centres are investigated at the individual scale by means of confocal microscopy, allowing the identification of possible interesting features, such as a deterministic, efficient and indistinguishable photon emission and the presence of spin states, to be later exploited for quantum applications. In addition, this approach of studying isolated point defects makes it possible to suppress averaging effects on ensemble measurements, and allows the observation of different atomic orientations or the influence of the local environment on the properties of the defects.

This novel method led to the first optical detection of single optically active defects in carbon-implanted silicon [21] followed by reproducible results obtained by another team [74]. These results demonstrated the presence of photo-stable and bright single emitters in carbon-implanted silicon. In the continuation of the previous mentioned works, we present in this chapter the discovery of six new families of individual fluorescent defects in carbon-implanted silicon. Additional insights on the defect reported in [21] will also be given.

In the first section, the home-made confocal microscope used during my PhD thesis as well as the experimental techniques allowing the identification of single emitters will be described. In the second section, the isolation of six new single defects in silicon will be demonstrated by spectroscopic studies and intensity-correlation measurements. In the last section, in order to

investigate their properties and potential for quantum applications, the study of the PL spectra, the polarization of the emitted photons, and the radiative recombination dynamics through lifetime measurements will be detailed.

## 2.1 Experimental set-up

The ability to resolve individual fluorescent defects in silicon requires an experimental set-up that must fulfill several criteria. To be able to detect individual centres, (i) the sample volume probed by the confocal microscope must be small enough to have less than one emitter on average, and (ii) the detection system must be adapted to the low photon flux emitted by a single defect. Then for studies in silicon, (i) the confocal microscope have to be optimized for the infrared as we aim for telecom emitters, and (ii) low temperature operation is required as non-radiative channels appear with increasing temperature, which leds to vanishing PL intensity. Our low temperature infrared-optimized confocal microscope will be detailed in the first part of this section. Then, to identify the presence of an individual fluorescent defect, intensity-correlation measurements are performed to assess whether or not the emitter is generating photons one by one. Thus, the techniques used to characterise the presence of a single emitter will be described in the second section.

### 2.1.1 Low temperature confocal microscope

Upon my arrival, the experimental set-up was already built and its first version had already led to a publication demonstrating the first optical detection of individual fluorescent defects in carbon-implanted silicon [21]. However, modifications and new implementations, such as new single-photon detectors to enhance the detection efficiency and thus be able to discern dimmer emitters, were added during my PhD. Therefore, the focus here will be on describing the main ideas behind the design of this experimental set-up, as well as the techniques that will be used for the intensity-correlation measurements presented in this manuscript. The cryostat allowing experiments at low temperature will be presented first, followed by the description of the optical set-up.

#### Cryostat and vacuum chamber interior layout

In a small band gap material such as silicon, working at cryogenic temperature (T<77 K) is a requirement for the study of fluorescent defects. Indeed, the emergence of non-radiative channels when increasing temperature entails a significant decrease in the PL of defects. Therefore, at cryogenic temperature, the PL of point defects is brighter and spectral lines are narrower than at higher temperatures.

*Helium closed-cycle cryostat*:

To maintain the silicon sample at low temperature, we use a helium closed-cycle cryostat (MyCryoFirm Optidry 200). The main unit of the cryostat is placed on the optical table, and

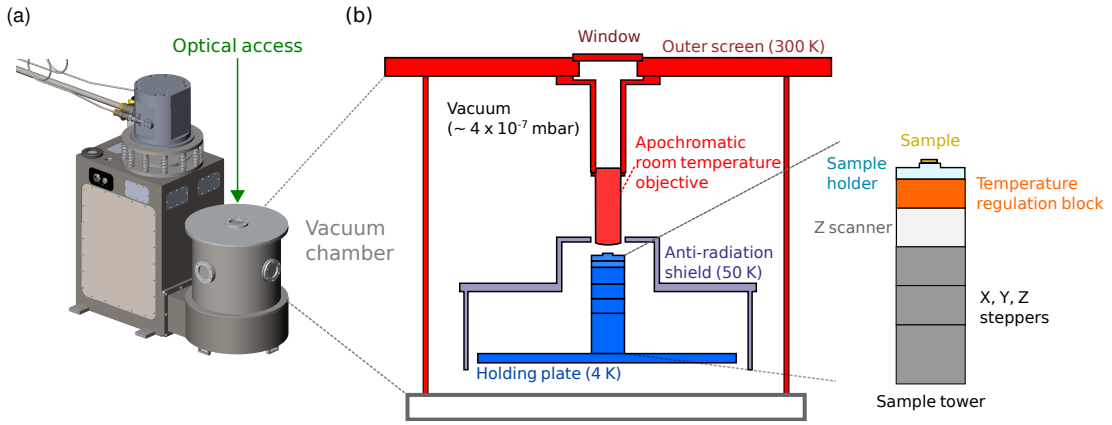


**Figure 2.1:** (a) Optidry 200 cryostat purchased from MyCryoFirm. (b) Schematic of the vacuum chamber. A code color distinguishes the 4 K, 50 K and 300 K elements displayed respectively in blue, purple and red. The sample tower in blue is detailed on the far right. Adapted from [75].

includes the vacuum chamber with a vertical optical access (see figure 2.1(a)). This closed cycle system allows continuous low temperature operation for months. The vacuum chamber reaches a typical vacuum of a few $10^{-7}$ mbar during operation.

*Microscope objective*:

A dry room temperature microscope objective (Olympus LCPLN100XIR) with a high numerical aperture (NA = 0.85) is positioned inside the vacuum chamber, attached at the top of the outer screen as schematized in figure 2.1(b). This plan apochromatic objective ensures an efficient collection in the infrared while allowing a green excitation at 532 nm.

*Sample positioning relative to the objective*:

In the vacuum chamber, the sample is glued with silver paint on a sample holder which is itself mounted on a stack of three linear piezo-stepper nanopositioners (X, Y, Z) (5 mm range each), and a Z piezo-scanner (30 $\mu$m range) for fine-positioning and depth-scan. This stack, labelled as "sample tower", is fixed on the 4 K plate. The sample tower and the 4 K plate are both shielded by an anti-radiation screen cooled down to 50 K and used to protect against heat transfer coming from the outer screen at 300 K. Due to its small working distance ($\approx$ 1.5 mm), the room temperature microscope objective needs to be close to the sample, and therefore has to be inserted inside a hole drilled in the anti-radiation shield (see figure 2.1(b)). This limits the minimum temperature achievable for the sample to about 10 K. The temperature of the cryostat cannot be tuned on demand, so to control the sample temperature, a temperature regulation block (composed of a thermistor and a heating resistance) is inserted in the sample tower below the sample holder (see figure 2.1(b)).

Once the sample is located at the focal plan of the microscope objective inside the cryostat

vaccum chamber, the next step is to optically excite the sample and collect its PL.

### Optical set-up

The optical set-up of a scanning confocal microscope, has here to fulfill three functions. First it must bring the excitation light at 532 nm to the sample. Secondly, the infrared PL emitted by the sample has to be collected efficiently to be able to detect the weak PL signal coming from single photon emitters. Lastly, the optical set-up needs to be as close to achromatic as possible to maximize the overlap between the excitation volume at 532 nm and the collected volume in the near infrared between 1.1 to 1.6 $\mu$m. Both optical paths will be now detailed starting with the excitation path.

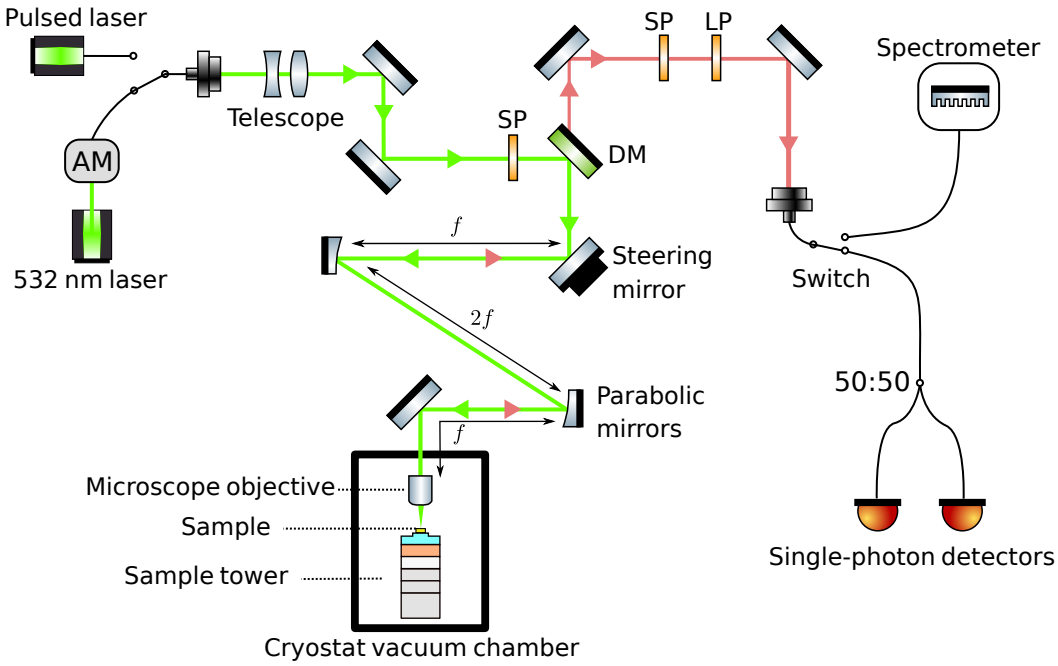


**Figure 2.2:** Schematic of the optical set-up. The optical excitation path is displayed in green, while the optical collection path is displayed in orange. AOM stands for acousto-optic modulator, SP for short pass filter, LP for long pass filter and DM for dichroic mirror. Adapted from [75].

*Excitation lasers*:

A continuous wave (CW) green laser at a wavelength of 532 nm (2.33 eV) is used to pump above bandgap the defects in the silicon sample. A CW green laser was chosen because of a small penetration depth ($\delta_p$) in silicon, close to 1 $\mu$m at 532 nm ($\delta_p = \lambda/4\pi\tilde{n}$ where $\tilde{n}$ is the imaginary part of the refractive index and $\lambda$ is the free space wavelength) [76]. A 976 nm excitation has also been attempted, but the higher penetration length in silicon at this wavelength (close to 100 $\mu$m) was detrimental to the study of single defects due to a poor signal-to-noise ratio, so it was abandoned. The optical power of the excitation path is tuned by controlling the transmission of an acousto-optic modulator (AOM). In addition, a fibered pulsed diode laser at

532 nm with a pulse duration of 150 ps is used to perform excited state lifetime measurements. The excitation laser is coupled into a monomode fiber and sent into the optical excitation path (see figure 2.2), where a fiber collimator convert the laser beam back to free space. The same process is also applied to the fibered pulsed laser.

*Optical excitation path*:

On the optical excitation path, as depicted in figure 2.2, a telescope is inserted to compensate for the residual chromatic aberrations that will be introduced by the microscope objective inside the cryostat. After this telescope, a short-pass filter at 1000 nm was added to eliminate parasitic light produced by Raman scattering in the optical fiber. A dichroic mirror with a cut-on wavelength of 1000 nm was installed to reflect the laser beam in the excitation path into the cryostat, while transmitting the PL in the collection path. The next optic is a steering mirror which ensures the scanning on the sample surface, typically on an area of 120 $\mu$m by 160 $\mu$m. Due to this scanning method, a 4f system with two parabolic mirrors is positioned between the steering mirror and the microscope objective inside the cryostat to ensure that the laser beam is always centered in the objective aperture. We add that the mirrors are parabolic to prevent chromatic aberrations. The laser beam then goes into the cryostat by passing through a fused silica window, to finish into the aforementioned microscope objective where it is focused on the sample.

*Optical collection path*:

The sample PL is collected by the microscope objective and it follows the same path as the excitation up to the dichroic mirror, where the PL is here transmitted (see figure 2.2). A 1050 nm long pass filter is added after the dichroic mirror to filter out any remaining green laser light. Additional long or short pass filters can be added via a filter wheel in the collection path if needed. The PL is then coupled into a single mode optical fiber (with an anti-reflection coating) by a silver reflective collimator preventing again chromatic aberrations. The core of this fiber (d = 8.2 $\mu$m) acts as a confocal pinhole spatially filtering the collected PL. This increases the spatial resolution while also improving the PL contrast.

*Measurement devices*:

The PL signal, via a remote-controlled fibered optical switch, is either conveyed into single-photon detectors or into a spectrometer equipped with a nitrogen-cooled InGaAs camera. Two different single-photon detectors were used during my PhD. The first ones (used in this chapter) are two InGaAs/InP avalanche photodiodes (ID Quantique ID230) working in the single-photon regime, with a quantum efficiency of 10 % at 1.3 $\mu$m. The second ones (used in the next chapter) are two superconducting nanowire single-photon detectors (Single Quantum Eos) with a quantum efficiency up to 80 % at 1.3 $\mu$m.

*Scanning method*:

The scanning method chosen in this experimental set-up is the raster scanning technique.

A steering mirror is used to scan a defined area of the sample pixel by pixel, with the excitation laser spot, while collecting the PL. This allows to reconstruct optical scans (or PL maps), reaching a maximum area of 120 $\mu$m by 160 $\mu$m.

As the optical set-up and imaging technique have been clarified, the optical measurement allowing the identification of a single photon emitter will be discussed in the next section.

### 2.1.2 Hanbury Brown and Twiss set-up and autocorrelation function $g^{(2)}(\tau)$

To determine whether a fluorescent defect is a single emitter or not, we measure if it emits photons one by one or not. This is performed by analyzing the temporal correlations in the fluorescence intensity [77].

*Autocorrelation function* $g^{(2)}(\tau)$:
The second-order correlation function $g^{(2)}(\tau)$, also referred to as the intensity autocorrelation function, quantifies the probability of coincidence between two detection events that take place at times $t$ and $t+\tau$. This function is defined by the equation [78]:

$$g^{(2)}(\tau) = \frac{< I(t)I(t+\tau) >}{< I(t) >^2} \tag{2.1}$$

where I(t) is the luminescence signal at time t, and $< ... >$ is the temporal average over time. The second-order autocorrelation function can also be expressed in terms of probabilities of photon detection [78] as:

$$g^{(2)}(\tau) = \frac{P(t+\tau|t)}{P(t)} \tag{2.2}$$

where $P(t)$ is the probability of detecting a photon at time $t$ and $P(t+\tau|t)$ is the conditional probability of detecting a second photon at time $(t+\tau)$, knowing that a first photon was detected at time t. To better understand how this function will provide the evidence that a defect is single, we consider three possible types of emitters:
(i) First let's consider a coherent source of light, for example the light coming from a laser. The statistical distribution of photons for a coherent source is Poissonian, and there is therefore no correlation between the different photodetections. Thus the two intensities $I(t)$ and $I(t+\tau)$ are uncorrelated, resulting in $g^{(2)}(\tau)$ equal to 1 for any delay time.
(ii) For an individual emitter, photons are emitted one by one, it is therefore not possible to detect two photons at the same time. At zero delay ($\tau = 0$), the probability of having two simultaneous photons is zero ($P(t|t) = 0$), resulting in the autocorrelation function at zero delay being equal to zero: $g^{(2)}(0) = 0$. We add that regardless of the source, at long delay time ($\tau \to \infty$), the events are uncorrelated, thus $P(t+\tau|t) = P(t)$, resulting in $g^{(2)}(\tau) = 1$.
(iii) For N emitters, the value of the autocorrelation function at zero delay is given by 1 - $\frac{1}{N}$ [79]. For N=2 emitters, we obtain $g^{(2)}(\tau = 0) = 0.5$, thus the condition for determining that an emitter is single is $g^{(2)}(0) < 0.5$.

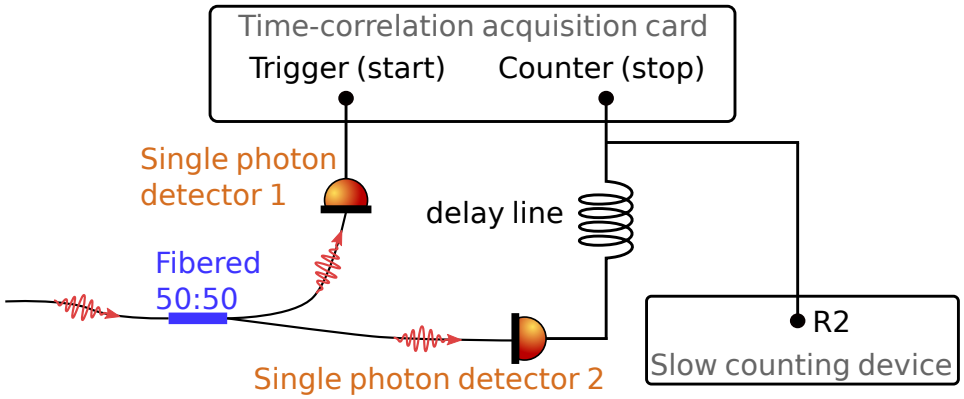


**Figure 2.3:** Schematic of the Hanbury Brown and Twiss on our set-up. Two single photon detectors are positioned after a 50:50 fibered beam splitter. The photon detection events are recorded by the time-correlation acquisition card which constructs the histogram of the time intervals between a start photon detection event and the photon stop events. A delay line was inserted to bypass the deadtime of the fast-counting card. The slow counting module record the photons detected on the single photon detector 2 to enable the normalisation of the histogram.

*Hanbury Brown and Twiss set-up*:

In practice, we measure the second-order correlation function $g^{(2)}(\tau)$ using two detectors mounted in a Hanbury Brown and Twiss (HBT) configuration (see figure 2.3). Two detectors are used to circumvent the detector dead time that would restrict the time intervals we can access to. The photon counting is recorded by a time-correlation acquisition card with a resolution of 100 ps (Fastcomtec 7889). The measurements operate as follows: a photon is detected on detector 1 (referred as the start) triggering the acquisition, then we record all the events associated to a photon detection during a given acquisition window on the second detector 2 (referred as the stop events). The time interval between a start and a stop event is the previously introduced delay $\tau$. By repeating this process, we can construct a histogram of time intervals $\tau$ between two detected photons $J(\tau)$. This histogram $J(\tau)$ needs to be normalized to give the second-order correlation function [80] through:

$$g^{(2)}_{exp.}(\tau) = \frac{J(\tau)}{NwR_2} \tag{2.3}$$

where $N$ is the number of start events, $w$ is the bin time of the histogram and $R_2$ is the photon detection rate on the detector 2. A slow counting module was used to record $R_2$ by duplicating the output pulses of the "stop" detector, while a delay line (50 m of cables) was inserted to add a constant delay of around 300 ns to bypass the deadtime of the fast-counting card (see figure 2.3).

We are now going to use this low temperature confocal microscope and the HBT set-up to investigate single fluorescent defects in silicon.

## 2.2 Isolation of single photon emitters

The study of defects at single scale in silicon allows to probe properties that are inaccessible on ensembles measurements, in the perspective of applications in integrated photonics or quantum applications. It even allows to discover defects that have never been detected before in spectroscopic measurements of defect ensembles [81], as it will be shown in this section. Here we investigate single fluorescent defects created in a carbon-implanted silicon-on-insulator sample. In the first section, after a description of the sample studied in this chapter, a spectral study of its PL emission reveals seven families of defects. Then, in the second section, intensity-correlation measurements are used to demonstrate the isolation of single photon emitters.

### 2.2.1 Spectral identification of seven families of defects

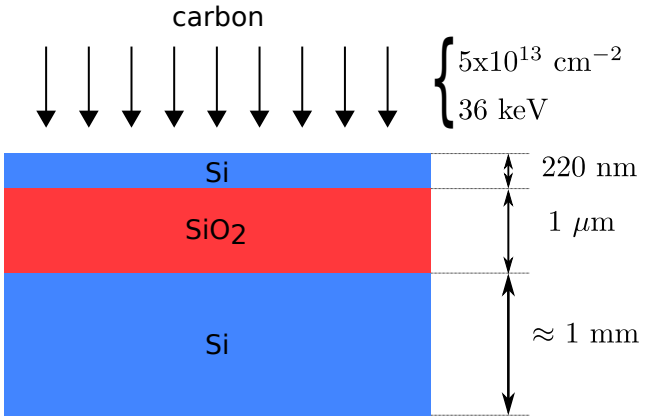


**Figure 2.4:** Sample schematic of a commercial SOI. The arrows represent the implantation ion beam.

#### C-implanted silicon sample

A commercial 220-nm-thick silicon-on-insulator (SOI) wafer with a $SiO_2$ layer of 1 $\mu$m is used in this chapter, as depicted in figure 2.4. Such wafers are commonly used in modern integrated silicon photonics. The initial goal in this sample was to intentionally create a carbon related defect, the G centre (see chapter 1). Thus carbon ions were implanted on the top silicon surface at a fluence of $5 \times 10^{13}$ cm$^{-2}$ with an energy of 36 keV. The energy of the carbon ions was chosen from SRIM (stopping and range of ions in matter software [82]) calculations to ensure that the carbon ions will stop on average 100 nm below the surface, thus assuring that they remain in the top silicon layer. Following this implantation step, annealing was performed at 1000°C for 20 seconds under $N_2$ atmosphere in order to heal the damaged lattice.

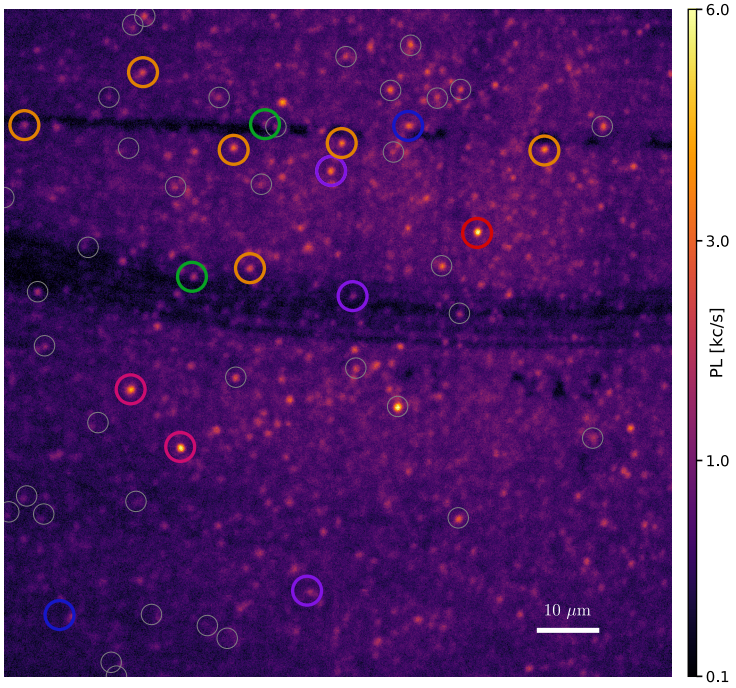


**Figure 2.5:** Typical PL raster scan of the carbon-implanted SOI at T=10 K. The image is 116 $\mu$m by 116 $\mu$m. The point defects investigated are circled. The detailed analysis was performed only on the most common defects with a ZPL or the brightest ones without a ZPL (coloured circles).

### PL map of isolated defects in C-implanted SOI

At a temperature of 10 K and with an above gap excitation at 532 nm, scanning this carbon-implanted silicon sample reveals a multitude of isolated luminescent spots, as illustrated in figure 2.5. In this typical PL scan, we observe a few isolated bright spots (typically above 5 kc/s with detector efficiency at 10 %) and a larger number of dimmer spots (below 2 kc/s) that form a granular background of low intensity. The two horizontal black stripes correspond to scratches in the sample and the circles indicate the isolated spots investigated. In order to study a large number of isolated spots and to increase the statistics of the interesting emitters, similar PL scans were performed at different positions on the sample. On each of these scans, isolated spots were selected and their position recorded so that these could be located again for future studies. This method allowed us to study a total of 633 hotspots in an area of 600 $\mu$m by 600 $\mu$m. In order to identify their nature, PL spectroscopy was performed on these emitters.

### PL spectrum of single hotspots

Among the investigated isolated spots, only those with a zero-phonon line (ZPL) or the brightest emitters without ZPL were further analysed (represented in figure 2.5 by coloured circles), corresponding to 75 hotspots. This post-selection was practical in order to facilitate the

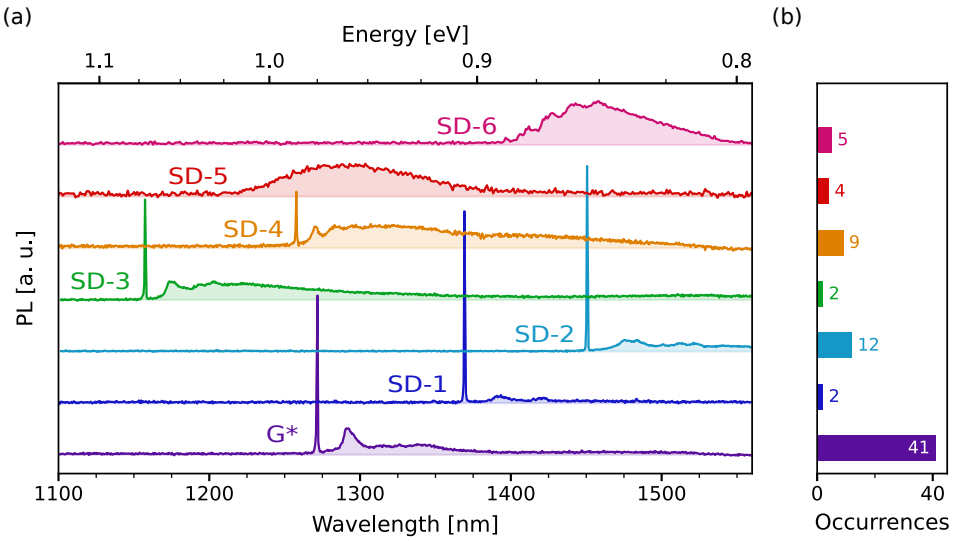


**Figure 2.6:** (a) PL spectra recorded on seven different individual single-photon emitters. The spectra SD-1 to SD-6 correspond to six families of single emitters randomly distributed over the sample. (b) Histogram of the number of defects per family.

study of these defects. Among the post-selected emitters, the seven most frequent PL spectra are plotted in figure 2.6(a). Three types of PL spectrum can be identified in this figure. The bottom three PL spectra labelled G*, SD-1 and SD-2 have a high ZPL relative to the phonon sideband (PSB), centred at 1269, 1369 and 1448 nm, respectively. The G* defects is labelled differently as it was studied at single scale before the start of my thesis in a previous work from my group and collaborators [21]. The two middle PL spectra, labelled SD-3 and SD-4, have a smaller ZPL, centred at 1157 and 1253 nm, respectively. And finally, the top two PL spectra labelled SD-5 and SD-6 have no ZPL with a broadband emission centred at 1300 nm and 1460 nm, respectively.

*Debye-Waller factor*:

For defects with a ZPL, we can provide information on the electron-phonon coupling [83] by examining the ratio of photons emitted in the ZPL to all photons, known as the Debye-Waller (DW) factor. The proportion of ZPL photons reaches values as high as 35% and 25% for the SD-1 and SD-2 defects, respectively, while it is limited to 2-3% for the SD-3 and SD-4 families. The G* centre exhibits a DW of 15 % (for comparison, the NV centre in diamond have a DW of 3 %). A large DW is preferred in the perspective of developing single indistinguishable photon sources since only the photons emitted in the ZPL can be used to produce indistinguishable photons.

*Unidentified isolated defects*:

From these PL spectra, two families (G* and SD-2) might be associated to known defects. (i) G* has a mean ZPL energy that matches the one of ensembles of G centres, which is the reason why it is labelled G* [21, 81]. However, we highlight the absence, in the PL spectrum of

G* defects, of an emission line at 70 meV from the ZPL, which is associated to a local vibration mode specific to the G centre called E-line in the literature [68, 84]. It explains why another labelling is introduced here with the asterisk indicating that it is similar to a G centre, but not strictly the same. Excited state lifetime and photon polarization measurements allow also to differentiate the G* centre from the G centre (see chapter 3).
(ii) The SD-2 defect might be the interstitial carbon defect C(i), which is thought to be a precursor of G centres, and that has an emission line at 856 meV [17, 85]. However photon polarization measurements and a study of the ZPL energy over multiple SD-2 defects will cast doubt on this association (see section 2.3.1).

The other observed defects differ from the ones identified and classified in previous studies performed in ensembles. As such, the PL spectra in figure 2.6 are new among the vast literature of luminescent defects in silicon.

*Defects occurrences*:

The occurrences of these defects are shown in figure 2.6(b). We notice that the occurrences of defects SD-1 to SD-6 are quite low (inferior to 16 %) in comparison to G* ($\approx$ 55 %). This could explain why these defects have not been reported so far, as their low occurrence would make them beyond the detection limit in ensemble measurements [17, 86].

**Seven distinct families**

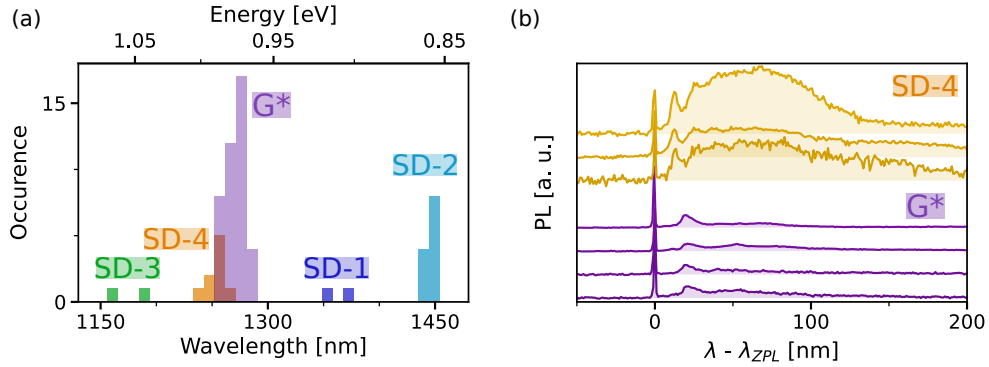


**Figure 2.7:** (a) Histogram of the ZPL wavelength and energy measured on all families featuring a ZPL. (b) PL spectra of 4 different G* defects in purple and 3 different SD-4 defects in orange. PL spectra are shifted to get the ZPL at the origin of the x-axis. They are normalized to the maximum of the ZPL peak.

From their PL spectra, the seven families appear to be distinct from each other as they display spectral characteristics such as Debye-Waller factor and PSB profile that differ from one another. However, one can ask if some defects belong to the same family. For example, defects SD-1 and SD-2 could be of the same family with a large dispersion of the ZPL, caused by local stress or different charge states. To support the relevance of the classification into seven different families of defects, we examine the histogram of the ZPL wavelength for all the defects

that possess a ZPL (SD-1 to SD-4 and G*), presented in figure 2.7(a). In this figure, it can be seen that the histograms do not overlap, except for the SD-4 and G* defects.

PL spectra of SD-4 and G* defects are shown in figure 2.7(b), displaying: (i) that different spectra of the same family are very similar (slightly less so for SD4), and (ii) that their PSB are clearly distinct. SD-4 defects display a bright PSB extending up to around 150 nm relative to the ZPL while G* defects display a weaker PSB extending up to around 100 nm from the ZPL. Thus these seven PL spectra are associated to seven different types of defects. Next, a more detailed analysis of their PSB will be carried out.

### Comparison of the phonon sideband spectra

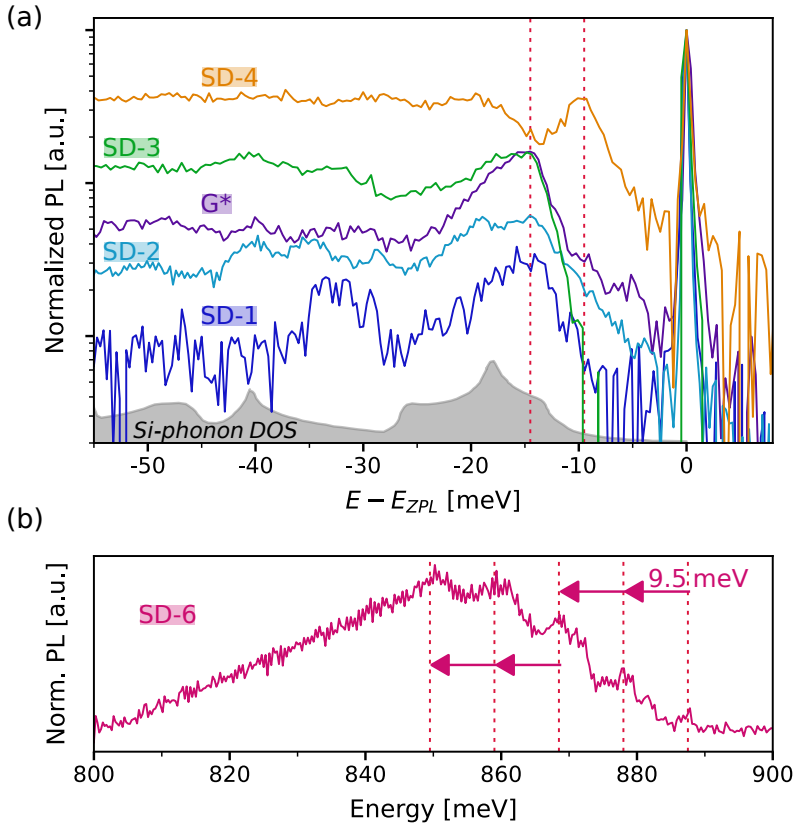


**Figure 2.8:** (a) Comparison of the phonon-sideband for the defects with a ZPL. The spectra are normalized to the ZPL maximum and plotted with respect to their ZPL energy $E_{ZPL}$. The vertical lines show the position of the first phonon replica at 9.5 meV and 14.5 meV. The gray-shaded area indicates the silicon-phonon density of states. (b) PL spectra of the SD-6 defect. The vertical lines display phonon replicas of energies separated by 9.5 meV.

As mentioned previously, the ZPL energy was the first feature in the PL spectrum used to distinguish the different families of defects, and looking at the PSB is another way to differentiate those centers. In figure 2.8(a), the PL spectrum of the five defects with a ZPL are plotted with respect to their ZPL energy to better compare their PSB. By looking at the peaks of the PSB, we observe that the first phonon replica appears at 9.5 meV for SD-4 and at 14.5 meV for G* and

SD-1 to SD-3, as highlighted in figure 2.8(a) by the two dashed vertical lines. The Si-phonon DOS is plotted at the bottom of figure 2.8(a), and it can be seen that the phonon replica at 9.5 meV and 14.5 meV does not correspond to any Si vibration mode. Furthermore, we notice that the overall shape of the Si-phonon DOS does not match the PSB of the defects. In particular, the SD-1 defect shows a PL peak around 32 meV which does not correspond to any peak in the Si-phonon DOS.

In addition, the PSB of the SD-6 defect exhibits a periodicity of 9.5 meV, as depicted in figure 2.8(b). For the PL peaks in the PSB at energies that do not match any of the maxima of the Si-phonon DOS, the vibronic spectrum likely results from phonons combining localized and Bloch vibrational states [87].

We observe hotspots that are spatially well isolated on our scan (i.e. that we can resolve), so one would be tempted to think that they may be associated with individual defects. However, to check this hypothesis, we need to analyse their photon emission statistics and ensure that they emit single photons one by one.

### 2.2.2 Demonstration of single photon emission

With the HBT set-up presented in section 2.1.2, analysis of the correlation between detected photons can indicate whether or not a defect is a single photon emitter.

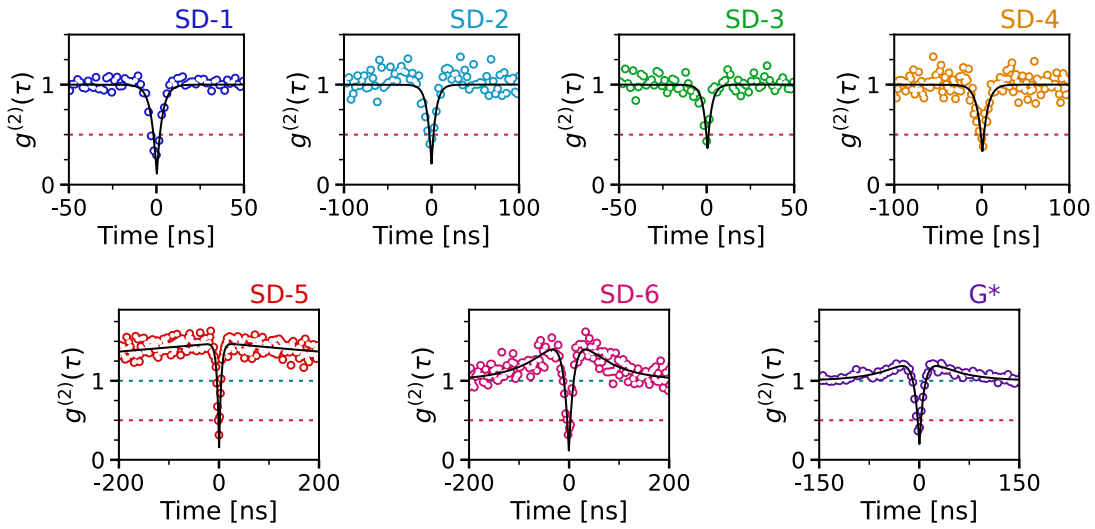


**Figure 2.9:** Second-order autocorrelation function $g^2(\tau)$ for seven defects of different families. The colour code corresponds to the one of figure 2.6. The solid black lines represent data fitting with the equation (2.7) for SD-1 to SD-4 and eq. (2.9) for SD-5, SD-6 and G*, deduced respectively from the modelling of the dynamics of a 2-level and 3-level systems.

*Autocorrelation function $g^{(2)}(\tau)$:*

The autocorrelation function $g^{(2)}(\tau)$ for defects in each of the seven families is plotted in

figure 2.9. A dip at zero delay is observed in each case, corresponding to an antibunching that fulfills the single-emitter condition of $g^{(2)}(\tau) < 0.5$ [88]. However, we can observe for all families that the experimental antibunching at zero delay does not reach 0, as expected for a perfect single photon source. Specifically, the value $g^{(2)}_{exp}(0)$ for the different families is displayed in table 2.1. The deviation of $g^{(2)}_{exp}(0)$ from ideal single-photon emission ($g^{(2)}(0) = 0$) is the result of background photons and detector dark counts, both of which produce uncorrelated detector clicks, increasing the antibunching value at zero delay. Since background photons and detector dark counts are assumed to be uncorrelated with the emission of defects, their contribution can be subtracted in the autocorrelation function $g^{(2)}(\tau)$.

| Family | SD-1 | SD-2 | SD-3 | SD-4 | SD-5 | SD-6 | G* |
|---|---|---|---|---|---|---|---|
| $g^{(2)}_{exp}(0)$ | $\approx 0.21(1)$ | $\approx 0.20(2)$ | $\approx 0.40(2)$ | $\approx 0.30(3)$ | $\approx 0.26(1)$ | $\approx 0.18(4)$ | $\approx 0.27(1)$ |

**Table 2.1:** Values of the antibunching at zero delay $g^{(2)}(0)$ for the different families.

*Background correction*:

With our ID230 detectors, the dark counts are typically 50 counts/s, which is negligible compared to the background photons typically greater than 1 kcount/s at the optical powers used in these measurements. The jitter of our single-photon detectors is typically 150 ps, so its influence is negligible in our measurements, as it is less than the time scale of the data, typically in the nanosecond range. Therefore, only the total noise counts that include both the sample background counts and the detector dark counts will be taken into account. This can be confirmed by removing the contribution of the noise counts in the experimental autocorrelation function $g^{(2)}_{exp}(\tau)$ following the equation [89]:

$$g^{(2)}_{cor}(\tau) = \frac{g^{(2)}_{exp.}(\tau) - (1-\rho^2)}{\rho^2} \tag{2.4}$$

where $\rho$ is related to the signal-to-noise ratio (SNR) by $\rho = 1/(1 + 1/\text{SNR})$. The SNR is obtained by collecting the luminescence signal (including the dark counts) a few micrometres away from the defects under investigation. The recorded SNR are 8(1), 3(1), 3(1), 4(1), 7(1), 5(1) and 5(1) for the SD-1 to SD6 and G* defects, in figure 2.9 respectively. This gives $g^{(2)}_{cor}(0)$ values of 0.1(1), 0.0(1), 0.1(1), 0.2(1), 0.1(1), 0.0(1) and 0.1(1) for the SD-1 to SD6 and G* defects, respectively. Thus, when corrected for PL background noise, the autocorrelation function at zero delay $g^{(2)}_{cor}(0)$ is zero within the error bars. The deviation of $g^{(2)}(0)$ from zero value for the defects is attributed to spatial inhomogeneities of the background counts, which prevent an accurate estimation of the SNR at the exact position of the defects.

*Bunching effect*:

For defects SD-5 and SD-6, as well as G*, we observe $g^{(2)}(\tau)$ values greater than 1 at intermediate delay time. This effect is referred to as bunching. It is well explained by the presence of a non-radiative decay channel through a metastable state (MS) in the electronic level structure,

which traps part of the population during optical cycles [21, 90].

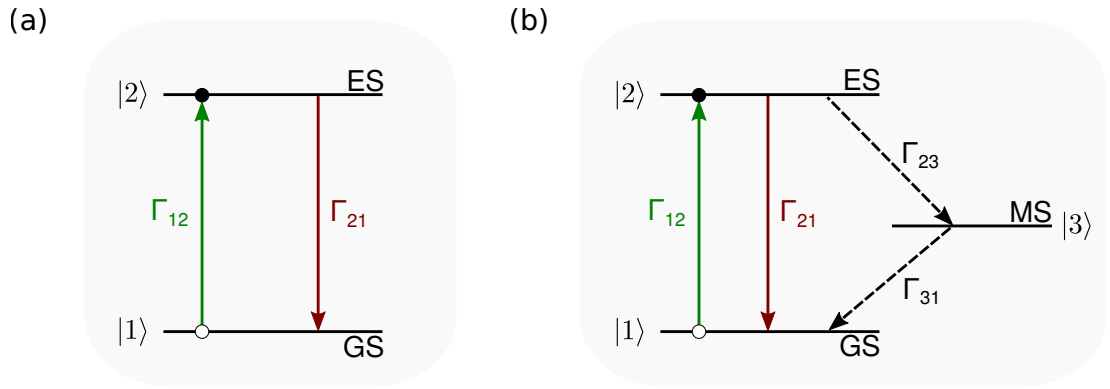


**Figure 2.10:** (a) Two-level model used to describe the dynamics of defects SD-1 to SD-4. (b) Three-level model used to describe the dynamics of defects defects SD-5, SD-6 and G*. GS: Ground state. ES: Excited state. MS: Metastable state.

*Modeling of the $g^{(2)}(\tau)$ function*:

To model the defects SD-1 to SD-4, let us consider a two-level system (represented in figure 2.10(a)), with a ground state $|1\rangle$ having a population $n_1$ and an excited state $|2\rangle$ having a population $n_2$. The transition rates between these two electronic states are $\Gamma_{12}$, the excitation rate from the ground state to the excited state, and $\Gamma_{21}$, the recombination rate from the excited state to the ground state. The evolution of the populations of a two-level system is governed by the following system of differential equations:

$$\begin{cases} \frac{\mathrm{d}}{\mathrm{d}t}\begin{pmatrix} n_1 \\ n_2 \end{pmatrix} = \begin{pmatrix} -\Gamma_{12} & \Gamma_{21} \\ \Gamma_{12} & -\Gamma_{21} \end{pmatrix} \cdot \begin{pmatrix} n_1 \\ n_2 \end{pmatrix} \\ \\ n_1 + n_2 = 1 \end{cases} \tag{2.5}$$

As mentioned in section 2.1.2, the intensity autocorrelation function is the probability of detecting a photon at time $t+\tau$ knowing that a photon was emitted at time $t$. The detection of a photon at time t (t=0), projects the system into the ground state. Thus the probability of detecting a second photon at time $\tau$ is governed by the evolution of the population of the excited state $P(t+\tau|t) = P(\tau|0) = \Gamma_{21} \cdot n_2(\tau)$. The term $P(t)$ corresponds to the probability of detecting a photon at any time. This probability is $P(t) = \Gamma_{21} \cdot n_2(\infty)$, where $n_2(\infty)$ represents the steady-state population of state $|2\rangle$. We thus obtain the following formula for the intensity autocorrelation function [78]:

$$g^{(2)}(\tau) = \frac{n_2(\tau)}{n_2(\infty)} \tag{2.6}$$

Then, with the two boundary conditions $g^{(2)}(0) = 0$ and $g^{(2)}(\infty) = 1$, corresponding to single photon emission and correlations loss at long time, respectively (see section 2.1.2), the autocorrelation function can be written as follows:

$$g^{(2)}_{2LS}(\tau) = 1 + \beta - (1+\beta)e^{-\Lambda_0 \tau} \tag{2.7}$$

with the two parameters $\beta = \frac{\Gamma_{12}}{\Gamma_{21}}$ and $\Lambda_0 = \Gamma_{12} + \Gamma_{21}$ being functions of the rates between the levels [90]. For the defects SD-1 to SD-4, the data were fitted by equation 2.7. This two-level model follows the data nicely (see figure 2.9), so the dynamics of emission of these defects is well explained by a two-level system.

In contrast, to model defects SD-5 and SD-6, as well as G*, we consider a three-level system, as depicted in figure 2.10(b). The evolution of the populations of a three-level system is governed by the system of differential equations:

$$\begin{cases} \frac{\mathrm{d}}{\mathrm{d}t}\begin{pmatrix} n_1 \\ n_2 \\ n_3 \end{pmatrix} = \begin{pmatrix} -\Gamma_{12} & \Gamma_{21} & \Gamma_{31} \\ \Gamma_{12} & -\Gamma_{21} - \Gamma_{23} & 0 \\ 0 & \Gamma_{23} & -\Gamma_{31} \end{pmatrix} \cdot \begin{pmatrix} n_1 \\ n_2 \\ n_3 \end{pmatrix} \\ \\ n_1 + n_2 + n_3 = 1 \end{cases} \tag{2.8}$$

By solving this system of differential equations, the autocorrelation function can be written as follows [90]:

$$g^{(2)}_{3LS}(\tau) = 1 - (1+\beta)e^{-\Lambda_0\tau} + \beta e^{-\Lambda_1\tau} \tag{2.9}$$

The parameter $\beta$ represents the bunching amplitude, while the parameters $\Lambda_0$ and $\Lambda_1$ quantify the slopes of the antibunching and of the bunching respectively. For defects SD-5 and SD-6, as well as G*, the data were fitted with the equation 2.9. The model and data are in good agreement (see figure 2.9), confirming that a three-level system can explain the photodynamics of these defects.

In order to further investigate the photodynamics of these defects, a study of the autocorrelation function as a function of optical power is required [78]. For the G* centre, it has been shown that a photo-induced repumping mechanism transferred the trapped population from the MS to the ES [21]. In this case, the three-level model shown in figure 2.10(b) is not valid anymore to explain the data, as an extra rate $\Gamma_{32}$ connecting the MS to the ES needs to be added. Analyzing the evolution of the $g^{(2)}(\tau)$ function with the laser excitation power has not been performed on the SD-5 and SD-6 defects, however, it was carried out on single W centres presented in chapter 4.

From this spectroscopic study and these intensity-correlation measurements, we have demonstrated that the hotspots sorted in 7 families of defects in section 2.2.1 are single emitters. Next, we will further investigate their properties at the individual defect scale.

## 2.3 Emission properties of single defects

Knowing that the SD-1 to SD6 defects and the G* centre [21] are single emitters, their properties at individual defect scale will now be further investigated. The ZPL dispersion between defects belonging to the same family will be analysed in the first section, for the most represented families: SD-2 and G*. In the next sections, the saturation curves of the SD defects will be investigated, as well as the polarization of their PL, to finish with the determination of the excited state lifetime of the defects belonging to the SD families.

### 2.3.1 Zero-phonon line dispersion between defects

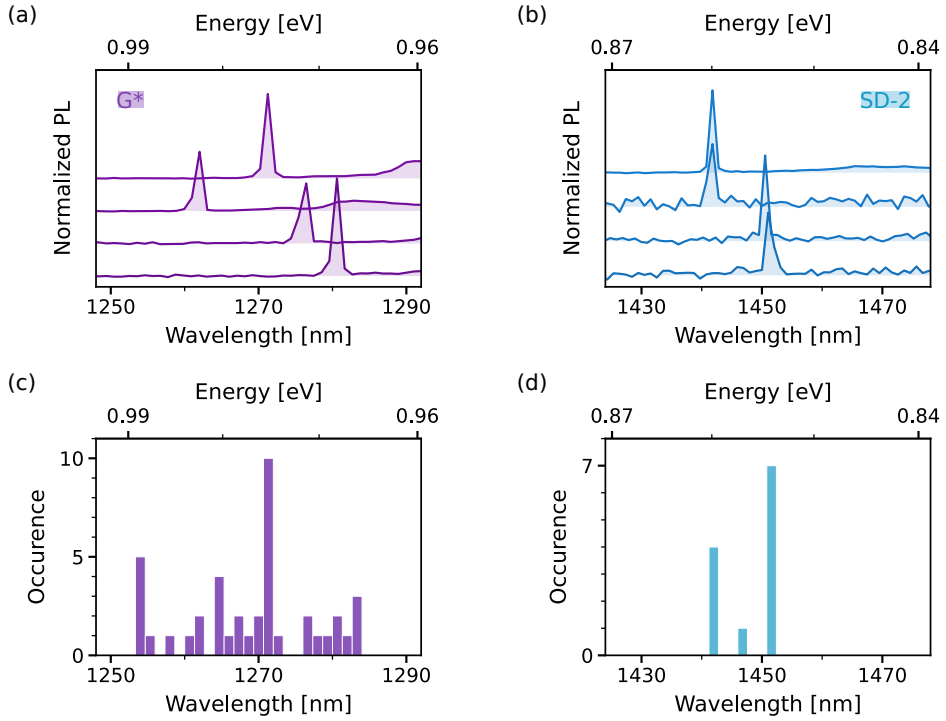


**Figure 2.11:** (a),(b) Typical PL spectra measured on 4 individual defects for families G* and SD-2, respectively. (c),(d) Distribution of the ZPL energy measured for a set of 41 single emitters for G* and a set of 12 single emitters for SD-2.

The variations of the ZPL energy over many defects can give additional insight into the coupling between the defects and its environment. We only study the most common families G* and SD-2 as their number allows a meaningful statistical study. Four PL spectra zoomed on the ZPL for the families G* and SD-2 are plotted in figure 2.11(a) and (b) respectively. Then, via a Lorentzian fit, extracting the ZPL mean energy from the PL spectra of all the emitters of a family allows us to estimate the spread of the ZPL energy for a given family. Figure 2.11(c) and (d) show the histograms of the ZPL energy of 41 G* centres and of 12 SD-2 defects, respectively. We observe two radically different distributions. For G* defects, the ZPL spreads over 20 meV around 977 meV (figures 2.11(a) and 2.11(c)). This large variation of the ZPL energy could be due to local strain and/or different electro-static environment variations [91]. A clear contrast is observed for SD-2 defects, as their ZPL is always found at three different energies equally split by 3 meV around 856 meV (figures 2.11(b) and 2.11(d)). Such behavior suggests the existence of three defect configurations for the SD-2 defects, along with reduced sensitivity to variations of lattice strain or electro-static environments. This potential feature could be an appealing property in the prospect of developing indistinguishable single-photon emissions [92]. Advanced theoretical calculations would nevertheless be required to explain the observed ZPL distribution.

After analysing the PSB shape and ZPL distribution of some of the individual defects, the photostability and saturation curves of the SD defects will be studied in the next section.

### 2.3.2 Photostability and saturation curves

The photostability of the PL emission of the defects will be investigated as well as the evolution of the PL intensity as a function of the optical excitation power for the SD families. Additional insights on the properties of individual G* defects will also be provided with measurements of the evolution of the saturation curves with temperature.

#### Defect photostability

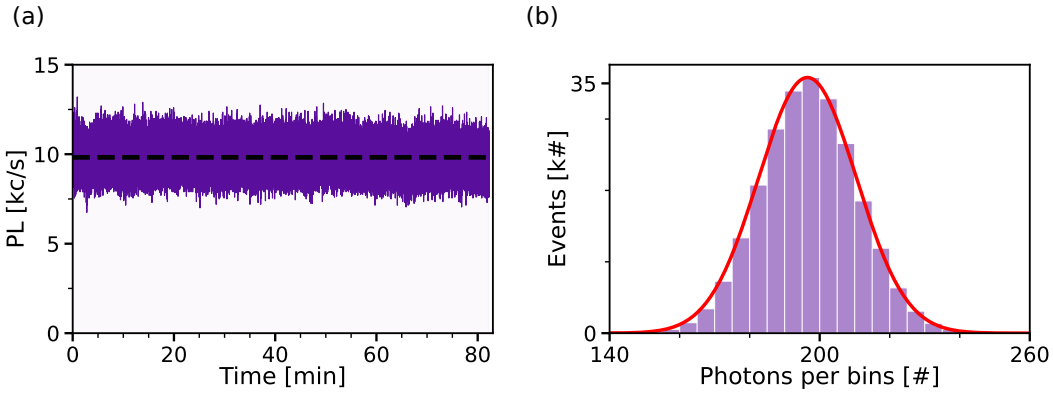


**Figure 2.12:** (a) Typical PL time trace showing a photostable emission beyond one hour, taken on a single G* defect at 11 K and under a 532 nm excitation power of 4 $\mu$W. The dashed line is the PL intensity mean value. Time bin = 20 ms. (b) Histogram of photons per bin of the PL time trace in (a). The red solid line represents a Poissonian distribution with the mean value of the PL time trace in (a).

In order to examine the photostability of the defects, a PL time trace is recorded on a single G* defect, as shown in figure 2.12(a). The individual SD and G* emitters display a perfect photostability over days. Indeed, the mean PL signal (in dashed line in figure 2.12(a)) is constant, with neither blinking, i.e. on-off light emission behaviour, nor bleaching, i.e. extinction of PL usually due to conversion to a non-luminescent form. The intensity variations are investigated by plotting the histogram of the photons per bin for the PL time trace displayed in figure 2.12(b). The histogram follows well a Poissonian distribution, indicating that the intensity variations of the PL time trace are shot noise limited.

Next we investigate the stability of the defects over temperature cycles from 10 K to 300 K back to 10 K. All defects are robust over warming up and cooling down cycles of the cryostat, except defects belonging to family SD-5. Indeed, we notice that the SD-5 defects either disappear or appear in optical scans as shown on figure 2.13. We then focus on the evolution of the SD-2 defect during these temperature cycles, as prolonged annealing at temperature of 300 K has been reported to convert interstitial carbon defects C(i) into G centres [85]. We did not notice any conversion from SD-2 defects into G centres, which raises questions about the

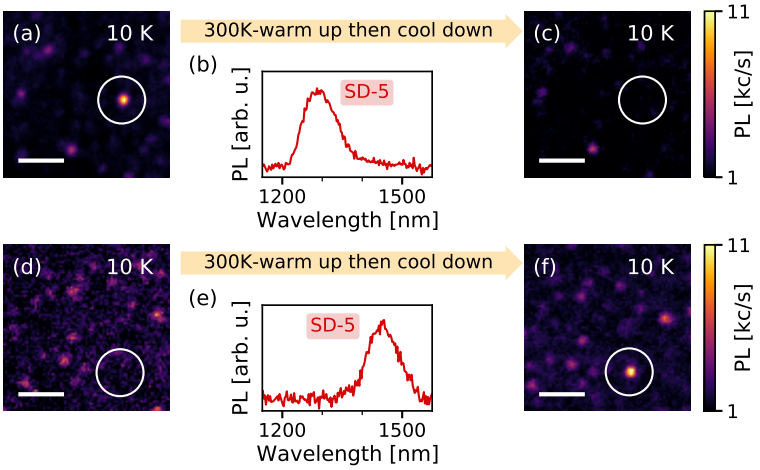


**Figure 2.13:** PL scans acquired at 10K on 2 sample areas before (a,d) and after (c,f) a warming-up of the cryostat to 300K. Horizontal bar corresponds to 5 $\mu$m. (b,e) PL spectra associated with SD-5 family and recorded on the bright spots circled on (a) and (f) respectively.

identification of SD-2 defects to interstitial carbon C(i) defects.

The photostability of the individual defects is here studied at a given optical excitation power. Next we study the PL intensity while varying the optical excitation power.

### Saturation curves

In order to determine the emission intensities at saturation, saturation curves were recorded. A saturation curve corresponds to the PL intensity as a function of the optical power P. The typical saturation curves of SD defects are shown in figure 2.14. In this figure, the raw data are plotted with symbols using the colour code previously introduced in figure 2.6, and the grey symbols correspond to the PL background taken few $\mu$m away from the defect. We observe a similar behaviour for all families when increasing optical power: first a linear increase of the PL intensity with optical power, followed by a transition to a saturation plateau in PL intensity at high power.

To model the saturation curves, we consider the same two-level system as in figure 2.10(a). From the system of differential equations 2.5, we find, in the stationary state, that

$$n_2(\infty) = \frac{1}{1 + \frac{\Gamma_{21}}{\Gamma_{12}}} \tag{2.10}$$

The collected PL intensity $I_{PL}$ is proportional to the intrinsic PL intensity of the defect which is given by the the population in the excited state times the radiative recombination rate:

$$I_{PL} = \eta \cdot I_{intrinsic} \quad \text{with} \quad I_{intrinsic} = \Gamma_R \cdot n_2(\infty) \tag{2.11}$$

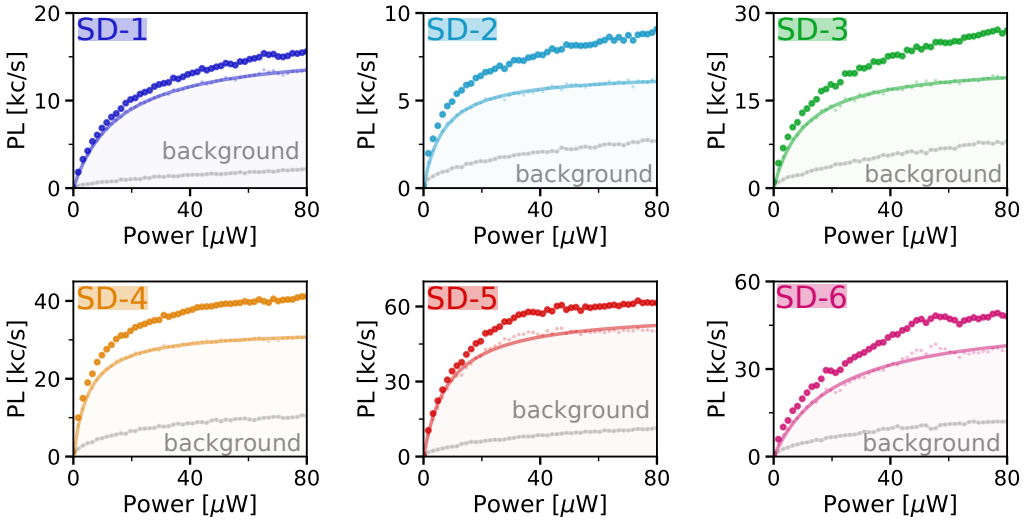


**Figure 2.14:** Typical PL saturation curves for the SD defects taken at 30 K. The raw PL signal is plotted with circles and the background taken near the defect in plotted in gray circles. The black solid line is fitting background corrected data (in dashed line) with the usual saturation function: $I_{sat}/(1 + P_{sat}/\mathrm{P})$.

where $\eta$ is the overall detection efficiency in our experiments. The rate $\Gamma_{12}$ is proportional to the optical excitation power $P$ ($\Gamma_{12} = \alpha \cdot P$). Additionally, the recombination rate $\Gamma_{21}$ includes a radiative and non-radiative part associated with the rates $\Gamma_R$ and $\Gamma_{NR}$, respectively. By definition, the sum $\Gamma_R + \Gamma_{NR}$ is equal to the inverse of the excited state lifetime and the quantum efficiency of the emitter can be defined as $\eta_{QE} = \Gamma_R/(\Gamma_R + \Gamma_{NR})$ which results in $\Gamma_R = \eta_{QE}/\tau$, with $\tau$ the excited state lifetime. Thus the dependence of the PL intensity as a function of the optical power is given by:

$$I_{PL} = \frac{\eta \cdot \eta_{QE}}{\tau} \cdot \frac{1}{1 + \frac{\Gamma_R + \Gamma_{NR}}{\Gamma_{12}}} = I_{sat} \frac{1}{1 + \frac{\Gamma_R + \Gamma_{NR}}{\alpha \cdot P}} = I_{sat} \frac{1}{1 + \frac{P_{sat}}{P}} = I_{sat} \frac{P}{P + P_{sat}} \tag{2.12}$$

with $\mathrm{I}_{sat}$ the maximum collected PL intensity at saturation defined as $\eta \cdot \eta_{QE}/\tau$ and $\mathrm{P}_{sat}$ the saturation power proportional to $\Gamma_R + \Gamma_{NR}$. For a three-level system such as the one presented in figure 2.10(b), we have $n_2(\infty) = \frac{1}{1 + \frac{\Gamma_{21} + \Gamma_{23}}{\Gamma_{12}} + \frac{\Gamma_{23}}{\Gamma_{32}}}$. Then, the PL intensity take the form $I_{sat} \frac{P}{(1+K_{NR})P + P_{sat}}$ with $P_{sat}$ proportional to $\Gamma_{21} + \Gamma_{23}$ and a non-radiative term $K_{NR} = \frac{\Gamma_{23}}{\Gamma_{32}}$, close to the one expressed for the two-level system.

To perform these fits, the background counts was subtracted from the total PL intensity $I_{PL}$ recorded on the defect. We observe that the two- and three-level system model fit extremely well the saturation curve of the defects, showing that the power dependence of the PL signal intensity is well accounted for with two or three electronics states for the SD defects. The behaviour of the saturation curves can then be explained. For low power $P << P_{sat}$, the PL intensity increases linearly with optical power ($I_{PL} \approx I_{sat} \frac{P}{P_{sat}}$). Then when the excitation rate $\Gamma_{12}$ is much greater than the desexcitation rate $\Gamma_{21}$ (i.e. $\mathrm{P} >> P_{sat}$), the PL intensity becomes equal to $I_{sat}$, and

we reach a saturation plateau of the counts. Here, all single-photon emitters present a bright emission under green optical excitation with a PL intensity at saturation of 13(1), 7(1), 16(1), 30(1), 48(1), 38(1) kcounts/s for SD-1 to SD-6 respectively as shown in figure 2.14.

These PL count rates are high considering the poor quantum efficiency of our detectors (only 10%) and that we collect, for optimal dipole orientation and position, at best 2% of the emitted photons due to the high refractive index of silicon (n ≈ 3.5) [21]. This can be explained by a short excited state lifetime that induces fast optical cycles, as well as a high quantum efficiency as we will see later.

### Evolution of the photon count rate with temperature

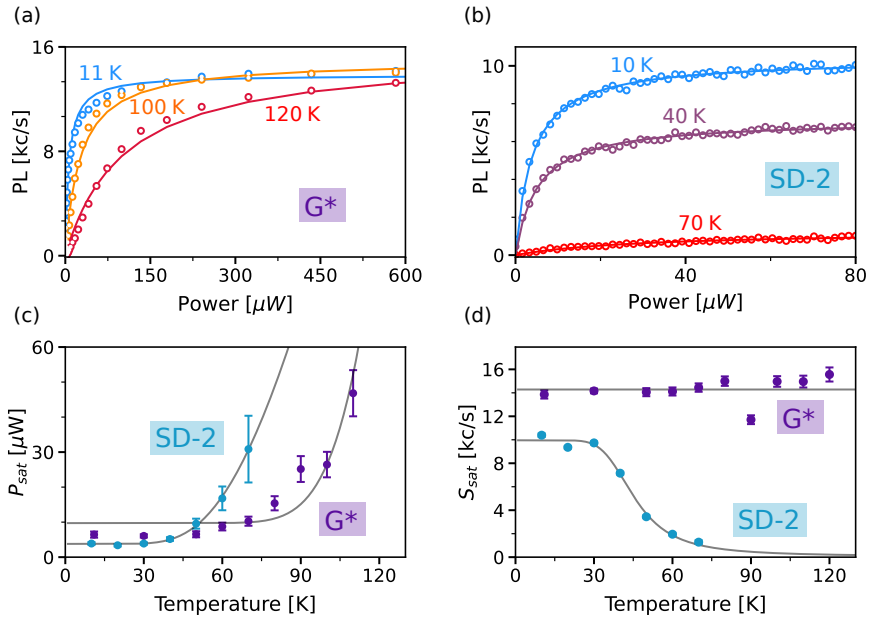


**Figure 2.15:** Evolution of the optical saturation curves with temperature. (a),(b) Background-corrected PL saturation curves measured respectively on a single G* defect and a single SD-2 defect for different temperatures. Data are fitted with Eq. (2.12) to extract the saturation power $P_{sat}$ and intensity at saturation $I_{sat}$. (c), (d) Corresponding evolution of $I_{sat}$ and $P_{sat}$ with temperature for the G* (purple) and SD-2 (blue) defects. The solid line for the G* data is a guide for the eye.

Next, we analyse the PL saturation curves as a function of temperature. Similarly to the ZPL energy statistics, we focus here on the most frequent families, namely G* and SD-2. Figures 2.15(a) and (b) display the saturation curves at different temperatures for two single G* and SD-2 defects, respectively. At a given temperature, the saturation curves follow the previously described phenomenology of a two-level system. However, their behaviour with temperature differ greatly. $I_{sat}$ remains constant with increasing temperature for G*, while for SD-2 it decreases significantly. The solid lines correspond to the data fitted by equation 2.12. From these fits, we can extract $P_{sat}$ and $I_{sat}$ as a function of temperature for the two defects.

In figure 2.15(c), a rise of $P_{sat}$ with temperature is observed. This behavior results from the

thermal activation of non-radiative decay channels, as evidenced by the decrease of the excited state lifetimes at elevated temperatures [18]. This evolution of $P_{sat}$ with temperature T is fitted using an Arrhenius fit [18]:

$$a + b.exp\left(\frac{-E_{a1}}{k_B.T}\right) \tag{2.13}$$

with $k_B$ the Boltzmann constant, $a$ and $b$ as fitting parameters, and $E_{a1}$ the activation energy. From this fit, the values $a^{(SD-2)} = 3.8 \pm 0.3$ $\mu$W, $b^{(SD-2)} = 1.6 \pm 0.3$ mW, $E_{a1}^{(SD-2)} = 25 \pm 1$ meV and $a^{(G*)} = 10 \pm 2$ $\mu$W, $b^{(G*)} = 0.5 \pm 0.5$ W, $E_{a1}^{(G*)} = 88 \pm 12$ meV are extracted for SD-2 and G* defects, respectively. The greater value of the activation energy $E_{a1}$ for G* indicates that the non-radiative channels activates at higher temperature than the SD-2 defects. The most striking feature is related to the PL intensity at saturation. We see in figures 2.15(b,d) that for the SD-2 family, $I_{sat}$ drops quickly above 30 K while for the G* defect, it stays constant well above the 77 K liquid nitrogen temperature. As the PL counts mirror the ES population of the emitters, this indicates that the G* defects behave as a closed system when the temperature rises, whereas the SD-2 defects are coupled to their environment.

Next, the polarization of the emitted photons will be investigated.

### 2.3.3 Polarization of the single photons

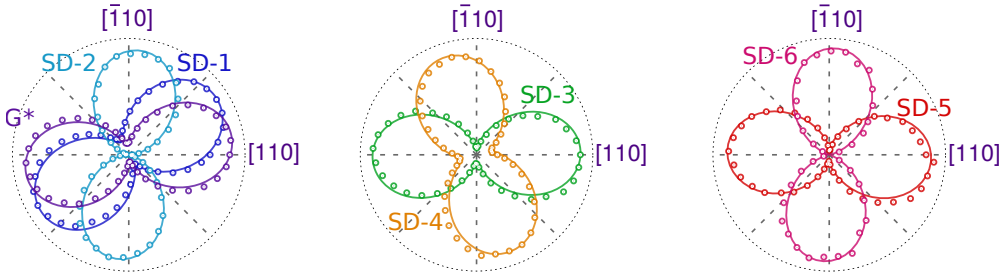


**Figure 2.16:** Emission polarization diagram measured on single defects from all SD families. The photoluminescence signal is corrected from background counts.

We now present measurements of the polarization of the photons emitted by single defects belonging to families SD-1 to SD-6. This is carried out by installing a half-waveplate and polariser in front of the single photon detectors. The polarization diagrams shown in figure 2.16 are obtained by rotating the half-waveplate while recording the PL at a temperature of 30 K after subtracting the unpolarized background light. The resulting PL intensity is fitted by the equation:

$$I(\theta) = I_{max}[Vcos^2(\theta - \phi) + (1 - V)] \tag{2.14}$$

with $I_{max}$ the maximum PL, $\phi$ the main polarization angle of the emission compared to the [110] crystal direction and $V$ the visibility which is defined by the formula $V = (I_{max} - I_{min})/I_{max}$ where $I_{max}$ and $I_{min}$ are the extrema of the PL signal intensity. All defects display a visibility close to unity. These are the characteristic associated with linearly polarized photons associated

with a single emission dipole [93]. For SD-1, 3 and 4, the visibility inferior to the unity is due to polarization distortion induced by the set-up for polarizations that are not parallel to the [110] or [1$\bar{1}$0] crystal direction. We add that the dipole orientation angle $\phi$ inside a given family can vary from defect to defect. For the SD defects, due to our small defect number, a relevant dipole angle distribution could not be established. However, a study on the dipole orientation angle was performed on G* in reference [21], revealing that the emission dipoles are orientated along specific directions divided in four subgroups that exclude the [110] and [1$\bar{1}$0] axis. These preferential directions could help in the identification of its microscopic structure.

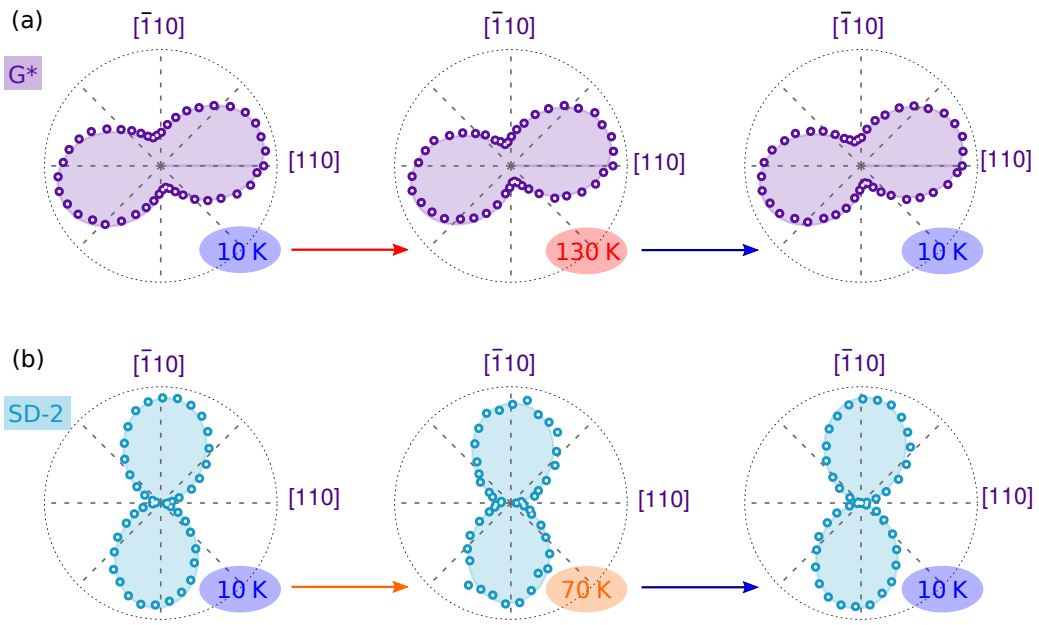


**Figure 2.17:** Emission diagram measured at different temperatures on a single G* (a) and SD-2 (b) center.

Atomic displacement or reconfiguration of a defect might occur at high temperature. This structural change could impact the emission dipole. To probe this potential effect, we measured the emission polarization diagram of the G* and SD-2 defects at 130 K and 70 K, respectively and observed no change (see figure 2.17). Similar results were obtained after successive thermal cycles of the cryostat (up to 300 K). For G*, the lower PL contrast observed is due to an imperfect background correction, added to the set-up polarization distortion. We note that interstitial carbon defect is known to be mobile at room temperature, this finding further indicates that SD-2 might not related to the interstitial carbon defect.

Next, the measurements of the excited state lifetime will be performed on the SD families using time-resolved PL experiments.

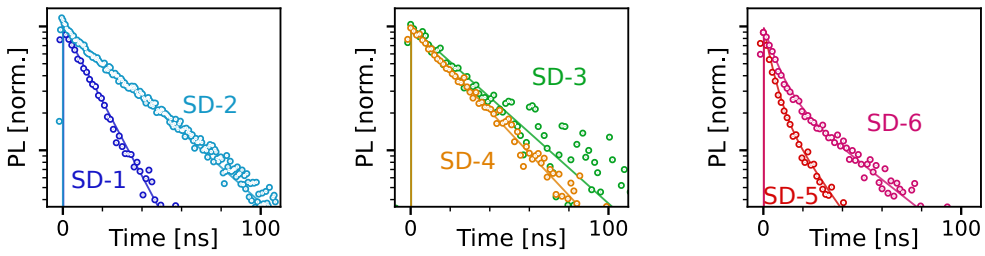


**Figure 2.18:** Time-resolved PL decay recorded on the same defects under 50 ps pulse excitation at 532 nm. The excited-state lifetime is extracted by fitting the data with a single exponential function (solid line).

### 2.3.4 Excited-level lifetimes

Analyzing the PL decay as a function of time after a 532 nm pulse excitation allows us to probe the relaxation dynamics of these individual single-photon emitters. The time-resolved PL traces are recorded by constructing the histogram of the detected photons after the pulsed photo-excitation of the defect. Such measurements, shown in figure 2.18, were performed on all SD families.

We observe a monoexponential decay associated to a single excited state lifetime ranging between 14 to 30 ns for the families G* to SD-4. Specifically, an excited state lifetime of 14.4(4), 30.6(5), 30(1), and 26(1) ns was measured for SD-1, SD-2, SD-3 and SD-4 defects, respectively. In contrast, families SD-5 and SD-6 feature a biexponential decay with a short lifetime of 4.4(7) and 6.7(8) ns and long lifetime of 19(5) ns and 35(4) ns, respectively, indicating potential additional electronic levels. The excited lifetime of G* centres was previously measured to be 32(1) ns [21].

All these values are orders of magnitude shorter than the ones measured erbium dopants [94] or T centers [73]. This shows that the SD emitters have fast optical cycles, which, coupled with good quantum efficiency, could possibly lead to efficient single photon sources.

#### Quantum efficiencies

Knowing the ES lifetime $\tau$ and the PL intensity at saturation $I_{sat}$, we can now estimate a lower bound to the quantum efficiency of these defects (which quantifies the probability of emitting a photon once it has been prepared in its excited state) with the formula $\eta_{QE} \geq \tau \cdot I_{sat}/\eta^{max}$ with $\eta^{max}$ the set-up overall detection efficiency that will now be detailed. The quantum efficiency of the set-up $\eta$ is the product of (i) the collection efficiency (i.e. the proportion of light collected by the microscope objective), (ii) the transmission of the optical set-up from the objective to the detector ($T_{set-up} = 40\%$) and (iii) the quantum efficiency of the detectors ($\eta_{det} = 10$ %). By considering the maximum collection efficiency (corresponding to the dipole orientation of the emitter that maximize the collection of the photons, that is parallel to the sample surface), a lower limit of the quantum efficiency can be estimated. With an estimated overall detection

efficiency of our set-up measured at $\eta^{max} = 2 \times 10^{-3}$ [21], we obtain a quantum efficiency at least equal to 13(1), 11(1), 35(1), 47(1), 14(1) and 17(1) % for the SD-1, SD-2, SD-3, SD-4, SD-5 and SD-6, respectively. For the G* centre, its quantum efficiency was estimated to be $\eta_{QE} \gtrsim 50\%$ in reference [21]. Consequently, these defects are already good candidates to develop bright Si-based single-photon sources even without requiring PL enhancement by Purcell effect [95].

## Conclusion

In this chapter, we have shown that carbon-implanted silicon-on-insulator can host several families of individual colour centres in the near infrared range. These single emitters display a wide diversity of bright, linearly polarized single-photon emission, some even matching the O and C telecom bands. Furthermore, some single defects exhibit additional appealing properties, such as a small spread of the ZPL energies or a strong PL intensity well above the liquid nitrogen temperature. We also specified that the G* defect is different from the G centre from spectral studies and ES lifetime measurements. However, the lack of a selective and efficient process to create these defects is a limitation to their use in integrated photonic or quantum technologies. Additional works will be required to develop a reproducible and deterministic creation method. In addition, the unidentified microscopic structure precludes theoretical support, stressing the need for additional experimental and theoretical work.

In the next chapter, we will examine a common point defect in silicon, the G centre. Unlike SD defects, its microscopic composition and structure is known. Besides, the creation process and detection of these defects at single scale will be studied.

Chapter 3

# Creation and detection of single G centres

## Contents


**3.1 The G centre in silicon . . . . . 50**
3.1.1 Optical properties . . . . . 50
3.1.2 Microscopic structure . . . . . 52
3.1.3 Electronic level structure . . . . . 54
**3.2 Single G centres creation by ion implantation . . . . . 56**
3.2.1 Sample fabrication and analysis before the implantation process . . . . 56
3.2.2 From ensembles to single defects . . . . . 59
**3.3 Investigating the photon emission of single G centres . . . . . 64**
3.3.1 Single G centre photophysics . . . . . 65
3.3.2 Defect reorientation inferred from the polarization diagram . . . . . 67
3.3.3 Fine structure in the zero-phonon line . . . . . 72
**3.4 Conclusion . . . . . 74**


## Introduction

The G centre in silicon is a complex defect composed of two carbon atoms with an interstitial silicon atom. In microelectronics, as carbon atoms are a major contaminant, this defect has been frequently observed in silicon samples and its presence was detrimental in manufactured silicon [22]. Consequently, this defect has been extensively studied [17, 20, 68, 96–100] in order to remove it. Later, the G centre was mainly used in optoelectronics applications as a light source in silicon to circumvent the poor intrinsic emission efficiency of silicon, such as in LED by electrical injection [101, 102]. Its sharp and bright emission line in the telecom O-band at 1280 nm [18], is an appealing property for its use in integrated photonics and telecommunications. The ZPL stems from a singlet (S=0) to singlet transition, but an optically detected magnetic resonance (ODMR) has been measured on an ensemble of G centres in 1982 [19], associated to a spin triplet (S=1) in a metastable state, allowing a potential use of the spin for quantum applications.

However, all these studies on the optical properties of G centres have been performed on ensembles, thus limiting the study of their properties. In this chapter, we will investigate the properties of single G centres. The optical properties and the microscopic structure of the G

centre as well as the electronic level structure of this defect will be introduced in the first section. Then, the creation by cross-implantation of carbon ions and protons and the isolation of G centres at single defect scale will be demonstrated in thin SOI samples in the second section. At last, the properties of individual G centres, such as the photostability, the evolution of the PL intensity with laser power, the excited state lifetime and the quantum efficiency, will be investigated. In addition, an unusual behaviour suggesting a reorientation of the microscopic structure of the defect will be evidenced by polarization measurements as well as a study of the fine structure of the optical transition at 1280 nm in the last section.

***In this chapter, the two superconducting nanowire single-photon detectors (Single Quantum Eos) with a quantum efficiency up to 80 % at 1.3 $\mu$m are used for all measurements.***

## 3.1 The G centre in silicon

The G centre has been studied extensively, in particular to remove it in silicon samples intended for microelectronics. It was detected in p- and n-type silicon samples [96] and in electron-irradiated silicon, where electron paramagnetic resonance was measured [97, 98]. In 1990, the comprehensive work of Watkins' group led to the determination of the microscopic model of the G centre still in use nowadays [20, 68]. The calculation of the spectrum of the electronic levels led to different ab initio methods [103–105]. In 2021, the electronic level structure of the defect was determined by first-principles calculations [106] with excellent agreement with recent measurements on the fine structure of the ZPL of the G centre in isotopically purified $^{28}$Si [70].

We will first present the optical properties of the G centre in silicon inferred from ensemble measurements in the first section, then its microscopic structure will be described in the second section. Lastly, the electronic level structure will be explained in the third section.

### 3.1.1 Optical properties

*Origin of the G centre*:

In 1971, luminescence studies of electron-irradiated silicon samples led to the PL spectrum shown in figure 3.1(a). This PL spectrum exhibits several optical lines labelled from A to G [84]. The names G centre and "G line" come from this labelling, as does the "E line" which was later associated with the same defect [99]. The other lines are related to other defects. Henceforth, the "G line" will be referred to as the ZPL of the G centre while the "E line" will be referred to as a local vibration mode (LVM) of the G centre.

*PL spectrum of the G centre*:

Figure 3.1(b) displays the typical PL spectrum at T=30 K recorded on a dense ensemble of G centres in a carbon-implanted silicon sample [18]. On this PL spectrum, we identify the two

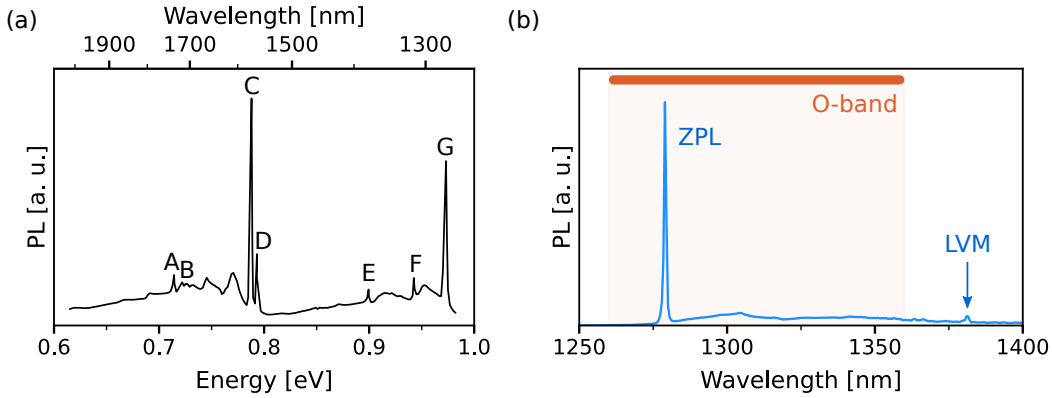


**Figure 3.1:** (a) PL spectrum recorded at a temperature of 34 K in a 80 ohm-cm n-type pulled silicon, phosphorus doped, irradiated with $10^{17}$ el./cm$^2$ at 2.5 meV, adapted from [84]. (b) PL spectrum of G centres ensemble recorded at a temperature of 30 K. The two main spectral features of the G centre, the "G line" at 1280 nm corresponding to the ZPL of the defect, and the "E line" corresponding to a LVM of the defect, are indicated in blue text. The telecom O-band is superimposed on the PL spectrum in orange to illustrate the matching with these wavelengths.

main spectral characteristics of the G centre, the sharp ZPL located at 1279 nm (969 meV) with its lateral PSB which includes an emission line located at 1381 nm (897 meV), associated with the LVM of the G centre with an energy of 72 meV. A DW factor of 18 % at 10 K was measured on ensembles in a carbon-implanted SOI sample [18], slightly more than for the G* centre (see chapter 2) where the DW factor is around 15 % [81]. Most of the photons in the PL spectrum overlaps with the O-band, ranging from 1260 nm to 1360 nm (as indicated in figure 3.1(b) by the vertical orange line at the top of the PL spectrum), a feature that is favourable for quantum communication applications.

*Luminescence of the G centre*:

The ZPL of the G centre stems from a singlet (S=0) excited state to singlet (S=0) ground state transition. The lifetime of the excited state of ensemble of G centres was measured in carbon-implanted SOI sample at 5.9 ns [18]. In addition, as previously mentioned, an optically detected magnetic resonance (ODMR) was measured on ensemble of G centres indicating the presence of a spin-triplet (S=1) metastable state [19].

*Fine structure of the ZPL*:

The ZPL fine structure of G centres was recently revealed at a temperature of 1.4 K by C. Chartrand, et al [70] thanks to measurements in an ultrapure isotopically purified $^{28}$Si (99.995 %) sample (from the Avogadro project [107]). Isotope-related inhomogeneous broadening [108] was suppressed, and the sample was fixed to be strain free. Figure 3.2(a) displays a very high resolution absorption spectra of G centres. A quartet structure with a 1:2:2:1 intensity ratio and an energy splitting $\delta$:2$\delta$:$\delta$ is observed on this figure. The origin of this fine structure stems from the motion of the centre of mass of the defect.

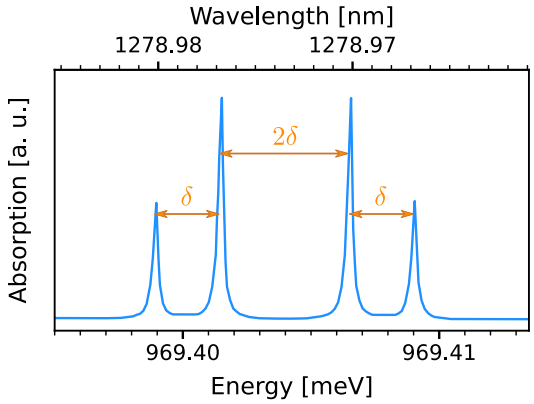


**Figure 3.2:** (a) Absorption spectrum recorded in a G centres ensemble in a $^{28}$Si sample at a temperature of 1.4 K displaying the fine structure of the ZPL of the G defect, adapted form [70]. Added in orange are the energy splitting [70, 106].

We next present the microscopic structure of the G centre.

### 3.1.2 Microscopic structure

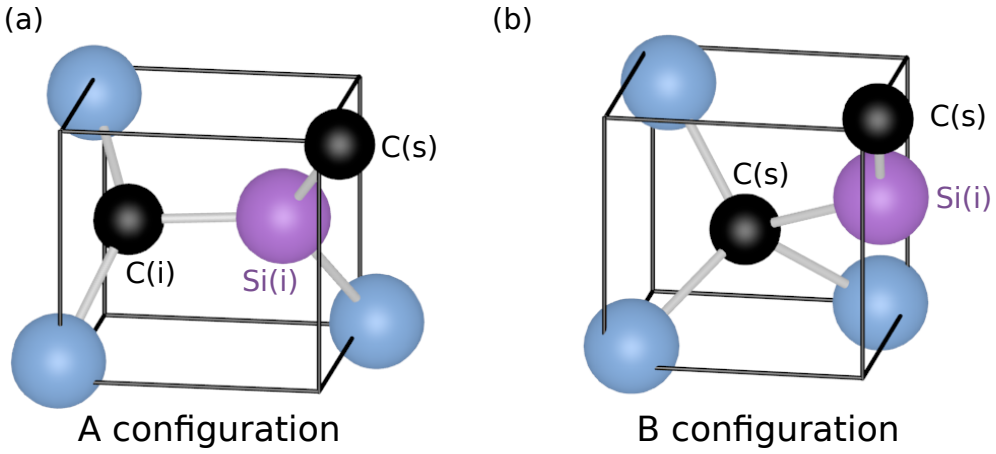


**Figure 3.3:** Microscopic structure of the G centre, represented on a cube of length a/2, i.e. one eighth of the main cube. (a) The configuration labelled as A with a C(i)-Si(i)-C(s) structure. (b) The configuration labelled as B with a C(s)-Si(i)-C(s) structure. The carbon atoms are represented in black, the interstitial silicon atom is represented in purple and the silicon atoms of the lattice are represented in blue. C(s) stands for carbon substitutional, C(i) for carbon interstitial and Si(i) for silicon interstitial.

*Two microscopic configurations*:

The G centre consists of two carbon impurity atoms and an interstitial silicon atom [20]. The numerous studies made on the G centre have shown that it possesses more than just one microscopic structure [17, 20, 68, 99, 100]. Two microscopic structures have been observed

experimentally and depend on the charge state and/or the doping level of the silicon. The A form for which no luminescence was reported in the literature, and the B form which is the one giving the PL with a ZPL at 0.97 eV. The microscopic structure of the A form is displayed in figure 3.3(a) with an interstitial carbon C(i) paired with an interstitial silicon Si(i) occupying a node in the silicon lattice accompanied by a substitutional carbon C(s) [20, 68]. This A form is stable in its odd charge state (+ or -) and possesses a monoclinic (C1h) symmetry along a <111> axis [99].

Alongside this A form, the microscopic structure of the B form is displayed in figure 3.3(b) with two substitutional carbon C(s) and an interstitial silicon Si(i). The Si(i) atom is positioned at equal distance of the two C(s) atoms, with an angle $\widehat{CSiC}$ equal to 143°. It can take six equivalent positions along the three equivalent planes {110} formed by the two C(s) atoms and the Si(i) atom and containing the <111> axis [20]. The B form is the stable conformation in the neutral state of this defect.

We also mention that a complex bistability has been observed, allowing conversion from one form to another by changing the charge state or inducing an optical excitation, or changing the temperature [68]. The mechanism behind this bistability was assigned to a switching molecular bond, inducing the change of configuration between the A and B forms, very close in energy [68].

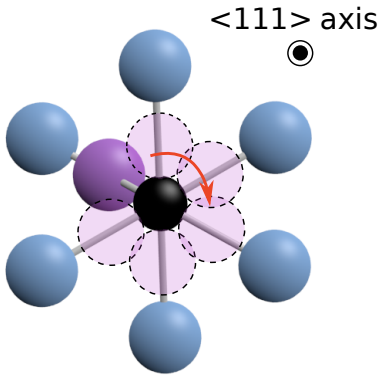


**Figure 3.4:** Reorientation of the G defect in the B configuration. Schematic showing the six positions of the Si(i) atom (dashed purple circles) in the plane perpendicular to the <111> axis. The color code of the atoms is the same as in figure 3.3.

*Reorientational motion of the Si(i) atom*:

In the B configuration, a reorientational motion of the Si(i) atom has been observed by EPR and ODMR measurements [19, 20]. This reorientation of the Si(i) atom is illustrated in the figure 3.4, representing the defect in a view perpendicular to its main <111> axis. The Si(i) atom hops around the <111> crystal axis on the six equivalent positions (displayed in dashed line in figure 3.4) that are aligned with the six closest neighbour silicon atoms of the lattice. This hopping occurs by tunnelling of the Si(i) atom between the six equivalent positions. The tunneling rates can be increased by acoustic phonons at elevated temperatures [106]. In a given

position of the Si(i), the B form (like the A form) displays a monoclinic ($C_{1h}$) symmetry [99] along the <111> axis, but with the motional averaging of the reorientation around the <111> axis observed at high temperatures [20, 100], the symmetry of the defect becomes $C_{3V}$.

This reorientation, which leads to a relocation of the centre of mass of the defect for each interstitial silicon position, will have an impact on the electronic level structure of the defect, which is discussed next.

### 3.1.3 Electronic level structure

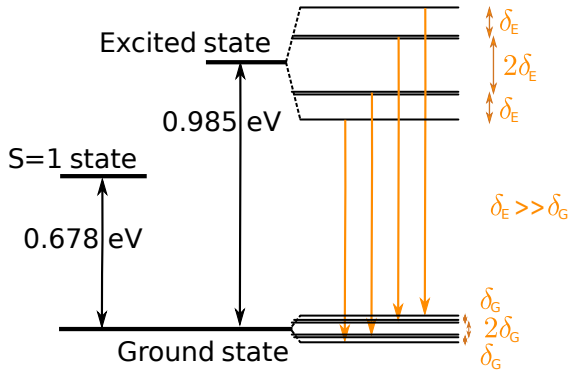


**Figure 3.5:** Schematic of the ground and excited level structure of the G centre. The hopping of the interstitial silicon results in a quartet structure in the GS and ES [106]. The optical transitions are represented with orange arrows.

The electronic structure was recently determined by first-principles calculations with a total energy difference for the singlet to singlet transition of 0.985 eV and for the singlet to triplet transition of 0.678 eV [106], as shown in figure 3.5. The calculations evidence that the electronic properties of the defect depend on the position of its centre of mass, because the central Si(i) atom of the defect can be located in six equivalent sites. The central S(i) atom can tunnel from one site to the adjacent one, thus lifting the sixfold degeneracy of each electronic level. In solid state physics, the nuclei are first considered frozen (Born-Oppenheimer approximation) and then the coupling to the vibrational excitations is introduced as a perturbation through the electron-phonon interaction. The equivalent of the Born-Oppenheimer approximation would be here a fixed Si(i) at one of the six positions. Here there is no vibrational excitation but a rotational one linked to the rotational degree of freedom of the defect centre of mass. The tunneling of the Si(i) is predicted to affect the singlet ground state, singlet excited state and triplet excited state [106]. We add that in the triplet excited state, the positions of the six equivalent sites of the Si(i) have been calculated to be energetically stable with an angular shift of 30° compared to the singlet excited state [106].

In a G centre, the electronic wave function $\Psi(\vec{r})$ can be written as the product of the wave

function of the centre of mass $\varphi\left(\overrightarrow{R_{MC}}\right)$ and the wave function of the electronic cloud relative to the centre of mass $\phi\left(\vec{r}-\overrightarrow{R_{MC}}\right)$:

$$\Psi\left(\vec{r}\right)=\varphi\left(\overrightarrow{R_{MC}}\right)\cdot\phi\left(\vec{r}-\overrightarrow{R_{MC}}\right) \tag{3.1}$$

The wave function of the centre of mass can be written as a Bloch function in the tight-binding approximation for a periodic potential as:

$$\varphi(x)=\frac{1}{\sqrt{N}}\sum_{n=1}^{N}e^{jkna}\xi(x-na) \tag{3.2}$$

with N=6 (corresponding here to the 6 sites), $a$ the period of the potential, $k$ the wave-vector introduced in the Bloch function and $\xi$ the wave function describing the position of the Si(i) atom in an isolated potential. From the time-independent Schrödinger equation $H\left|\varphi\right\rangle=E\left|\varphi\right\rangle$ and $\left|\varphi\right\rangle=1/\sqrt{N}\sum_{n=1}^{N}e^{jkna}\left|n\right\rangle$ with $\left|n\right\rangle$ the states in Dirac notation related to the wave-function $\xi(x)$ ($\langle x|n\rangle=\xi(x)$), we can determine the eigen-energies of the Si(i) atom by projecting $\langle p|$ on the Schrödinger equation. With $\langle n|H\left|n\right\rangle=E_0$ and $\langle n|H\left|n\pm1\right\rangle=\delta$ the tunneling probability, we obtain:

$$\begin{aligned}&\langle p|H\left|\varphi\right\rangle=\langle p|E\left|\varphi\right\rangle\\&\Leftrightarrow E_0+\delta e^{jka}+\delta e^{-jka}=E\\&\Leftrightarrow E=E_0+2\delta cos(ka)\end{aligned} \tag{3.3}$$

Then, with the Born-von Karman boundary conditions:

$$\begin{aligned}&e^{jkNa}=1\\&\Leftrightarrow kNa=2\pi m\quad(m\in\mathbb{N},m=[0;5])\\&\Leftrightarrow k=\tfrac{2\pi m}{Na}\\&\Leftrightarrow k=m\tfrac{\pi}{3a}\quad\text{since } N=6\end{aligned} \tag{3.4}$$

We finally get the energies:

$$E_m=E_0+2\delta cos\left(m\frac{\pi}{3}\right) \tag{3.5}$$

From the 6 values of m, we obtain four energies ($E_0+2\delta$, $E_0+\delta$, $E_0-\delta$ and $E_0-2\delta$) with a 1:2:2:1 degeneracy.
The selection rules for dipolar transitions are given by:

$$\langle\Psi_f|-\vec{d}.\vec{E}\left|\Psi_i\right\rangle=\langle\varphi_f|\varphi_i\rangle\cdot\langle\phi_f|-\vec{d}.\vec{E}\left|\phi_i\right\rangle \tag{3.6}$$

Since $\langle\varphi_f|\varphi_i\rangle=\delta_{m_f,m_i}$ where $\delta$ is the Kronecker symbol, the azimuthal quantum number m is conserved in the transition, thus the rotational state cannot change during an optical transition.

To resume, in the low temperature regime, the tunneling of the Si(i) atom, coinciding with the centre of mass of the G centre, between 6 equivalent positions results in a quartet structure with a 1:2:2:1 degeneracy. The $\delta$:2$\delta$:$\delta$ energy splitting calculated in ref. [106] (with $\delta$ the tunneling rate between two positions of the Si(i)) can be interpreted with a simple tight-binding model. Instead of 4x4 transitions between the ground and excited state quartets, the selection rule of conservation of rotational quantum number reduces this number to only 4 transitions. If $\delta$ was

the same for the ground and excited states, only one line would be observed experimentally. Ab initio calculations show that $\delta_E = 2.5\ \mu$eV $>> \delta_G$ so that 4 lines are finally detected, thus explaining the results of Chartrand et al., where the quartet experimental splitting is essentially determined by $\delta_E$.

All the studies of G centres were up to now only accomplished at the ensembles level. In the following section, we demonstrate the creation of single G centres by using cross-implantation with carbon atoms and protons at low fluences.

## 3.2 Single G centres creation by ion implantation

As demonstrated in the previous chapter, silicon hosts several families of isolated colour centres emitting in the NIR. Their optical isolation has been achieved with a reproducible creation procedure, but without control of the emitter densities. It is however crucial to master this individual defect creation step for two reasons. Firstly, to improve and facilitate the optical study of these defects at the individual defect level. And secondly, to ensure the deterministic integration of an individual colour centre into an optical photonic microstructure to build quantum photonic devices.

To address this problem for the G centre, a study on the fabrication of single G centres in silicon was performed during my thesis. This defect can be created by carbon implantation followed by flash annealing and proton irradiation, and a control of the implantation parameters allows a decrease in its density [18]. Thus, as the goal is to find the appropriate parameters to reach the regime that allows the creation of single defects, a local co-implantation of carbon ions and protons with varying fluences on a SOI wafer has been performed. A cross-implantation scheme was chosen to explore a wide range of G centre densities for different combinations of carbon and proton fluences, with the reduction in implantation fluences allowing a gradual transition from dense ensembles of G centres to dilute arrays.

In the first section, optical control experiments of SOI wafers either pristine or after only flash annealing at 1000°C are performed to determine the presence or absence of native G centres in these samples. We specify here that the term native defects corresponds to defects present in the samples before any implantation process. In the second section, the cross-implantation of carbon ions and protons is studied by performing optical scans, PL spectra and intensity-correlation experiments.

### 3.2.1 Sample fabrication and analysis before the implantation process

The studied SOI samples are presented in the first section, and preliminary studies are performed on reference samples to assess the presence of emitters in virgin samples in the second section.

### Cross carbon and proton implantation of silicon samples

*Wafer sample*:

The investigated wafer consists of a $^{28}$Si epilayer grown on an etched commercial SOI wafer. Isotopically purified silicon $^{28}$Si is used in order to have a nuclear spin-free host matrix for optically active defects [108] and also to avoid isotope-related inhomogeneous optical broadening [70]. The wafer is created by first thinning the upper Si layer of the commercial SOI down to 4 nm by thermal oxidation, followed by wet chemical etching with hydrofluoric acid. Then the layer of $^{28}$Si is grown on top of the etched SOI by chemical vapor deposition following the method described in reference [109]. The resulting wafer is therefore composed of a stack of a 56 nm thick layer of $^{28}$Si on top of a 4 nm thick layer of natural Si. Under the 60 nm of natSi/$^{28}$Si is the rest of the commercial SOI, composed of a 145 nm thick layer made of natural silicon oxide that separates the top part from the substrate as shown in figure 3.6(a). This wafer is then cut into 5×5 mm$^2$ pieces to produce the samples studied in this chapter.

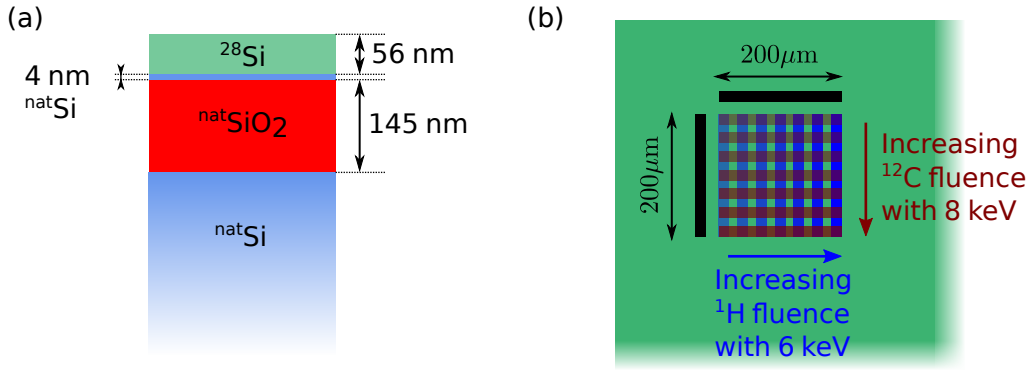


**Figure 3.6:** (a) Schematic of the silicon-on-insulator (SOI) sample used in this chapter. The top silicon layer is an isotopically purified $^{28}$Si layer. (b) Schematic top view of the $^{28}$SOI sample displaying the implantation map. A rectangular pattern is repeated while increasing the fluences for both carbon ions and protons, thus shaping the cross implanted area. The carbon implantation is operated at 8 keV and the proton irradiation at 6 keV. The seven fluences range from 3×10$^{13}$ cm$^{-2}$ down to 3×10$^{10}$ cm$^{-2}$ for both carbon and proton. The black stripes on the left and top of the implant area are markers.

*Implantation steps*:

The procedure for creating G centres is the following: A first implantation with carbon ions is operated, then to heal the silicon lattice from the implantation damage, the sample is subjected to a flash annealing at 1000°C during 20 s under $N_2$ atmosphere, and then the irradiation step with protons follows [18, 110]. The implantation of carbon ions and protons are performed using a beam of accelerated ions sent through a mask, by our collaborators Tobias Herzig and Sébastien Pezzagna at the University of Leipzig, Germany. All annealing steps are carried out by our collaborators Mario Khoury and Marco Abbarchi at IM2NP in Marseille, France. The grid pattern is made by a 10 $\mu$m thick mica mask with a 20x200 $\mu$m$^2$ aperture on the samples

positioned at 4.5 mm from the sample. The mask is moved to implant the 7 vertical carbon-implanted stripes as well as, after the flash annealing, the 7 horizontal proton-irradiated stripes that will overlap the carbon lines as shown in figure 3.6(b). All of the stripes are separated by around 10 $\mu$m. The resulting 7x7 implantation grid allows to probe 49 combinations of carbon and proton doses for generating G centres (figure 3.6(b)). The energies used for the implantation are 8 keV for the carbon ions and 6 keV for the protons, while the fluences vary from 0.3 to $300\times10^{11}$ cm$^{-2}$ for both ions. The energies were determined using SRIM software so that the carbon ions stop in the upper silicon layer whereas the protons cross it while producing interstitials, and stop in the oxide layer below.

| Sample number | C implant. | HT flash anneal. | H irrad. | LT anneal. |
|---|---|---|---|---|
| #0 | no | no | no | no |
| #0.5 | no | yes | no | no |
| #1 | yes | no | yes | no |
| #2 | yes | yes | yes | no |
| #3 | yes | yes | yes | yes at 150°C |

**Table 3.1:** Labelling of the samples studied with the corresponding implantation steps.

*Presentation of the studied samples*:

To ensure that the samples prior to the implantation process do not contain G centres, a preliminary study is performed. To this end, one of the samples is kept in its virgin state (i.e. without any additional step following the $^{28}$Si epilayer growth) to serve as a reference (labelled #0, see table 3.1). In addition, to analyse the influence of the annealing step, another virgin sample (labelled #0.5, see table 3.1) did undergo only the flash annealing without any implantation, and another sample (labelled #1, see table 3.1) was implanted without the flash annealing step to complete this analysis. The sample labelled #2 (see table 3.1) went through the full implantation procedure with carbon implantation, flash annealing and proton irradiation. Lastly, the sample labelled #3 (see table 3.1) did undergo the implantation procedure with an additional low temperature annealing during 30 min under $N_2$ atmosphere, after all the implantation processes. These two last samples will be analysed in the following sections.

Before trying to create G centres by implantation, we first check that they are not natively present in the sample.

### Sample control experiments

*Study of the reference sample #0*:

We first analyse the reference sample #0, which is the sample without any implantation or annealing. Measurements of the PL intensity of the reference sample #0 give the PL map displayed in figure 3.7(a). It shows a spatially uniform background accompanied with some isolated spots of slightly higher intensity. The typical PL spectrum of these isolated spots is shown in

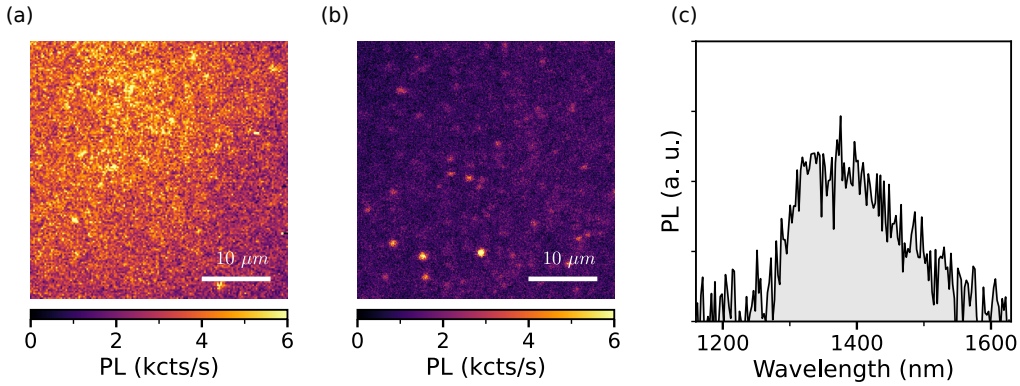


**Figure 3.7:** PL map of (a) the virgin sample (#0) and (b) the sample after a flash annealing of 20 s at 1000°C under $N_2$ atmosphere (#0.5). (c) Typical PL spectrum of the hotspots in (a) and (b). Data are recorded at 30 K under excitation at 532 nm with an optical power of 10 $\mu$W.

Figure 3.7(c). It exhibits a broad PL emission centered at ≈1350 nm and no ZPL. This emission spectrum is different from the ensemble of G centres spectrum (see figure 3.1) [18]. The presence of native G centres in the virgin SOI wafer studied here can therefore be excluded.

*Study of the reference sample #0.5*:

We also analyse sample #0.5, the one that has undergone only the flash annealing stage. In the same manner as for sample #0, a PL map of the sample was recorded and is displayed in figure 3.7(b). On this PL map, the intensity of the spatially uniform PL background is reduced by a factor close to two. Moreover, the sample also presents native hotspots, which are better resolved due to a better intensity contrast compared to the PL background of sample #0, but their intensities are similar to the isolated spots of the virgin sample #0. The PL spectrum of these hotspots does not change either. Thus, we conclude that the flash annealing alone does not contribute to the formation of G centres in silicon.

From these control experiments, we conclude that there are no native G centres in our samples and that they are not created by the flash annealing. We will now create them by implantation.

### 3.2.2 From ensembles to single defects

We now investigate the sample #2 that has been cross-implanted with the flash annealing. In the first section, the PL map of the full implanted area is examined, then PL spectra will be recorded on highly implanted areas and low implanted areas to assess the presence of G centres. In the next section, areas outside of the implantation will be explored and lastly the influence of the additional low temperature annealing will be examined.

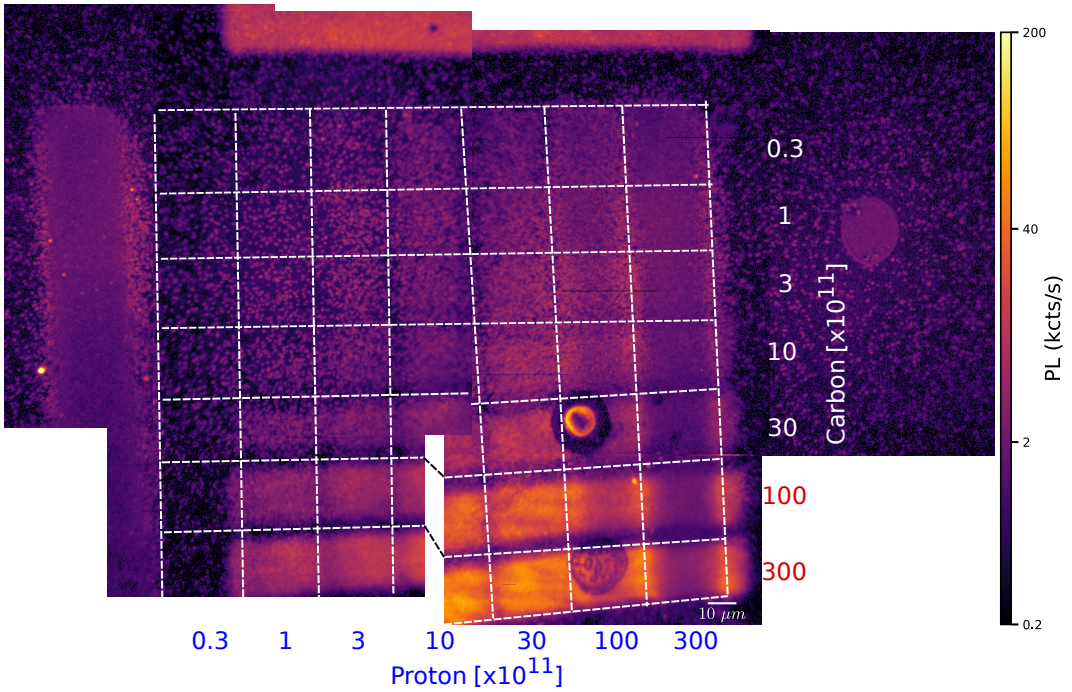


**Figure 3.8:** Reconstruction of the PL map of the entire implanted area using multiple optical scans to overcome range limitations in our scanning method. The PL intensity is plotted using a logarithmic scale for better contrast. The white lines are guides to the eyes to display the implantation grid. Fluences are indicated on the bottom for the protons and on the right for the carbon ions. Scale bar = 10 $\mu$m. Data are recorded at 30 K under excitation at 532 nm with an optical power of 10 $\mu$W.

### PL map of the implanted areas

In figure 3.8, the entire implanted area is displayed by combining multiple optical scans, which explains the discontinuity of some stripes. On the side and bottom of the PL map are indicated the corresponding fluences for the implanted lines of both ions, and the PL intensity is plotted using a logarithmic scale for better contrast. We observe that there is a significant variation in PL intensity between the different implanted squares. Two trends can be deduced: first the PL signal intensity increases monotonously with the carbon dose (from top to bottom). Secondly there is a maximum PL intensity when the proton concentration reaches $30\times10^{11}$ proton/cm$^2$ (from left to right). Above this proton fluence, a PL decrease is observed from the presence of a dark centre and bright vertical edges. This shows the harmful effect of irradiating protons at high fluences to create G centres, as previously observed for silicon wafers highly implanted with carbon ions [110]. The column at $0.3\times10^{11}$ proton/cm$^2$ (on the left) was not properly implanted due to an imprecise mask repositioning. The decrease in PL intensity for the low carbon and low proton fluences is due to the creation of more and more dilute ensembles of fluorescent defects. In these areas, the intensity of the PL signal is no longer spatially uniform with bright spots whose relative distance increases with the decrease of carbon and proton fluences.

We will now perform PL spectra on the highly implanted areas and the low implanted areas.

### Highly implanted areas

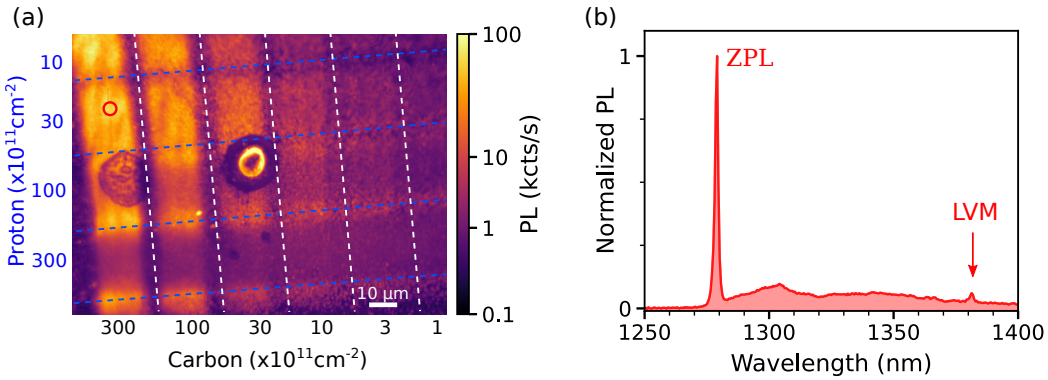


**Figure 3.9:** (a) PL map of the sample #2 cross-implanted with carbon and proton in the region of high irradiation fluences. The vertical white (horizontal blue) dashed lines are guides for the eyes separating the stripes with different carbon (proton) fluences, whose values are indicated in the bottom (left) axis. Scale bar = 10 $\mu$m. The two 20 $\mu$m large spots visible in the left middle of the scan are due to local sample imperfections. (b) Normalized PL spectrum detected for an ensemble of G centres at the position indicated by the red circle in (a). These data are recorded at 30 K under excitation at 532nm with an optical power of 10 $\mu$W.

The PL intensity map of the most heavily implanted part of our SOI sample #2 is plotted in figure 3.9(a) (rotated by 90° compared to figure 3.8). Next to the PL intensity map, figure 3.9(b) displays the PL spectrum taken on the position indicated by the red circle drawn on figure 3.9(a). This corresponds to the area of highest PL intensity. This PL spectrum exhibits a sharp ZPL at 1279 nm and a broad phonon-sideband at longer wavelengths. Both features are characteristic of the G centre in silicon, as previously reported in ensemble measurements [18]. On the PL spectrum, we also observe the so-called E-line at 1380 nm. This line corresponds to a LVM of the G centre and thus serves as a key fingerprint for the identification of this point defect [17]. These results confirm the effectiveness of a dual carbon and proton implantation method to produce G centre ensembles in a SOI wafer.

### Low implanted areas

The low irradiation region of our cross-implanted SOI is now examined. The PL intensity map of this area is shown on the figure 3.10(a). In the area implanted with carbon and proton respectively at $0.3\times10^{11}$ and $1\times10^{11}$ cm$^{-2}$, the estimated areal density of fluorescent defects is roughly 0.3 per $\mu$m$^2$.

A PL spectrum of such an isolated spot (circle on figure 3.10(a)) is recorded and displayed on figure 3.10(b). This PL spectrum is identical to the one recorded on the high fluences area as it shares the same features, such as the ZPL at 1279 nm and the local vibrational mode at 1380 nm. In contrast to G*, the PL spectrum is here exactly the same for ensembles and isolated spots, which leaves no doubt that this fluorescent spot is a G centre (see chapter 2, section 2.2.1). To test if this isolated spot is a single emitter or not, an intensity-correlation experiment

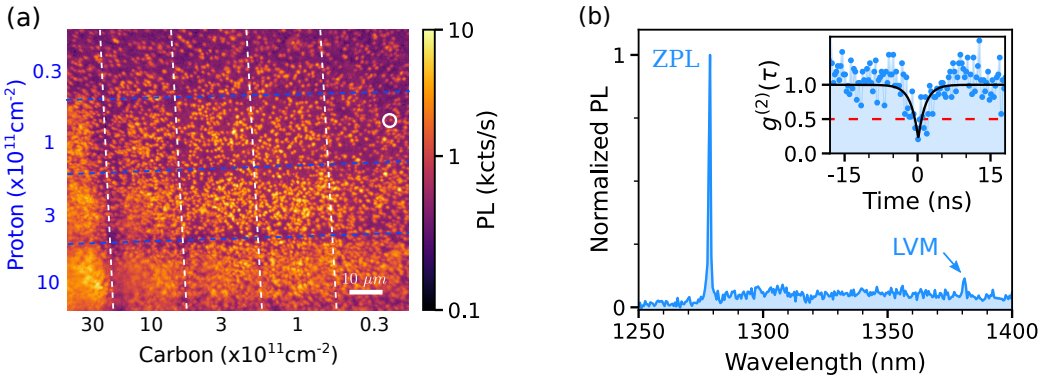


**Figure 3.10:** (a) PL map of the sample #2 in the region of low irradiation fluences. The vertical white (horizontal blue) dashed lines are guides for the eyes splitting the stripes with different carbon (proton) fluences, whose value is indicated in the bottom (left) axis. The white bar scales for 10 $\mu$m. (b) Normalized PL spectrum detected for an isolated G centre indicated by the blue circle in (a). Inset: Corresponding intensity-correlation function $g^{(2)}(\tau)$, without any correction from background or detector noise counts. The photon anti-bunching with $g^{(2)}(0) < 0.5$ evidences the emission of single photons. These data are recorded at 30 K under excitation at 532 nm with an optical power of 10 $\mu$W.

is conducted. The resulting second order autocorrelation function is displayed in the inset of the figure 3.10(b). On this figure, we observe a photon anti-bunching with $g^{(2)}(0) = 0.24(1) < 0.5$ [89], demonstrating the detection of a single G centre in silicon.

### Defects outside locally implanted areas

Regions far from the implanted area were investigated in order to complete the exploration of sample #2. In figure 3.11(a), a PL intensity map was recorded around 200 $\mu$m from the implanted area. It displays plenty of isolated spots over a dark background, similar to what was observed on the low implanted areas. An estimation of their areal density gives a value $\approx 0.1$ per $\mu m^2$, close to the one found for the low implanted area.

The PL spectrum of these emitters is then recorded to identify them, and one of them is plotted in figure 3.11(b). All these isolated defects are G centres, due to their PL spectra having the characteristic sharp ZPL at 1279 nm as well as the LVM at 1380 nm. In figure 3.11(b), the double emission line observed on the ZPL will be studied later in this chapter. Intensity-correlation experiments reveal an anti-bunching at zero delay going under 0.5 with a value of $g^{(2)}(0) = 0.19(1)$, as shown in figure 3.11(d), thus showing that the emission originates again from single defects.

The presence of defects outside the implanted region is unexpected given that the virgin sample (# 0) and the sample with only the flash annealing step (# 0.5) didn't show any G centres. Furthermore, the implantation is carried out with a mask, which should prevent the ions from reaching the sample outside the aperture. A considered hypothesis for the presence of emitters outside the implanted area was the diffusion in the sample of interstitial carbons,

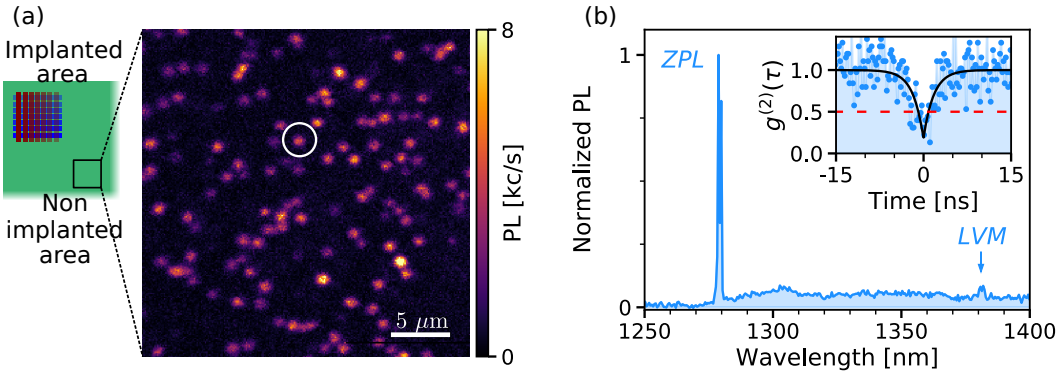


**Figure 3.11:** (a) PL scan 200 $\mu$m away from locally implanted region taken under 532 nm CW excitation laser at an optical power of 10 $\mu$W and at T=30 K. On the left, schematic of the sample to illustrate the area outside the locally implanted areas. (b) Normalized PL spectrum of a single G centre corresponding to the isolated spot surrounded by a white circle on (a). (Inset) Measurements of the second-order correlation function $g^{(2)}(\tau)$ of the same G centre, showing a $g^{(2)}(0) < 0.5$, confirming that this defect is a single G centre.

mobile at room temperature. To test this hypothesis, the same implantation was performed on a sample half covered by a silicon mask. The part covered by the silicon mask did not exhibit any PL, demonstrating that no diffusion occurs, thus eliminating this hypothesis. Two other possibilities were considered. (i) The SOI sample could get electrically charged during the implantation steps, thus bending part of the ion beam, which would result in a spreading of the ions after the mica mask. (ii) Part of the ions could cross through the implantation mask (a 10 $\mu$m thick mica piece). However, given the weak energy used for the implantation, our collaborators in Leipzig consider these effects to be very unlikely. A new implantation is planned to distinguish the other two hypotheses by placing the mica mask directly in contact with the sample. The presence of these defects outside the implanted areas are currently being investigated and further work will be needed to fully understand the creation process of these defects.

### High temperature flash annealing and additional low temperature annealing

*Impact of the flash annealing*:

Sample #1 without the flash annealing step was examined to investigate the impact of this annealing step. A PL intensity map was taken on the implanted area and is displayed on figure 3.12(a). The background is higher that in any previous PL maps, with a mean intensity around 12 kc/s. Still we can distinguish the stripes associated to the carbon implantation, while the proton stripes are not distinguishable. For the higher carbon implantation fluences (300 and $100\times10^{11}$ cm$^{-2}$), the PL quenches. At lower fluences, the PL is maximal at $30\times10^{11}$ cm$^{-2}$ and below fluences at $10\times10^{11}$ cm$^{-2}$, the PL is equal to the background. A typical PL spectra, displayed on figure 3.12(b), indicates that these emitters are mostly G centres, with few W centres with a ZPL at 1218 nm (see chapter 4). By comparing samples #1 and #2, we infer that the

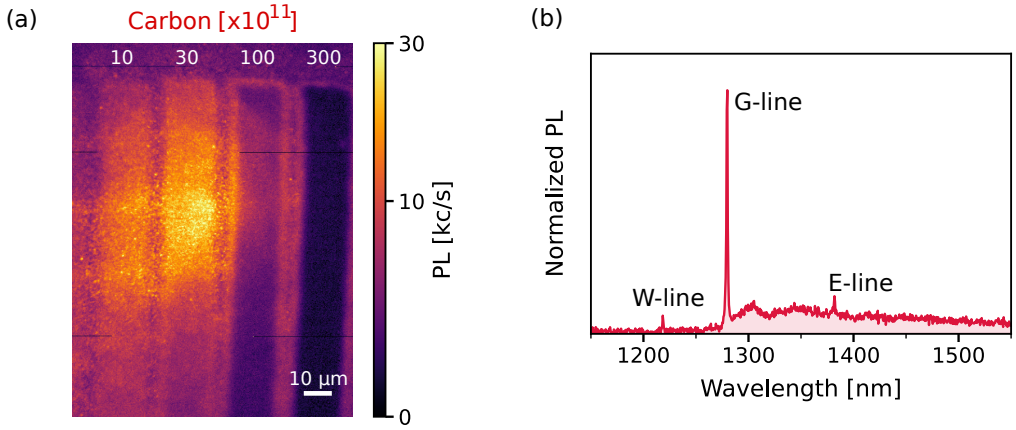


**Figure 3.12:** (a) PL map of the implanted area in sample # 1. (b) Typical PL spectrum recorded on this sample. Measurements were taken under 532 nm illumination at an optical power of 10 $\mu$W and at a temperature of 30 K.

flash annealing step favors the creation of G centres to the detriment of other defects like W centres. Additionally, a large number of emitters was observed far from the implanted area on this sample, confirming that the presence of G centres far from the implanted area comes only from the implantation steps.

*Impact of the low temperature annealing*:

To investigate the impact of an additional low temperature annealing after the implantation steps, the sample #5 was studied. We remind that sample #5 is identical to sample #2 but with an additional low temperature annealing at 150°C during 30 min under $N_2$ atmosphere. PL intensity maps taken on the implanted areas reveal that the PL is close to the ones in sample #2, except that the hotspots density decreases. This effect is also observed in areas outside the implanted area. In addition, the proportion of G centers among the hotspots is lower than in sample #2. Thus the low temperature annealing seems to decrease the density of defects as well as the density of G centres relative to the emitters created.

Despite some unresolved questions, the first isolation of G centres was demonstrated, as well as a reproducible method to create single G centres. These results enable to study the G centre photophysics at the single defect scale.

## 3.3 Investigating the photon emission of single G centres

The isolation at single defect scale of G centres allows us to further explore their optical properties without averaging effect, like in ensembles. In the first section, the photophysics of single G centres will be explored. The PL polarization will then be studied in the second section, revealing hints about the defect reorientation in the crystal. In the last section, the fine structure of the ZPL will be investigated.

### 3.3.1 Single G centre photophysics

The photostability of single G centres is investigated as well as the saturation curve in the first part. In the second part, excited state lifetime measurements will be performed, allowing us to estimate the quantum efficiency of single G centres.

#### Photostability and saturation curve

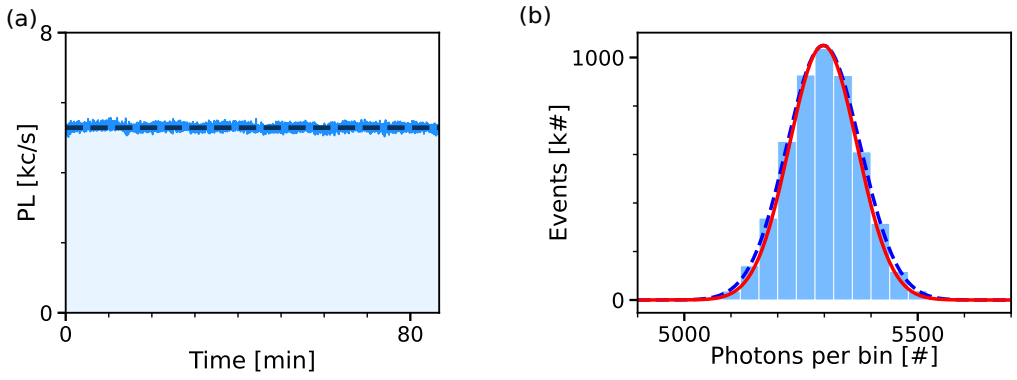


**Figure 3.13:** (a) PL time trace of a single G centre. The dashed line is the PL intensity mean value. Time bin = 33 ms. (b) Histogram of photons per bin of the PL time trace in (a). The dashed line represents a Gaussian fit of the histogram. The red solid line represents a Poissonian distribution with the mean value of the PL time trace in (a).

*Photostability*:

For acquisition times extending up to one day, no photobleaching or photoblinking of the PL signal of individual G centres was observed. To illustrate this stability, a PL time trace taken on an individual single G centre is displayed in figure 3.13(a), showing a shot noise limited PL signal and confirming that single G centres are photostable, whatever the incident optical power. Similarly to chapter 2, the histogram of photons per bins of the PL time trace is displayed in figure 3.13(b) indicating that the intensity variations of the PL time trace are shot noise limited.

*Saturation curve*:

To estimate the maximum defect count rates, saturation curves are recorded on single G centres. We remind that we use the single quantum detector with a quantum efficiency of 80 % at 1300 nm. The typical saturation curve of single G centres is shown on figure 3.14, with a raw PL signal increasing linearly with the optical power and reaching a maximum at saturation. The background, taken near the emitter, is evolving linearly with optical power. Then the background is subtracted to the raw PL signal and, as in the previous chapter, the black solid line is fitting this background corrected data with the equation 2.12.

From the fit, we extract a saturation power of $P_{sat} = 2.6(1)$ $\mu$W and a saturated intensity of $I_{sat} = 6.3(1)$ kc/s. These are typical values and the statistics made on 40 single G centres gives $< P_{sat} > = 4.5 \pm 2.1$ $\mu$W and $< I_{sat} > = 7.1 \pm 2.7$ kc/s. This maximum count rate is much

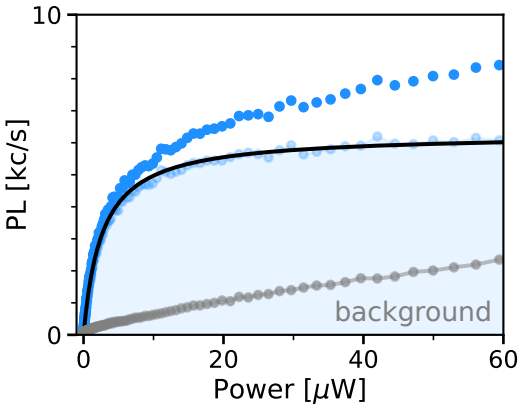


**Figure 3.14:** Standard PL saturation curve recorded on an individual G defect. The raw PL signal is plotted in blue circles and the background in plotted in gray. The black solid line is fitting background corrected data with the usual saturation function: $I_{sat}/(1 + P_{sat}/\mathrm{P})$.

lower than the one obtained on the G* defect in chapter 2 (section 2.3.2), and by taking into account the increase of the detector quantum efficiency by a factor $\approx 8$, the G centre emission is close to one order of magnitude lower than the one of G* defects.

**Lifetime measurements of single G centres**

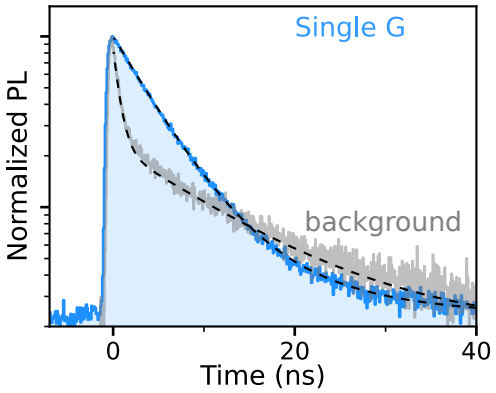


**Figure 3.15:** Time-resolved PL trace for a single G centre in the area of low irradiation fluences (corresponding to the PL spectrum in figure 3.10) acquired with a 532 nm laser pulses of duration 150 ps. The background PL decay displayed in gray.

To probe the recombination dynamics, time-resolved PL experiments are recorded under a 150 ps pulsed laser excitation at 532 nm on single G centres. The decay of the PL signal is displayed in figure 3.15 and fitted by a bi-exponential function: $A_1/\tau_1 \cdot e^{(-t/\tau_1)} + A_2/\tau_2 \cdot e^{(-t/\tau_2)}$ with $A_1$ and $A_2$ the temporally integrated intensities and $\tau_1$ and $\tau_2$ the decay times. More than 80 % (with $A_1$ / $(A_1 + A_2) = 0.82$) of the photons are emitted with a decay time $\tau_1 = 4.5(1)$ ns, close to the short lifetime measured in G centres ensembles [18]. The rest of the

photons are associated with a decay time of $\tau_2 = 12(3)$ ns. In opposition to the 4.5 ns time, this long decay time is still observed by repeating the experiment a few microns away of the isolated PL hotspots, suggesting that it results from the PL of the sample background (see figure 3.15).

A recent study of G centre ensembles in microrings [111] indicates that the dynamics of the excited state of the G centres is dominated by non-radiative processes. This result explains the small difference in the G centre excited state lifetime measured in this sample and in a previous study [18] ($\approx$ 5.9 ns). Additional experiments will be needed to further elucidate the recombination dynamics of the G centre in silicon and identify its intrinsic channels.

#### Quantum efficiency of single G centres

With this lifetime, we can now estimate the quantum efficiency of the G centre using the same method as in the previous chapter. However, we have to take into account the new values of (i) the saturated detection rate of 6.3 kc/s, (ii) the new detector efficiency of 80 % as well as (iii) the maximum extraction efficiency of 5 % calculated by our collaborators from CEA Grenoble for a 60 nm SOI. With these new values, the lower bound of the quantum efficiency of the G centre is estimated around 0.2 %, obtained from the equation $\eta_{QE} \geq \tau \cdot I_{sat}/\eta^{max}$. In a recent collaborative work with Baptiste Lefaucher and Jean-Michel Gérard from the CEA Grenoble, ensembles of G centres were incorporated inside SOI microrings producing a five-fold enhancement of the ZPL intensity by the Purcell effect [111]. However, parasitic defects produced besides G centres limit this enhancement [111] and further studies will be needed to decrease the density of the parasitic defects.

To extend our analysis of this defect, the photon polarization of single G centres will be investigated in the following section.

### 3.3.2 Defect reorientation inferred from the polarization diagram

#### Polarisation-resolved PL measurements

Reaching the single emitter regime enables the analysis of the polarization of the single photons emitted by G defects. In figures 3.16(a) and (b) are displayed the two typical emission polarization diagrams of single G centres using the same recording method as in chapter 2. There is one signature indicating deviation from linearly polarized photons.

*Polar emission diagrams visibility*:

The visibility ($V = (I_{max} - I_{min})/I_{max}$) measured on the single G centres in figures 3.16(a) and (b) are $\approx$ 64 % and $\approx$ 67 %, respectively. An analysis over 40 G centres was performed by fitting the emission diagram with equation (2.14). From this fit, a histogram of the visibility is obtained in figure 3.16(c). The visibility values range from 42(1) % to 72(1) %, with an average value of 62(1) %. For a single dipole emitting linearly polarised photons, the associated emission diagram should display a visibility close to 100 %, such as the one shown in chapter 2. Thus

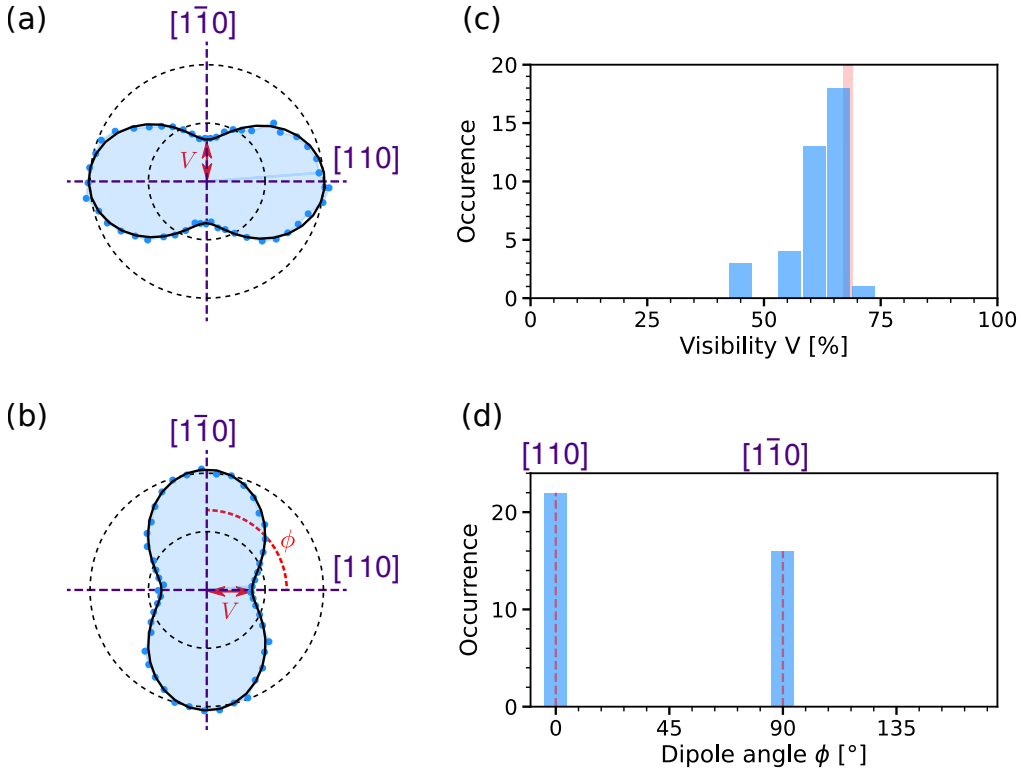


**Figure 3.16:** (a, b) Polarisation-resolved PL measurements of two single G centres displaying horizontal and vertical polarization. The defect PL is corrected from background emission. Data are fitted by equation 2.14 to extract the visibility $V$ and the angle $\phi$ between the main axis of the diagram and the [110] axis indicated in red. (c, d) Histogram of the visibility $V$ and angle $\phi$ obtained from the analysis of 40 single G centres. The red lines correspond to the predictions given by our model plotted in fig. 3.19.

this visibility for the G centres suggests the presence of multiple emission dipoles.

*Dipole orientation*:

The main polarization angle of the emission diagram $\phi$ on the single G centres in figures 3.16(a) and (b) are $\approx 0(1)°$ and $\approx 90(1)°$, respectively. These angles correspond to the [1 1 0] and [1 $\bar{1}$ 0] crystal axis, respectively. A histogram of the main polarization angle for 40 G centres is displayed in figure 3.16(d). We observe that the orientation of the emission polarization diagram is either along [1 1 0] or along [1 $\bar{1}$ 0] crystal axis. The deviation from a 50:50 distribution ratio between the [1 1 0] and the [1 $\bar{1}$ 0] crystal direction is related to the statistical fluctuation resulting from the small number of emitters studied.

The presence of multiple emission dipoles could be linked to the hopping of the interstitial silicon Si(i) between the six equivalent Si positions discussed earlier in section 3.1.2. To investigate the influence of the reorientation of the Si(i) in the emission diagram, a simple model is developed, associating multiple emission dipoles and this reorientation.

### Modeling of the G centre emission diagram

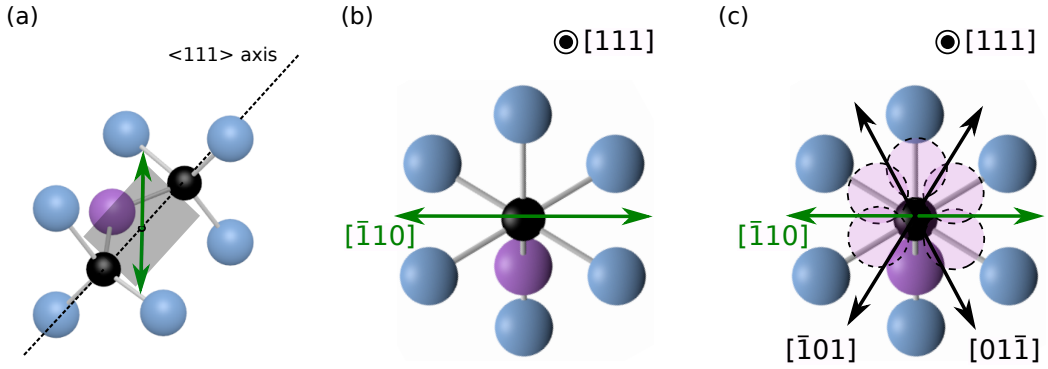


**Figure 3.17:** (a) Schematic of one of the six equivalent interstitial silicon Si(i) atom positions with its associated dipole in double arrowed green lines. The carbon atoms are represented in black, the Si(i) atom is represented in purple and the silicon of the lattice are represented in blue. (b) Schematic of (a) in the plane perpendicular to the <111> axis. (c) Schematic showing the six positions of the Si(i) (dashed purple circles) in the plane perpendicular to the <111> axis for the excited state. The three independent dipoles introduced by our model are represented by double arrowed lines, in green for the [$\bar{1}$10] dipole and in black for the [$\bar{1}$01] and [01$\bar{1}$] dipoles.

Our model consists in associating a single emission dipole to each of the six equivalent positions of the Si(i). The idea is then to sum the dipoles to reproduce the emission diagram.

*Considering one dipole for one Si(i) position*:

Figure 3.17(a) shows the G centre in a frozen state, with the Si(i) fixed in one of the six equivalent positions. Our collaborators Péter Udvarhelyi and Adam Gali from Budapest calculated that the electronic ground state has a A' symmetry and the excited state has A" symmetry. From the electronic transition selection rule, the transition between these two states is allowed for a dipole of A" symmetry (represented by the arrow in figure 3.17(a)), perpendicular to the plane of the two C(s) atoms and the Si(i) atom. In figure 3.17(b), the view is oriented along the <111> axis, where the two C(s) (in black) are superposed, and the Si(i) (in purple) position lead to the dipole along the [$\bar{1}$ 0 1] crystal axis (in green).

Each of the six equivalent positions of the Si(i), corresponding to the vertices of a plane hexagon perpendicular to the <111> axis, are displayed in figure 3.17(c). In this view oriented along the <111> axis, the Si(i) (in purple) can take 5 other equivalent positions represented by the dashed purple circles. Using the same symmetry arguments, the six Si(i) positions are associated with six independent dipoles. Three of the six dipoles are equivalent with three other dipoles in pairs, resulting in three equivalent dipoles along the [$\bar{1}$ 0 1], [$\bar{1}$ 1 0] and [0 1 $\bar{1}$] crystal axis. The [$\bar{1}$ 1 0] dipole (in green) originates from the Si(i) being at the bottom or at the top positions, while the two [$\bar{1}$ 0 1] and [0 1 $\bar{1}$] dipoles (in black) originates from the remaining 4 positions.

*Calculation of the collected intensities for each dipole*:

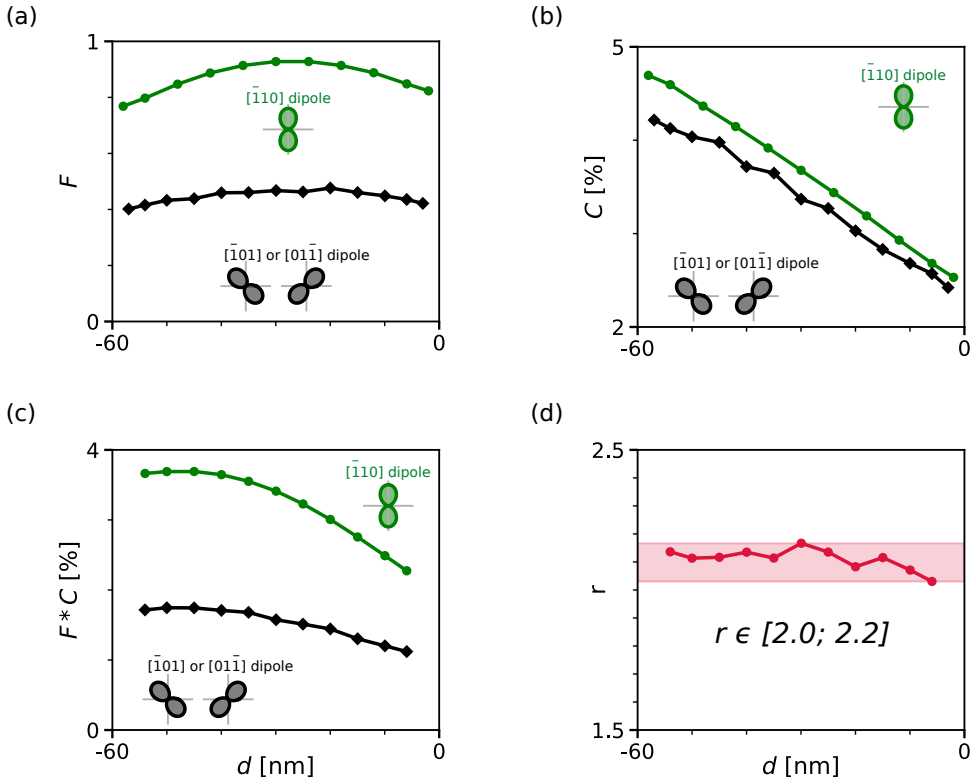


**Figure 3.18:** (a, b, c) Calculations of the exaltation factor F, collection efficiency C, and the effective collection efficiency, which is the product F×C, of the three dipoles used in our model as a function of the dipole depth in the top $^{28}$Si layer. Using the same color code as in figure 3.17, the [$\bar{1}$ 1 0] is displayed in green while the [$\bar{1}$ 0 1] and [0 1 $\bar{1}$] are displayed in black and strictly equivalent. (d) Ratio of the effective collection efficiency of the green and black dipoles r = $(F^{[\bar{1}10]} * C^{[\bar{1}10]})$ / $(F^{[\bar{1}01]} * C^{[\bar{1}01]})$ resulting in a value of r $\epsilon$ [2.0; 2.2] for all depth values.

To determine the effective contribution of the three dipoles, the emission and collection of these dipoles need to be investigated. Using the RSOFT software and the finite-difference time-domain method, our collaborator Jean-Michel Gérard from the CEA Grenoble (PHELIQS) simulated the spontaneous emission of the three dipoles in a 60 nm SOI.

The exaltation factor F is the ratio between the spontaneous emission of a dipole in bulk silicon over the spontaneous emission of a dipole in the studied medium (here 60 nm SOI). Its variations as a function of the depth $d$ in the 60 nm silicon layer are displayed in figure 3.18(a). The exaltation factor F indicates if the dipole emission is inhibited (F $<$ 1) or enhanced (F $>$ 1) by the environment induced by the 60 nm silicon layer. The calculations show that the two [$\bar{1}$ 0 1] and [0 1 $\bar{1}$] dipoles (in black) are strictly equivalent and that their exaltation factor is close to 0.5, showing an inhibition of the emission by a factor close to 2, varying very little with $d$. The exaltation factor for the [$\bar{1}$ 1 0] dipole (in green) varies from 0.78 to 0.92 with $d$. It stays slightly below 1, meaning that its spontaneous emission is less affected by the SOI structure than for the other two dipoles.

Next, the collection efficiency C is the portion of the photon collected by the microscope

objective with a numerical aperture of 0.85. It is also plotted as a function of the dipole position d in the silicon layer in figure 3.18(b). We note that the curves for the three dipoles are similar, which means that the collection efficiency weakly depends on the orientation of the dipole. These collection efficiencies vary linearly with the depth d, going from $\approx$ 4.5 % at the bottom of the silicon layer to 2.5 % at the surface.

To estimate the PL of each dipole, we display in figure 3.18(c) the effective collection efficiency $C_{eff}$ = F * C, and in figure 3.18(d), we plot the parameter r = $C_{eff}^{[\bar{1}10]}$ / $C_{eff}^{[\bar{1}01]}$, which is the ratio between the effective collection efficiency of the [$\bar{1}$ 1 0] and diagonal dipoles. This ratio r vary from 2.0 to 2.2 depending of position of the dipole in the silicon layer. This parameter will fix the weighting coefficient of each dipole in the summation.

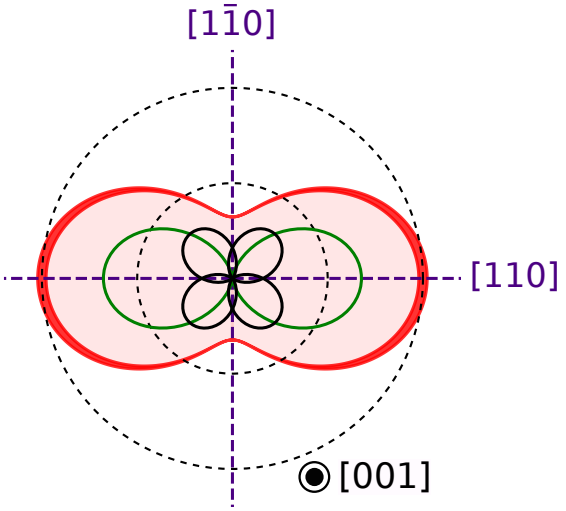


**Figure 3.19:** Projection on the (001) top surface of the sample of the polarization diagrams associated with each of the three dipoles of our model and multiplied by the ratio of the collected intensities. The result of the summation of the three polarization diagrams is represented in red.

*Modeling of the emission diagram*:

Figure 3.19 displays the projection on the top (001) surface of the sample of the polarization diagrams associated with the dipole [$\bar{1}$ 1 0] (in green) and the two dipoles [$\bar{1}$ 0 1] and [0 1 $\bar{1}$] (in black), with the contributions obtained from the ratio r. Using the previously introduced angle $\phi$, the 3 projected dipoles correspond to angles of 0° for [$\bar{1}$ 1 0] (in green), and -45°, +45° for [$\bar{1}$ 0 1] and [0 1 $\bar{1}$] (in black). The summation of the three dipoles on the top (001) surface of the sample is also plotted in red. This modelled emission diagram nicely matches the experimental emission diagram in figure 3.16(a). The model fits the data, and with $r \epsilon$ [2; 2.2], we extract visibility close to the maximum visibility $V \epsilon$ [67; 69] by using the equation 2.14. However, this model does not reproduce all of the emission diagrams measured over 40 emitters, as some of them display lower visibilities. The observed variations in visibility may indicate that the probability of presence per Si(i) site is not equal. This may originate from

a symmetry distortion that could energetically favour certain Si(i) positions. Thus this model could be refined, for example by considering three dipoles non-equivalents, to fit all the data.

Despite these deviations between the data and the model, we evidence the presence of multiple dipoles in the G centre emission. Moreover, these dipoles are associated with the reorientation of the G centre, caused by the interstitial silicon hopping between its six positions.

### 3.3.3 Fine structure in the zero-phonon line

As specified in the first section of this chapter, a fine structure in the ZPL was observed in a strain-free and isotopically purified $^{28}$Si sample in reference [70], with splittings of the order of 10 $\mu$eV (see figure 3.2(a)). In addition, multiple emission lines were observed on the PL spectra of single G centre (see section 3.2.2), motivating a study over its fine structure. We have performed spectrally-resolved measurements of the ZPL but with a spectral resolution of $\approx$ 100 $\mu$eV.

#### Analysis of the ZPL fine structure

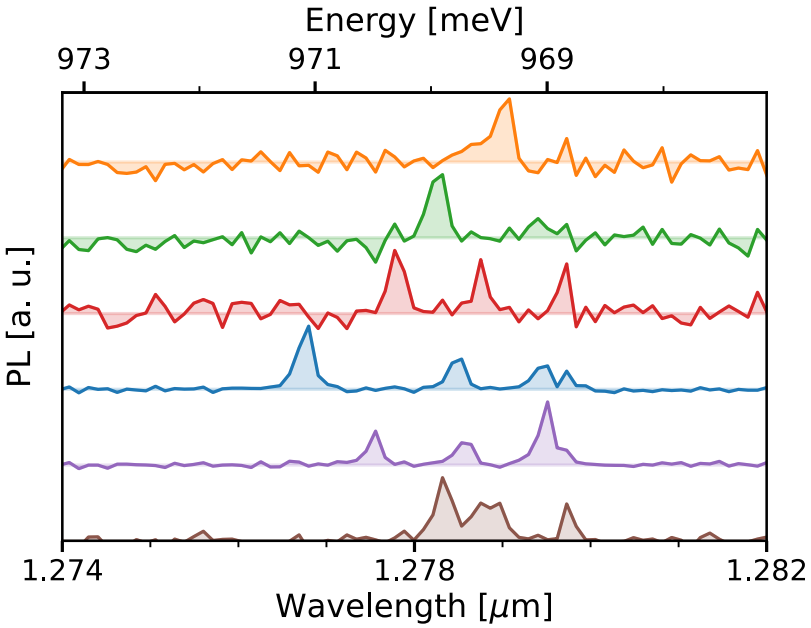


**Figure 3.20:** PL spectra of single G centres zoomed around their ZPL.

To investigate the fine structure of the ZPL in our sample, PL spectra zoomed on the ZPL have been realized on several single G centres located outside of the implanted area. These PL spectra were recorded by using a 600 lines / mm grating, resulting in a spectral resolution of $\approx$ 100 $\mu$eV per pixel ($\approx$ 0.12 nm at the ZPL wavelength). Their PL spectra are displayed in figure 3.20. On almost all these PL spectra, we observe more than one peak, indicating the presence of multiple emission lines whose wavelength varies from defects to defects. We observe splittings of the order of the meV. This ZPL structure is completely different from the one presented in

Chartrand's work [70] since the energy splitting (orders of magnitude lower) and the relative intensity of the lines do not match the quartet (1:2:2:1 intensities, see figure 3.2(a)).

The multiple lines observed on single G centres are attributed to an enhanced splitting of the quartet measured by Chartrand under sample strain. The ZPL splitting under high stress has been well studied in G centre ensembles [84, 91, 99, 112] and the splittings observed here (close to 2 meV) are similar to those measured in ensemble measurements under an applied stress of $\approx$ 150 MPa (with an uniaxial compression along the [100] direction) [84, 91]. In addition, the ZPL splitting of single G centres measured in the implanted areas were showing a slightly lower splitting. The G centres in the implanted areas are optimized to be created at the centre of the top Si layer. Thus, the splitting may be caused by strain induced by the close interfaces (the $Si/SiO_2$ interface and the surface at less than 60 nm).

The exact number of lines are hard to estimate due to the limit in the resolution of our spectrometer. This issue could be solved by future PLE measurements, as this would allow a better resolution of the ZPL splitting.

Next, we further investigate the ZPL splitting by resolving the emission polarization.

**Evolution of the ZPL with polarization**

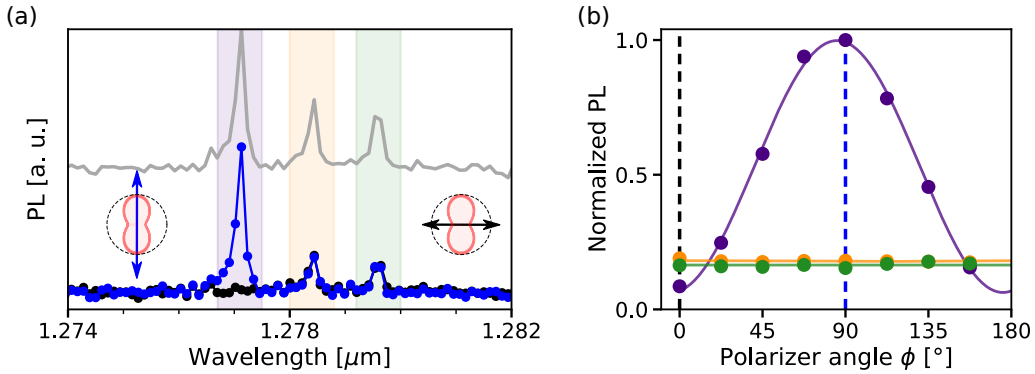


**Figure 3.21:** (a) PL spectrum zoomed around the ZPL of a single G centre for two different emission polarizations. The PL spectrum in blue is analysed with a vertical polarization (90°) corresponding to the main dipole axis of the defect. The PL spectrum in black is filtered with a horizontal polarization (0°). The emission diagram of this single G centre is displayed in red in inset with the polarization of the PL represented by an arrow for both PL spectra. The PL spectrum without polarization is displayed in grey. (b) For the same single G centre, evolution of PL intensity integrated over a given wavelength range as a function of the polarizer angle $\phi$. The chosen wavelength ranges of integration correspond to the three windows of the PL spectrum in (a) indicated by the columns in purple, orange and green, with matching color code.

To observe whether the PL spectrum varies with polarization, we use the same set-up as for measuring emission polarisation diagrams. In figure 3.21(a), two PL spectra are recorded on a single G centre for horizontal and vertical polarization. In addition, the unfiltered PL spectrum (in grey in figure 3.21(a)) is displayed for comparison. For a vertical polarization, there are 3

lines, identical to the ones in the unpolarized PL spectrum. The relative intensities of the lines however are different. The two low energy lines centered at 1278.5 nm and 1279.6 nm are weaker than those in the unfiltered PL spectrum. When the polarizer is placed perpendicular to the main axis of the polarization diagram of this defect (in red in figure 3.21(a)), the left emission line vanishes, while the other two lines seem to remain unchanged in comparison to the vertical polarization PL spectrum.

In figure 3.21(b) is plotted the evolution of the integrated PL intensity of each line as a function of the polarizer angle. We observe a significant variation for the high energy line and almost no variations for the other two. The variations in intensity of the high energy line gives a visibility close to unity (V = 92(1) %). This suggests that this line originates from the $[\bar{1}10]$ emission dipole. However, the other two lines does not appear to be associated with a single linearly-polarized emission dipole, or to the $[\bar{1}01]$ and $[01\bar{1}]$ dipoles.

Nevertheless, the variation of the high energy line with the polarization angle indicates that this emission line is related to a single dipole linearly polarized (in particular to the $[\bar{1}10]$ emission dipole) and that spectral filtering could provide information on the position of the Si(i) atom through the selection of emission dipoles. However, the complete understanding of all the split lines of the ZPL and their association with all of the dipoles generated by the hopping Si(i) atoms between the 6 quasi-equivalent positions require additional works. Other parameters of this hopping Si(i) atom, such as the tunneling time between positions or the effect of temperature, are still unknown and need to be explored.

## 3.4 Conclusion

Isolation of G centres at the single scale was achieved in a sample fabricated by a cross-implantation method using carbon and proton in a silicon-on-insulator sample. By gradually decreasing the fluences of the carbon ions and the protons, this reproducible fabrication method allowed the creation of ensembles down to single emitters. The single G centres have enabled the study of the defect photophysics at single scale, revealing photostable defects, with a short radiative lifetime of 4.5 ns and a low quantum efficiency of 0.2 %. The study of the emission diagrams of single emitters evidenced the presence of multiple emission dipoles, linked to the interstitial silicon hopping between 6 equivalent positions, observed via the study of the ZPL fine structure by spectroscopic and polarization measurements. This unusual hopping is interesting from a fundamental physics perspective however, generation of indistinguishable photons with this defect seems to be compromised by the splitting in the ZPL, but might still be possible through spectral filtering or by controlling the emission lines via strain. However, the low quantum efficiency of the defect is not ideal for quantum communication applications.

In the next chapter, the demonstration of the isolation at single scale of another defect will be presented, the W centre. This single defect presents a linearly polarized emission, and may be better suited for quantum communication applications.

Chapter 4

# Creation and detection of single W centres

Contents


**4.1 The W centre in Silicon . . . . . 76**
4.1.1 Optical properties of ensembles of W centres . . . . . 76
4.1.2 Microscopic structure . . . . . 77
4.1.3 Electronic level structure . . . . . 79
**4.2 Creation of single W centre by ion implantation . . . . . 80**
4.2.1 Investigation of the implanted areas . . . . . 80
4.2.2 Detection of single W centres outside the implanted areas . . . . . 82
**4.3 Study of W centres at single defect scale . . . . . 84**
4.3.1 Investigation of the ZPL of single W centres . . . . . 84
4.3.2 Orientation of the emission dipole of W centres . . . . . 87
4.3.3 Photostability . . . . . 88
**4.4 Photodynamics of individual W centres . . . . . 89**
4.4.1 Excited state lifetime . . . . . 89
4.4.2 Evolution of the $g^2(\tau)$ function with laser power . . . . . 90
4.4.3 Saturation curves . . . . . 92
**4.5 Conclusion . . . . . 95**


## Introduction

Intrinsic defects in silicon, consisting of vacancies or interstitials, are often present in silicon-based components and are therefore well-studied defects [86]. During nanofabrication, their unintentional creation can limit the performances of silicon nanoelectronic devices [63]. In addition, in environments subject to strong radiations [113] such as in particle physics experiments [64], intrinsic defects are blamed as being the cause of degradation of silicon-based components. Concerning the development of advanced large-scale quantum photonic devices, control of the quantum properties of individual fluorescent defects in silicon has been so far focused on extrinsic defects based on impurities embedded in the silicon lattice. Thus, intrinsic defects in silicon, in particular optically active defects such as the W centre, could be of interest for these applications.

The W centre is a common fluorescent defect in silicon with a ZPL emission at 1218 nm (1.018 eV). It is made of self interstitial atoms [62] and is a well studied defect [86]. This intrinsic defect can be created by silicon implantation [65], neutron irradiation [114] or following laser

annealing [115]. It has been also created in isotopically purified $^{28}$Si, thus drastically reducing its optical linewidth [70]. Although the presence of the W centre appears to be detrimental in microelectronics [63, 64], there has recently been a renewed interest for Si based classical photonics, where it has been used as an active medium in LEDs [116, 117] and optical resonators [118]. For quantum applications, its optical properties such as an emission in the near infrared close to the telecom O-band, and an intense ZPL with a Debye-Waller of around 40 %, are promising characteristics to potentially develop efficient emission of indistinguishable near infrared photons.

We first introduce the W centre by looking at its optical properties as well as its microscopic structure. Then creation and isolation of single W centres will be demonstrated in an ultra pure silicon sample, followed by its study at the single scale. To finish, the photodynamics of single W centres will be investigated, as well as the evolution of the PL intensity with optical power.

***In this chapter, the two InGaAs/InP avalanche photodiodes (ID Quantique ID230) working in the single-photon regime, with a quantum efficiency of 10 % at 1.22 $\mu$m are used for all measurements.***

## 4.1 The W centre in Silicon

In the first section we will describe the optical properties of the W centre, then in the second section its microscopic structure will be discussed, and finally in the last section its electronic level structure will be explained.

### 4.1.1 Optical properties of ensembles of W centres

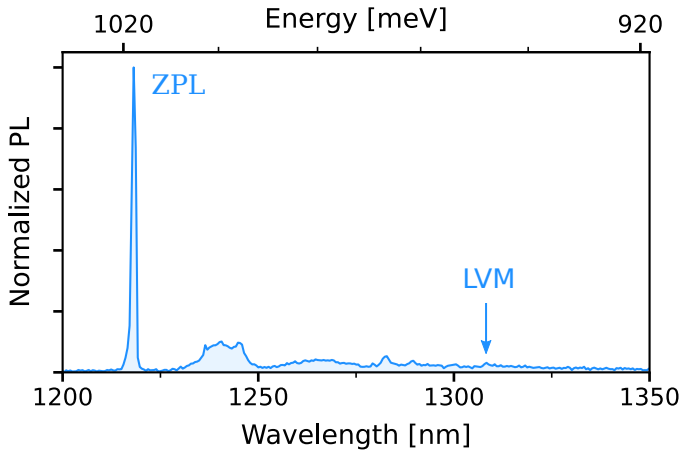


**Figure 4.1:** PL spectrum of an ensemble of W centres in silicon. The PL spectrum displays an intense ZPL at 1218 nm, as well as an emission line associated with a local vibrational mode (LVM) at 1308 nm.

The emission of the W centre in silicon is characterized by a bright ZPL at 1218 nm (1.018 eV) with a DW factor of $\approx$ 40 % [119], accompanied by a broad structured PSB that includes

an emission line at 1308 nm (948 meV), associated with a LVM at 70 meV, as displayed in figure 4.1. This DW value is higher than any of the point defects studied in the previous chapters and, as mentioned above, holds promise for efficient single photon source applications. Time-resolved PL measurements on ensembles of W centres in a commercial SOI sample implanted with Si ions at 80 keV with a fluence of $5\times10^{13}$ cm$^{-2}$, determined an excited state lifetime of 34.5(5) ns [65], more than 5 times longer than the ES lifetime of G centres (5.9 ns). A recent measurement in an isotopically purified $^{28}$Si sample gives a value of 2.0(1) $\mu$eV for the FWHM of the ZPL in ensembles of W centres. With an excited state lifetime of 34.5 ns, the associated Fourier-transform limited broadening is equal to 0.02 $\mu$eV, two order of magnitude lower than the one measured, indicating the presence of inhomogeneous broadening. The W centres are assumed to exist near the most heavily damaged regions, which may induces a large inhomogeneous broadening, and their linewidth in $^{nat}$Si decreases with increasing annealing temperature [113]. A control over the creation of the defect could therefore reduce this inhomogeneous linewidth in the prospect of indistinguishable single photon source applications. The ZPL emission stems from a transition between spin singlet states [70, 119] like the G centre. However, in contrast to the G centre, no ODMR has been detected.

### 4.1.2 Microscopic structure

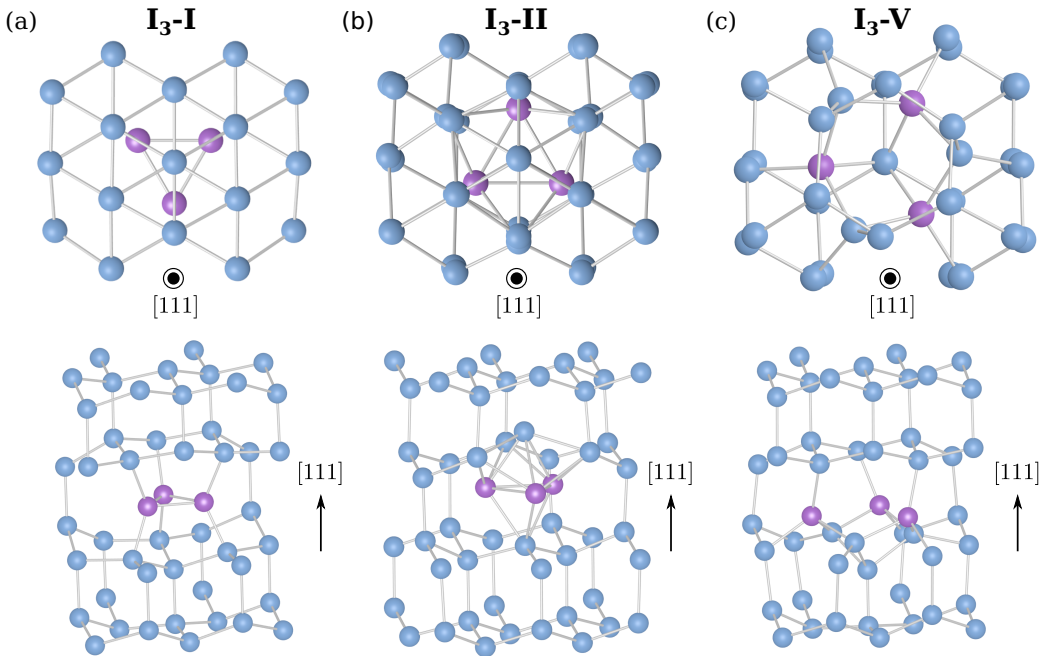


**Figure 4.2:** Tri-interstitial potential candidates for the microscopic structure of the W-center in silicon. (a) $I_3$-I defect, (b) $I_3$-II defect, and (c) $I_3$-V defect. (Top) View showcasing the defect structure. (Bottom) View perpendicular to the [111] direction showcasing the symmetry. The blue spheres are silicon atoms and the 3 purple spheres are the interstitial silicon atoms constituting the defect.

Multiple microscopic configurations have been proposed as the origin of the W centre emis-

sion, such as di- [62], tri- and tetra-interstitial [62, 120] microscopic structures. In 1999, the tri-interstial ($I_3$) defect in its neutral state was determined to be the most stable structure using ab initio tight-binding molecular-dynamics simulations [121] and first principles local-density-functional theory [62]. At the beginning of my PhD, the microscopic structure of the W centre was still debated. The $I_3$-I, which was the first proposed configuration, corresponds to a triangular arrangement with the three Si atoms positioned at the center of three adjacent $\langle 111 \rangle$ bonds, forming a three-atom ring (see figure 4.2(a)). This $I_3$ defect possesses a vibrational mode at 74 meV, close to the LVM at 70.0 meV, and possesses a $C_{3v}$ symmetry, consistent with uniaxial stress measurements that revealed a trigonal symmetry [119]. Afterwards, the $I_3$-II defect, consisting of a compact tetrahedral shape, has been found with a formation energy lower by $\approx$ 1 eV [67, 122]. However, this defect did not present any LVM and possesses the wrong symmetry ($T_d$) [123]. The last configuration $I_3$-V is a more extended form of the $I_3$-I structure, obtained by combining tight-binding molecular dynamics and ab initio calculations [124]. It displays a $C_{3v}$ symmetry and the correct LVM energies, with an energy formation in-between the other two configurations obtained via local density functional calculations [123] and ab initio simulations [67]. However, the presence of energy levels inside the bandgap to enable its optical activity was still under debate [67, 123].

Theoretical work using density functional theory (DFT) computations was carried out by our collaborators Péter Udvarhelyi and Adam Gali at the Wigner Research Centre for Physics in Budapest (Hungary) during my PhD thesis. Their simulations brought new elements that evidence the $I_3$-V structure as the best candidate for the microscopic structure of this defect [125]. The formation energies of the three configurations were determined by DFT calculations using the Heyd–Scuseria–Ernzerhof functional (HSE06) and gives 8.17, 7.69 and 7.52 eV for the neutral $I_3$-I, $I_3$-II and $I_3$-V configurations, respectively. This reveals that the $I_3$-V configuration is the most stable one, contrary to what was reported before. The previous calculations used methods (local density approximation and Perdew-Burk-Ernzerhof functional) that tend to delocalize the wavefunction, thus favoring the more compact structure, in contrast with the HSE06 functional. Bonding properties described with the HSE06 functional reveals in plane bond lengths between the three Si atoms to be 2.465 Å for the $I_3$-II configuration and 2.315 and 2.242 Å for the $I_3$-V configuration. The out-of-plane bond lengths are 2.457 and 2.296 Å for the $I_3$-II and $I_3$-V configurations, respectively, confirming that the $I_3$-V configuration is the most stable. Vibrational calculations show that the $I_3$-II configuration does not possesses LVM in agreement with previous studies. LVMs are found at 69.9, 73.9 and 74.2 meV for the $I_3$-I configurations, while LVMs for $I_3$-V at 63.8, 65.9 and 71.6 meV. Both configurations have LVMs with an energy close to the 70 meV of the W centre, so no distinction can be made on the basis of LVM energy alone.

The electronic structure of the $I_3$-I and $I_3$-V atomic configurations was calculated, allowing to identify the most likely microscopic structure to account for the PL of the W centre. This will be discussed in the next section.

### 4.1.3 Electronic level structure

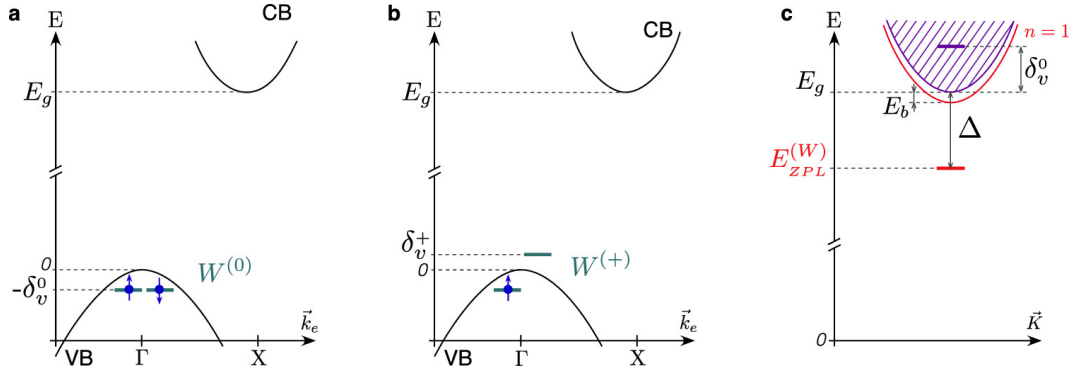


**Figure 4.3:** Schematics of the energy level diagrams of the $I_3$-V configuration of the W-center. In the single-particle representation, energy diagrams of (a) the GS of the neutral form of the defect and (b) after its ionization. VB: valence band; CB: conduction band; $\vec{k_e}$ is the electron wavevector. (c) Two-particle representation of the energy levels. The continuum of free electron–hole pairs above the electronic bandgap energy $E_g$ is represented in purple. The red parabola represents the GS of the bulk excitons, whose energy minimum is lower from $E_g$ by the exciton binding energy $E_b$. The energy splitting Δ between the W centre ZPL energy $E_{ZPL}$(W) and the silicon bandgap includes the energy $\delta_v^+$ and the binding energy of the exciton localized on the defect. $\vec{K}$: wavevector of the electron–hole pair center-of-mass.

HSE06 DFT calculations were performed on the two $I_3$-I and $I_3$-V configurations by our collaborators Péter Udvarhelyi and Adam Gali. In their neutral singlet ground state, no strongly localized in-gap defects levels emerged. While the absence of electronic energy levels within the silicon gap may indicate at first sight that no optical emission is possible with these configurations, important Coulomb correlations induce an optical transition inside the gap. For the $I_3$-V configuration, in the ground state of the neutral form, there is a resonant state localized at the defect position in real space 73 meV below the valence band maximum (VBM), as displayed in the single-particle representation in figure 4.3(a). After ionization (using the Freysoldt–Neugebauer–Van de Walle charge correction), the unoccupied defect level of $a$ type emerges inside the bandgap, 55 meV above the VBM, as shown in figure 4.3(b). Then under photo-excitation, an electron is promoted to a level ($a$ type) close to the CB, leading to the creation of an electron-hole pair with the hole localized inside the bandgap. The electron–hole interaction further pushes the transition energy inside the bandgap, as showed in the figure 4.3(c) in the two-particle representation. Thus the W centre ZPL appears to originate from an excitonic recombination between a hole localized at the defect and an electron trapped by Coulomb interaction [125]. The symmetry of the ES for the $I_3$-V configuration has an A character, and the GS of the neutral defect is a closed-shell A state. Thus, the optical transition dipole moment of the $I_3$-V defect belongs to the A symmetry and is predicted to lie in the <111> direction. Furthermore, the ZPL energy was estimated at a value close to the experimental one of 1.018 eV, using the self-consistent field method for two different functionals.

For the $I_3$-I configuration, a degenerate $e$ level and a single $a$ level below the VBM at 142

and 201 meV, respectively, were obtained. These levels are unable to support a stable positive charge state and therefore cannot result in a hole confined at the defect position. These results therefore exclude the $I_3$-I configuration as the structure of the W centre. Thus, based on the latest DFT calculations, the $I_3$-V configuration is the most promising microscopic structure for explaining the W centre luminescence in silicon.

After this introduction about the W centre in silicon, we will now look at the optical experiments on single W centres performed during my thesis.

## 4.2 Creation of single W centre by ion implantation

As for the G centre, the isolation of defects at single scale allows a more in-depth study of the intrinsic optical properties, since there is no averaging effect anymore compared to ensemble measurements. To study the creation and perform the isolation of W centres, an ultra pure SOI sample was locally implanted with $^{28}$Si ions with varying fluences to enable a gradual transition from dense ensembles of W centres to diluted ones. In the first section, we investigate the PL emission of ensembles of W centres in the implanted areas by performing optical scans and PL spectra. Then, in the second section, single W centres created around the locally implanted areas will be examined via spectroscopic studies and intensity-correlation measurements.

### 4.2.1 Investigation of the implanted areas

We start by looking at the implanted area to study the creation of W centres as a function of the implantation parameters. First we introduce the sample used for this study, then we investigate the implanted area via optical scans and spectroscopic analysis.

#### $^{28}$Si-implanted SOI sample

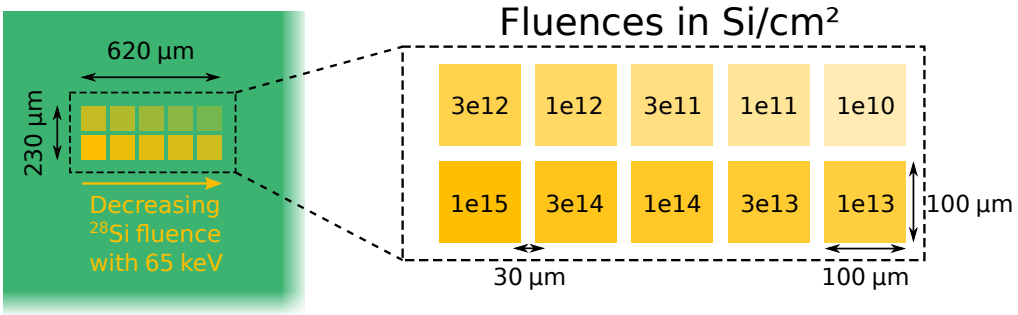


**Figure 4.4:** Schematic top view of the $^{28}$SOI sample displaying the implantation map. A square pattern is repeated to implant $^{28}$Si while decreasing the fluences.

The sample studied for the investigation of the W centres comes from the same pristine wafer as the one studied in the previous chapter for the G centres. Thus, the sample control experiments (see previous chapter) carried out on the virgin sample (#0, see table 3.1) and the

sample (#0.5) that underwent only a flash annealing are relevant here. This allows us to know that the sample prior to the implantation step does not contain any W centre. First, the sample underwent a flash annealing at 1000°C during 20 s under $N_2$ atmosphere. Then, to create the point defects, $^{28}$Si ions have been locally implanted in squares (with a size of 100 × 100 $\mu m^2$), with an energy of 65 keV and with fluences ranging from $1\times10^{10}$ to $1\times10^{15}$ $cm^{-2}$. This energy was chosen from SRIM simulations, maximising the creation of vacancies in the upper Si layer by having the Si ions stop after the $Si/SiO_2$ interface. These patterns were obtained by positioning a 30 $\mu$m thick mica mask with a square aperture of 100 × 100 $\mu m^2$ in front of the SOI sample at a distance of 4.5 mm. The mask was moved for the different fluences, with a gap between the squares of 30 $\mu$m, resulting in an implanted area of 230 $\mu$m by 620 $\mu$m as indicated in figure 4.4.

**PL map**

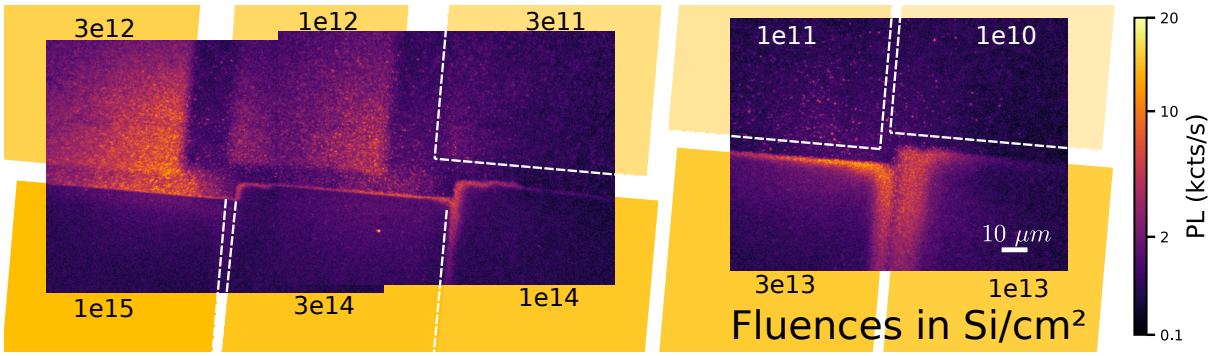


**Figure 4.5:** Reconstruction of the PL map of the entire implanted area using multiple optical scans of 160 $\mu$m by 120 $\mu$m. Scale bar = 10 $\mu$m. The PL intensity is plotted using a logarithmic scale for better contrast. The white lines are guides to the eyes to display the implantation squares. Fluences are indicated at the top or bottom of each squares.

In figure 4.5, several optical scans are concatenated to display the implanted area, like for the G centre implanted area (see chapter 3). In our experimental set-up, optical scan can display PL variations on a scale of about 30 $\mu$m because the sample PL is less collected on the borders than on the center of the scans. The variations in PL observed inside each 160x120 $\mu m^2$ scanned area are the consequence of this effect.

We observe that there is a significant variation in PL intensity between the different implanted squares. There is a maximum PL intensity when the silicon ion fluence reaches $3\times10^{12}$ $cm^{-2}$. For high fluences, corresponding to the implanted squares with fluences from $1\times10^{15}$ to $1\times10^{13}$ ions/$cm^2$, we observe PL intensity on the sides but not inside the squares. A higher PL intensity is observed on the sides when the implantation fluence decreases. This shows the harmful effect of implanting silicon ions at high fluences to create W centres. Then for the lower fluences (from $1\times10^{12}$ to $1\times10^{10}$ ions/$cm^2$), the PL intensity decreases due to the creation of more and more dilute ensembles of fluorescent defects with the lowering of the fluence. In these areas, the intensity of the PL signal is no longer spatially uniform with the appearance of bright

spots that are more distant as the fluence is low.

**PL spectra**

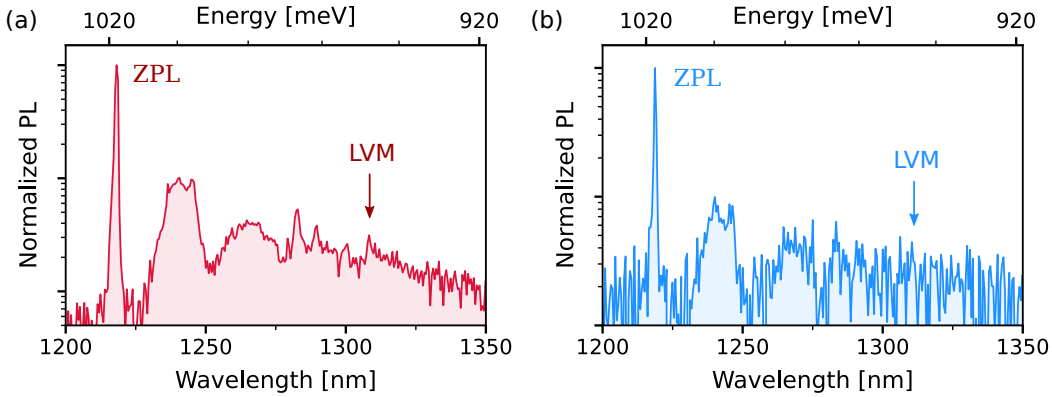


**Figure 4.6:** (a) PL spectrum recorded on a position inside the implanted area with fluence of $3\times10^{12}$ $^{28}$Si/cm$^2$, revealing the formation of an ensemble of W centres. (b) PL spectrum recorded on a diluted ensemble corresponding the implanted area with fluence of $1\times10^{10}$ $^{28}$Si/cm$^2$. The arrows indicate the position of the LVM at 70 meV [66, 119]. In (b), the LVM is hidden in the noise, and a longer acquisition time should have been used to differentiate it from noise.

Next, PL spectra in the different implanted areas are acquired. The spectrum of the PL emitted in the square with maximum PL (fluence of $3\times10^{12}$ cm$^{-2}$) is displayed on figure 4.6(a) on a logarithmic scale. This emission is typical of the W centre in silicon, with the same characteristics as in figure 4.1 (i.e. a ZPL at 1218 nm and a LVM at 1308 nm) [66, 119]. Thus the present implantation method is successful to create W centre ensembles for a fluence of $3\times10^{12}$ $^{28}$Si/cm$^2$ and an energy of 65 keV. The PL on the side of the heavily implanted squares ($10^{13}$ to $10^{15}$ ions/cm$^2$) also comes from W centres. PL spectra were further taken on isolated spots in the diluted ensembles, and their PL also comes from the emission of W centres as shown in figure 4.6(b).

At the periphery of the implanted areas, the concentration of defects is low. As for the G centres, this method of ion implantation creates W centres in and outside the implanted areas. These regions outside the implanted areas have a similar concentration of defects to the one implanted at $10^{10}$ $^{28}$Si/cm$^2$ where the W centre density is of order 0.01 $\mu$m$^{-2}$. Thus we concentrate our study on the W centres created outside the implanted area. These defects are investigated in the next section.

### 4.2.2 Detection of single W centres outside the implanted areas

Few hundreds of $\mu$m away from the implanted areas, optical scans taken at a temperature of T=10 K reveal isolated PL spots over a dim background, as shown in figure 4.7(b). The PL spectrum of these isolated spots, displayed in figure 4.7(c), is similar to the PL spectrum taken on the ensemble of W centres (see figure 4.1 and 4.6). In view of their similarities, the

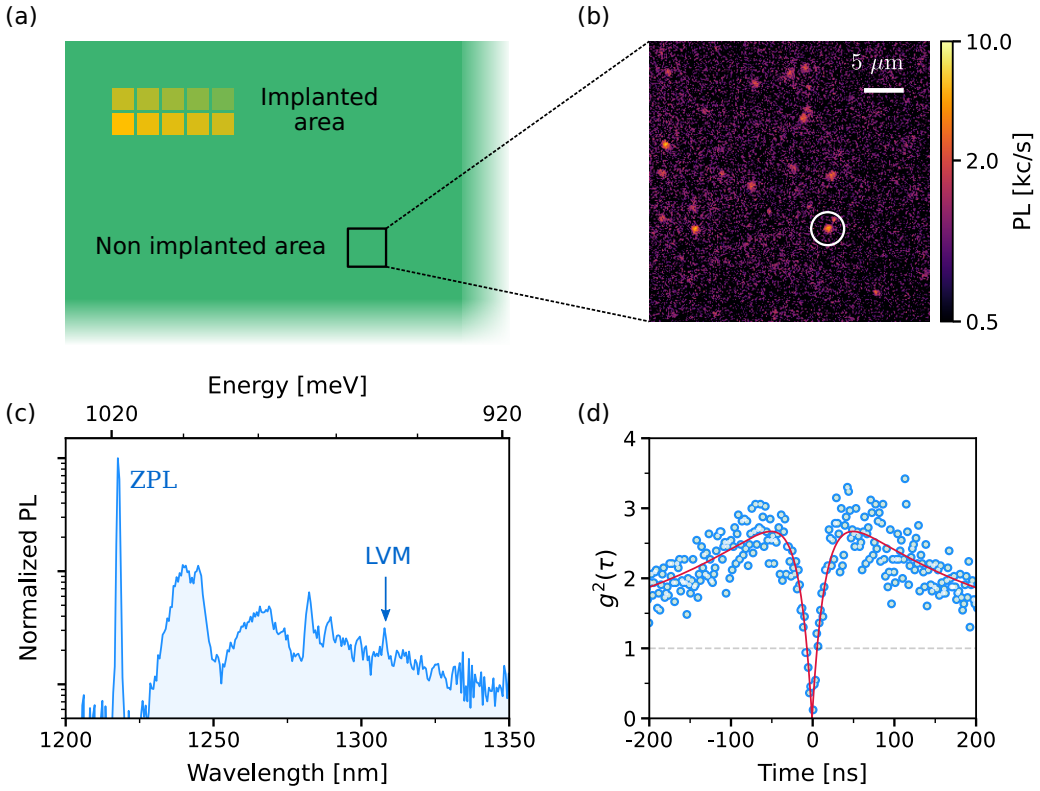


**Figure 4.7:** Isolation of single W centres in silicon. (a) Top view of the $^{28}$SOI sample displaying the implantation map, as well as an area a few hundreds of $\mu$m away from the implanted area. (b) PL raster scan recorded outside the implanted region. (c) PL spectrum from the bright spot circled in panel (b). (d) Second-order autocorrelation function $g^{(2)}(\tau)$ measured at this position. The antibunching effect at zero delay reaches the value $g^{(2)}(0) = 0.12(5)$, without any background or noise correction. The red curve is data fitting with the three-level model of eq. (2.9). All measurements are acquired at 10 K.

isolated spots are attributed to one or several W centres. An estimation of the Debye–Waller factor is performed and gives a value of ≈40 %, very close to the one determined in ensemble measurements [119].

Intensity-correlation measurements, using the HBT set-up presented in chapter 2, were performed on these isolated spots. A typical autocorrelation function is displayed in figure 4.7(d), featuring a strong antibunching at zero delay of $g^{(2)}(0) = 0.12(5)$. This $g^{(2)}(0)$ is well below the single photon emission threshold of 0.5 [89], indicating the presence of a single emitter, here an individual W centre. Moreover, this low value is not corrected from any background counts or noise, and results from a very good SNR of 15. In addition, a bunching effect is observed in figure 4.7(d), indicating that a non-radiative path through a metastable level is involved in the relaxation process [89] (see chapter 2). This bunching will be analysed in more detail in section 4.4.2. Such information is inaccessible through ensemble measurements, which shows the interest of isolating single point defects to study them.

After the successful isolation of single W centres, we will explore their optical properties in the next section.

## 4.3 Study of W centres at single defect scale

The isolation at single scale of W centres allows us to explore their optical properties without the averaging effect of ensembles. The ZPL energy of single W centres will first be investigated, followed by their temperature dependence. The study of the polarization dependence of the single W centres emission will reveal the nature and the orientation of the defect dipoles. Finally, the photostability will be examined.

### 4.3.1 Investigation of the ZPL of single W centres

For quantum communications, photon energy variations from one defect to another prevent their implementation in a quantum network. Indeed, to allow two-photon quantum interference from distant defects, their photon emission must satisfy two criteria. (i) The emitters must emit photons at the same average energy and (ii) each emitter must emit indistinguishable photons on long time scale (i.e. have a Fourier-transformed limited linewidth). As we saw in the previous chapters 2 and 3, for solid state emitters, the average emission is usually at different frequencies between emitters. Thus the investigation of the ZPL variations of one W centre to another is performed.

#### Statistical study of the ZPL energy

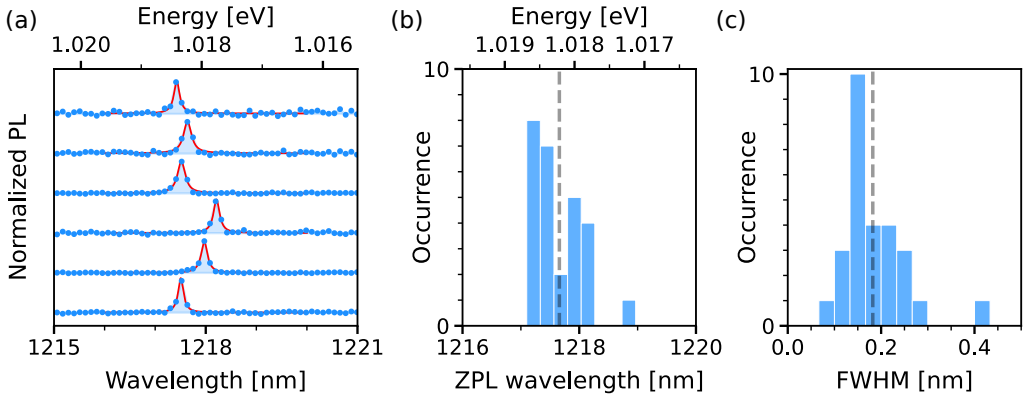


**Figure 4.8:** Statistical analysis of the ZPL of single W centres at T=30 K. (a) ZPL spectra recorded on individual W defects, data in blue are normalized by the ZPL maximum and are shifted in intensity for a better visualisation. The red solid lines are data fitting with a Lorentzian function (eq. 4.1) to extract the ZPL energy. The FWHM is limited by the spectrometer resolution to ≈0.10 meV. Distribution of the ZPL energy (b) and of the full width at half maximum (FWHM) (c) for a set of 27 single W centres. The dashed vertical line indicates the mean value on both histograms.

PL spectra zoomed on the ZPL were recorded over 27 single W centres. Figure 4.8(a)

displays 6 typical PL spectra of single W centres where we observe variations in the central wavelength and linewidth of the ZPL. To quantify these variations, data are fitted with the following Lorentzian function:

$$f(\lambda) = A \times \left[ \frac{(\frac{\Gamma}{2})^2}{(\lambda - \lambda_0)^2 + (\frac{\Gamma}{2})^2} \right] \tag{4.1}$$

with $A$ is the amplitude of the Lorentzian function, $\Gamma$ the full width at half maximum (FWHM) of the Lorentzian function and $\lambda_0$ the value of the peak of the Lorentzian function. Figure 4.8(b) displays the histogram of the ZPL wavelength $\lambda_0$, and figure 4.8(c) the histogram of the ZPL width $\Gamma$.

For the ZPL wavelength, a mean value of $\lambda_0 \approx 1217.7(1)$ nm is extracted (corresponding to a ZPL energy of 1018.2(1) meV). This value is equal within the error bars to the 1018.24 meV energy reported on ensembles in isotopically purified $^{28}$Si and acquired with a Fourier-transform infrared (FTIR) spectrometer [70]. Of the W centres studied, 95 % have a ZPL with an energy between 1017.7 to 1018.7 meV. These fluctuations are about 20 and 6 times smaller than those observed in the 220 nm thick silicon layer for the unidentified single color centers G* and SD-2, respectively (see chapter 2, section 2.3.1). The variations in our sample are attributed to different strain and electrostatic environments experienced by each emitter. For the FWHM, a mean value of 0.18(4) nm is obtained (corresponding to 150(40) $\mu$eV), partly limited by the resolution limit of our spectrometer, which is close to 100 $\mu$eV.

Next, we analyse the temperature dependence of the ZPL.

**Temperature dependence of the ZPL**

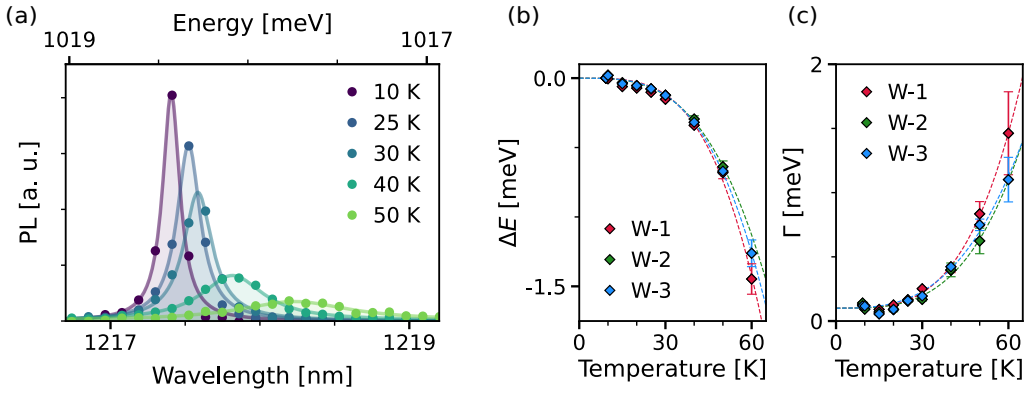


**Figure 4.9:** Evolution with temperature of the ZPL of single W centres. (a) ZPL spectra recorded on a single W centre at different temperatures. The data are represented with round markers and are fitted with a Lorentzian function (solid lines). (b) Evolution versus temperature of the ZPL energy shift $\Delta$E with respect to the ZPL energy at 8 K for three single W defects. (c) Evolution with temperature of the FWHM $\Gamma$ for the same defects. Error bars represent the standard error from data fitting results. Dashed lines in (b, c) are data fitting results with a polynomial function.

For indistinguishable single photon source applications, the study of the broadening with temperature can indicate the most suitable operating temperature regime for the photon source. Thus the temperature dependence of the ZPL shift and broadening is carried out. The evolution of the ZPL with temperature is analysed for 3 individual W centres in figure 4.9 where their PL spectra were recorded for different sample temperatures ranging from 10 K to 60 K. Figure 4.9(a) displays the PL spectrum of one single W centre from 10 to 50 K. Two effects are observed when increasing the temperature, a red-shift of the ZPL alongside its broadening. To quantify these two effects, the ZPL are fitted by a Lorentzian function to extract their mean energy and FWHM.

On figure 4.9(b) is plotted the ZPL energy shift $\Delta E$ (shift from the ZPL energy at T = 10 K) with temperature. The evolution of $\Delta E$ with temperature is identical for the 3 individual W centres within the error bars and is also similar to ensembles measurement [119]. $\Delta E$ is fitted with the polynomial formula: $\Delta E(T) = -\alpha T^p$, which is commonly observed for fluorescent defects in semiconductors [126]. This polynomial law matches well the data with the parameters $\alpha$ = 1.3(5), 2.5(2) and 0.6(5)$\times 10^{-6}$ meV/K$^p$ and p = 3.4(1), 3.2(2) and 3.6(2) for W-1, W-2 and W-3, respectively, revealing that the ZPL shift follows a polynomial law of degree close to 3. This behaviour is similar to the one observed on ensembles of G centre in silicon with $\alpha$ = 1.9(2)$\times 10^{-6}$ meV/K$^3$ and p = 3.0(1) [18]. To understand this ZPL shift, we compare it with the band gap of bulk silicon, which decreases with temperature (see figure 1.2(b)) with a shift of -2.5 meV between 0 and 60 K. Thus the ZPL shift observed on the W centres is lower than the silicon bandgap shift, indicating an additional effect. Indeed, the ZPL red-shift for the W centre in silicon originates mainly from the temperature dependence of the electron–phonon interaction [18, 119]. In addition, a negligible part of the ZPL shift comes from the thermal contraction of silicon, being only $+5\times 10^{-3}$ meV between 0 and 50 K for the W line [119]. The fitting results for the ZPL shift with temperature are presented in Table 4.1.

| Center | | W-1 | W-2 | W-3 |
|---|---|---|---|---|
| $\Delta E$ | $\alpha[\times 10^{-9}]$ | $1.3 \pm 0.5$ | $2.5 \pm 0.2$ | $0.6 \pm 0.5$ |
| | p | $3.4 \pm 0.1$ | $3.2 \pm 0.2$ | $3.6 \pm 0.2$ |
| $\Gamma$ | $\alpha'[\times 10^{-9}]$ | $5 \pm 4$ | $1 \pm 2$ | $0.8 \pm 0.4$ |
| | $p'$ | $3.0 \pm 0.2$ | $3.4 \pm 0.4$ | $3.5 \pm 0.1$ |

**Table 4.1:** Fitting results for the ZPL thermal shift $\Delta E$ and broadening $\Gamma$ of individual W centres, whose data are presented in figures 4.9(b) and 4.9(c). The uncertainties correspond to one standard deviation.

The variations of the FWHM of the ZPL ($\Gamma$) with temperature are displayed in figure 4.9(c). In our case, the parameter $\Gamma_0$ is limited by the spectral resolution of our spectrometer (0.10 meV). Above this value, we are observing an increase of the FWHM, corresponding to a broadening of the ZPL for temperatures above 20 K, following a polynomial law. The 3 single W centres analysed display identical behaviour within the error bars, and follow the same behaviour

as ensembles measurements [119]. The thermal evolution of Γ is fitted with the expression: $\Gamma(T) = \Gamma_0 + \alpha' \cdot T^{p'}$, where $\Gamma_0$ is the zero-temperature FWHM. A polynomial law matches well the data with the parameters $\alpha' = 5(4)$, 1(2) and $0.8(4)\times10^{-6}$ meV/K$^p$ and p$' = 3.0(2)$, 3.4(4) and 3.5(1) for W-1, W-2 and W-3, respectively. This increase in the ZPL width is due to phonon-assisted broadening processes [18, 119]. Thus, for single-photon applications, it is desirable to work at low temperature for the W centre. Additional measurements, such as PL excitation (PLE) measurements, which could allow to measure optical linewidths narrower than the spectral resolution of our spectrometer, are required at lower temperature to estimate the temperature regime that narrow the emission line to a minimum.

### 4.3.2 Orientation of the emission dipole of W centres

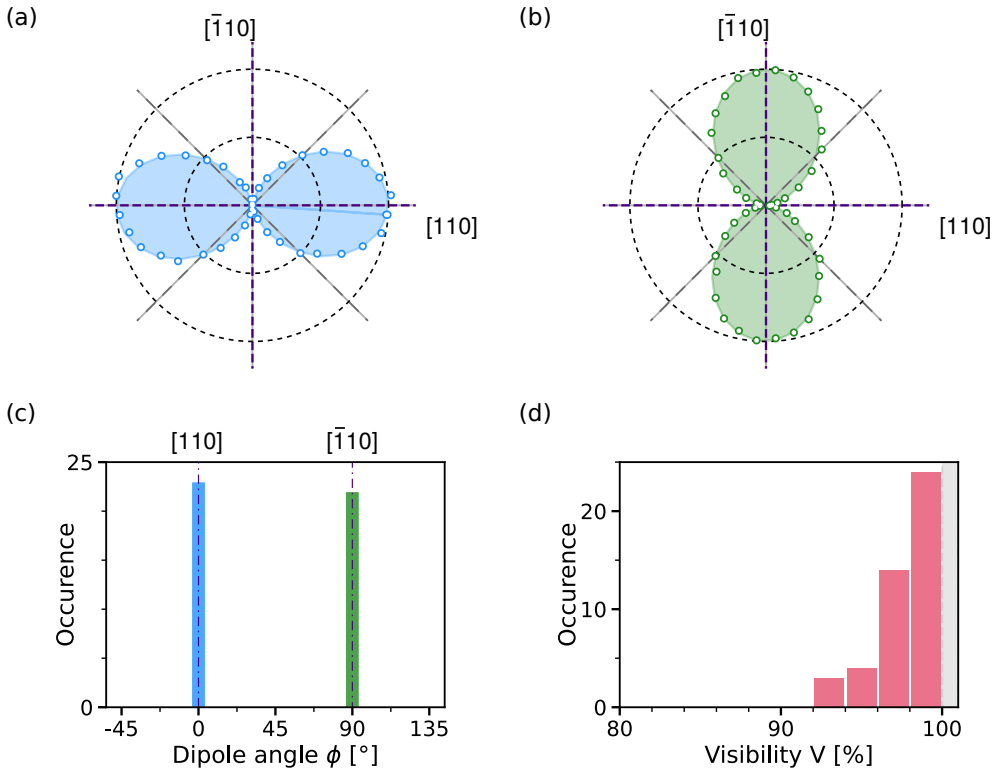


**Figure 4.10:** Polarization of the single photons emitted by W centres. (a,b) Emission polarization diagrams recorded on two individual W defects (blue and green markers). The 0 and 90° directions match the crystal axes [110] and [11$\bar{0}$], respectively. Solid lines are fits using a $\cos^2(\theta)$ function. (c) Histogram of the emission dipole angle $\phi$ and (d) histogram of the visibility V measured on a set of 45 individual W centres.

In order to identify the emission polarization of the W centre, we record the polarization emission diagram of single W centres. Figures 4.10(a,b) show the typical emission polarization diagrams measured on single W centres using the same recording method as in chapter 2. For these 2 single W centres, the visibility V (($I_{max}$ - $I_{min}$) / $I_{max}$) exceeds 96 %. This visibility close to unity indicates linear polarization of the photons, and therefore a single emission dipole [127].

The emission dipole is oriented along either the [110] crystal direction for figure 4.10(a) or the [$\bar{1}$10] crystal direction for figure 4.10(b).

Over a set of 45 individual W centres, a statistical analysis of the emission dipole is performed. The emission dipole angle $\phi$ extracted from the fit using the equation $I(\theta) = I_{max}[Vcos^2(\theta-\phi)+(1-V)]$ (defined in chapter 2) is displayed on figure 4.10(c). On this histogram, we observe that $\phi$ can take only two possible values with equal probability, either 0° or 90° corresponding to the crystal directions [110] and [$\bar{1}$10], respectively. Moreover, by looking at the values of the visibility in figure 4.10(d), we observe that the visibility of the single W centres are almost entirely between 95 % to 100 %. These observations are in agreement with the theoretical calculations that predict a single dipole aligned along the <111> crystal directions for the $I_3$-V defect. After a projection onto the top (001) sample surface, this lead to a projected dipole oriented either along [110] or [$\bar{1}$10] with 50/50 probability. We can conclude that the emission is linearly polarized, consistent with the theoretical predictions [125].

### 4.3.3 Photostability

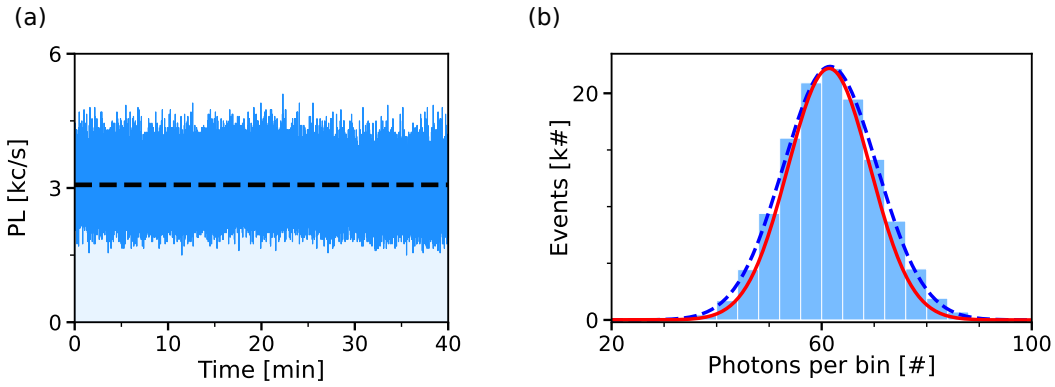


**Figure 4.11:** (a) Typical PL time-trace measured at 30 $\mu$W on a single W defect. The dashed line is the PL intensity mean value. Time bin = 20 ms. (b) Histogram of photons per bin of the PL time trace in (a). The dashed line represents a Gaussian fit of the histogram. The red solid line represents a Poissonian distribution with the mean value of the PL time trace in (a).

For quantum communications, a deterministic single photon source is required to be photostable for on-demand generation of photons. Thus the photostability over time of the W defect is investigated, and a PL time trace recorded on a single W centre is displayed in figure 4.11(a). The PL intensity of single W centres is photostable up to a certain power. Beyond that, photobleaching was observed on some emitters (16 out of the 77 isolated W centres studied) under very high optical power illumination, typically above 500 $\mu$W. Nevertheless, when working at an optical power close to the saturation power (about 2 $\mu$W, see section 4.4.3), photobleaching is unlikely as only 4 defects out of the 77 isolated W centres showed this effect. In contrast, no photoblinking was observed on any of the W centres over days of study, provided the optical power is kept $\leq P_{sat}$. As in chapter 2 and 3, the intensity variations are investigated by plotting the histogram of the photons per bin of the PL time trace displayed in figure 2.12(b). The data

display a Poissonian distribution indicating that the intensity variations of the PL time trace are shot noise limited.

## 4.4 Photodynamics of individual W centres

The study of the photodynamics and its power-dependence will give us new insights on its level structure. The excited state lifetime will be determined in the first section via time-resolved PL measurements. In the second section, the study of the second-order autocorrelation function evolution with the laser power on single W centre will be performed. Finally, in the last section, the saturation curves on single W centres, as well as their temperature dependence will be investigated.

### 4.4.1 Excited state lifetime

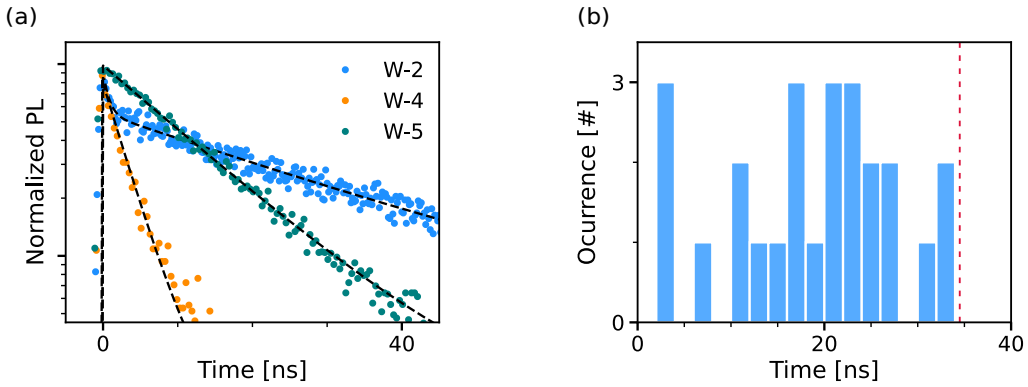


**Figure 4.12:** (a) Time-resolved PL recorded for three W centres under a 150 ps pulsed laser with an excitation wavelength at 532 nm. The data are represented by dotted markers. The excited state lifetime is extracted from data fitting with a single exponential function (dashed lines), which gives, 30.8(3), 12.7(1), and 3.4(1) ns for W-2, W-4, and W-5, respectively. The sharp peak at the beginning of the pulse for W-2 comes from background counts. (b) Histogram of the excited-state lifetime measured on a set of 25 W centres. The red dashed line represents the excited-state lifetime value reported in ensembles in an isotopically purified $^{28}$Si-on-insulator sample [65].

To determine the ES lifetime, time-resolved PL measurements are performed under a 150 ps pulse laser at an excitation wavelength of 532 nm like in the previous chapters. Figure 4.12(a) shows the PL temporal decay of three individual W centres. We observe that the PL follows a mono-exponential decay with a characteristic time constant that varies strongly from one defect to another.

To extract the ES lifetime and quantify the variations, the data are fitted by a single exponential function. The ES lifetime gives 30.8(3), 12.7(1), and 3.4(1) ns for W-2, W-4, and W-5 respectively, showing that it can vary considerably from one defect to another. A statistical analysis performed on 25 W defects reveals ES lifetimes ranging from roughly 3 up to 30 ns, as displayed in figure 4.12(b). On the $3{\times}10^{12}$ Si/cm$^2$ implanted area, the ES lifetime of W centre

ensembles also shows variations from 15(1) to 26(1) ns (at different positions on the sample). All of these lifetimes are under the reported value of 34.5(5) ns measured on ensemble of W centres in an p-type bulk silicon sample [65].

The lifetime fluctuations could be explained by the proximity of the interfaces (surface or oxide interface), as the W centre position in the top 60 nm thick silicon layer of the sample can differ from one defect to another. This effect could be investigated in future works with SOI samples with a thicker top silicon layer for example.

### 4.4.2 Evolution of the $g^2(\tau)$ function with laser power

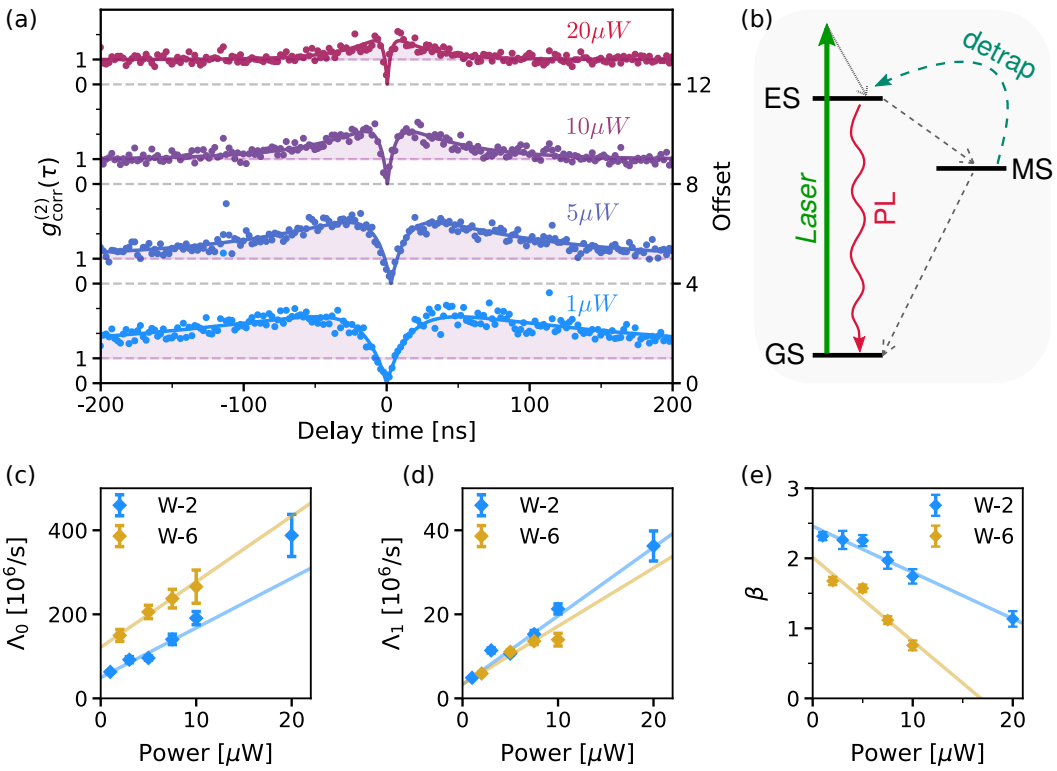


**Figure 4.13:** Second-order autocorrelation measurements versus optical power. (a) Measurements of the $g^2(\tau)$ function on a single W centre with increasing optical power. The solid lines represent data fitting with equation (2.9). (b) Simplified three-level model system of the dynamics of W centres under optical excitation. GS: ground state; ES: excited state; MS: metastable state. Evolution with increasing laser power of (c,d) the antibunching rate $\Lambda_0$ and bunching rate $\Lambda_1$, and (e) the bunching amplitude $\beta$ extracted from the $g^2(\tau)$ data fitting for two W defects. The dashed lines are linear fitting in (c) and a guide-to-the-eye in (d). The error bars correspond to the standard deviation extracted from the data fitting.

Previously, in the initial demonstration of isolated single W centres (figure 4.7(d)), the intensity autocorrelation functions measured a strong bunching ($g^{(2)}(\tau) > 1$), associated with the presence of a non-radiative decay channel through a metastable level [89] (see chapter 2). To further study the dynamics of the defects and to unveil new information on the level structure of

the W centre, the evolution of the $g^{(2)}$ function with optical power is studied on single W centres. In figure 4.13(a), a reduction of the bunching amplitude by increasing the excitation power is observed. This effect has already been observed on individual G* defects [21], and it could be related to a detrapping mechanism transferring populations from the metastable state back to the excited state, as depicted on figure 4.13(b). For fluorescent defects in semiconductors, such as color centers in diamond [89,128] or in silicon carbide [129], this bunching amplitude is often observed to increase with the optical excitation power, with no detrapping mechanism observed.

In order to model our defect, we consider the three-level system presented in chapter 2 (figure 2.10(b)) on which we add a transition rate $\Gamma_{32}$ from $|3\rangle$ to $|2\rangle$ to fit our data. With this additional rate, we obtain the same equation (2.9) [21, 128]. The data are well described by this model, and the three parameters $\beta$, $\Lambda_0$ and $\Lambda_1$ are displayed in figure 4.13(c,d,e) as a function of the optical power for two single W centres. Both rates $\Lambda_0$ and $\Lambda_1$ evolve linearly with the optical power. This behaviour is explained by the acceleration of the photon emission dynamics [89]. In the zero-power limit, the rate $\Lambda_0$ should tend to the inverse of the excited level lifetime of the defect [89]. A linear fit $a \times P + b$ is used to extract this value, and we find 37(17) ns and 8(1) ns for the W-2 and W-6 defect, respectively, as summarized in table 4.2 with the errors being given by the fit. For W-2 defect, the ES lifetime was measured previously at 31(1) ns, in agreement with the value obtained with the $g^{(2)}(\tau)$ measurement (within the error bars). For W-6, this value was not known, showing that this measurement allows the determination of the ES lifetime.

| Center | | W-2 | W-6 |
|---|---|---|---|
| $\Lambda_0$ | a [MHz/$\mu$W] | 11(2) | 15.6(1.4) |
| | 1/b [ns] | 37(17) | 8(1) |
| $\Lambda_1$ | a [MHz/$\mu$W] | 1.6(2) | 1.4(2) |
| | 1/b [ns] | 300(50) | 300(80) |

**Table 4.2:** Fitting parameters $\Lambda_0$ and $\Lambda_1$ for two single W centres extracted from the $g^{(2)}(\tau)$ evolution with laser power. Both rates are fitted with a linear equation $\Lambda = a \times P + b$. At zero power, the inverse rates 1/b correspond to the characteristic times of the excited level and metastable level.

This measurement also allows to estimate the order of magnitude of the characteristic lifetime of the MS by looking at the inverse of $\Lambda_1$ in the zero-power limit. A value of 300 ns was obtained for both defects (see table 4.2), one order of magnitude higher than the ES lifetime. This longer time scale is well illustrated in figure 4.13(a) as the bunching bump is predominant for longer delay time compared to the antibunching dip, implying that the population are trapped in a non-radiative state with a longer lifetime that the ES. The metastable level lifetime could be inferred from future time-resolved PL measurements by varying delay between laser excitation pulses [130]. We remind that the ground state and excited state are spin singlet states, so the question is open whether this metastable could be linked to a spin triplet state populated by an

intersystem crossing.

Lastly, in figure 4.13(e), the amplitude $\beta$ of the bunching effect is represented as a function of the optical power, and fitted by the same linear fit. This bunching amplitude decreases with the optical power, as previously discussed, indicating that less population are being trapped in the MS. This effect may be related to the above bandgap excitation, as the laser provides enough energy to detrap electrons from the metastable state to the conduction band then, back to the excited state, as it was observed in [21]. Linking this parameter to the possible detrapping rates remain to be done, and will require further studies.

### 4.4.3 Saturation curves

In order to estimate the maximum count rates for individual W centres, the PL intensity of single W centres are recorded as a function of the excitation optical power at T=10 K.

#### Defect-dependence saturation curves

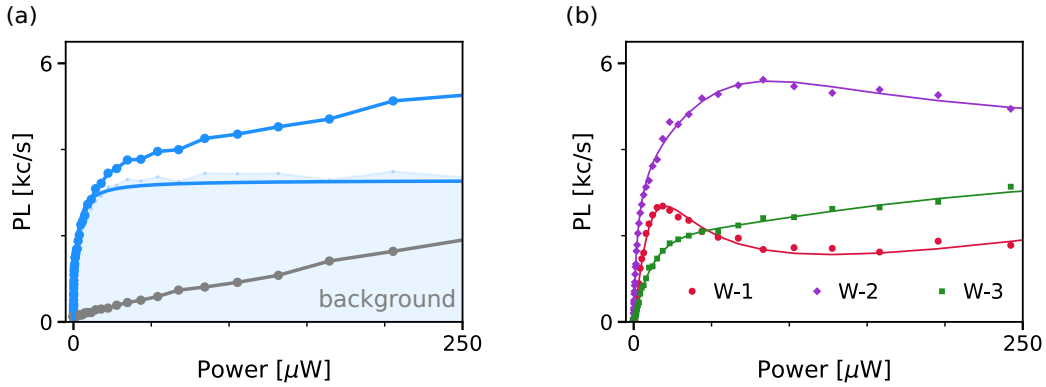


**Figure 4.14:** (a) Saturation curves recorded on single W centres at T=10 K. (b) Saturation curves recorded on three single W centres at T=10 K displaying anomalous behaviour.

The PL intensity evolution of single W centres with optical power differs strongly from one defect to another. Among a data set of 32 individual W defects, 12 presented a standard PL saturation curve (i.e. with a saturation plateau), as observed in the previous two chapters, but for the 20 remaining ones, three typical PL evolutions have been observed at a temperature T=10 K.

*Standard saturation curves*:

The saturation curve of a single W centre displayed in figure 4.14(a) presents a behaviour compatible with the photodynamics of a two-level system, as described in chapter 2. The data are subtracted by the background and fitted using equation (2.12) (solid line in figure 4.14(a)). A saturation power $P_{sat}$ = 1.7 $\mu$W and a saturation intensity $I_{sat}$ = 3.3(1) kc/s are extracted for this single W centre. For the 12 defects with a standard PL saturation curve, the typical PL intensity at saturation reaches between 2 to 6 kcounts/s. These data were acquired by using the detectors with a weak detection efficiency of 10 %. After correction by the different detection

efficiencies, we find that the emission count rates of individual W centres are ≈ 4 to 5 larger that for single G centres.

*Anomalous saturation curves*:

The other two-third of the W centres show anomalous saturation curves with no clear PL saturation. Three typical PL evolutions have been observed and are depicted in figure 4.14(b). On this figure, for the W-2 defect, the PL intensity reaches a maximum and then decreases with optical power. This behaviour was observed on 8 defects. For the W-1 on the contrary, an increase of the PL intensity with optical power is observed without saturation plateau. This evolution was observed on 7 other defects. At last, the W-3 defect exhibits an increase of PL intensity followed by a decrease and it ends with the PL intensity rising again. This W-3 saturation curve was observed on 5 single W centres.

These different power-dependences suggest a coupling of the W centres with a non-radiative state. This state could correspond to another charge or conformation state of the defect, thus explaining the different saturation curves from defect to defect. Then, the transition from the fluorescent form of the W centre to this state would be dependent on the local environment of the defect, and also appears to be affected by the optical power exciting the defect. Coupling with a near non-radiative defect, diverting part of the electronic population of the W centre, could also explain this PL evolution. This non-radiative state differs from the previous metastable state evidenced by the $g^{(2)}$ function, as it is defect dependent, and will be referred by the more general term of dark state (DS).

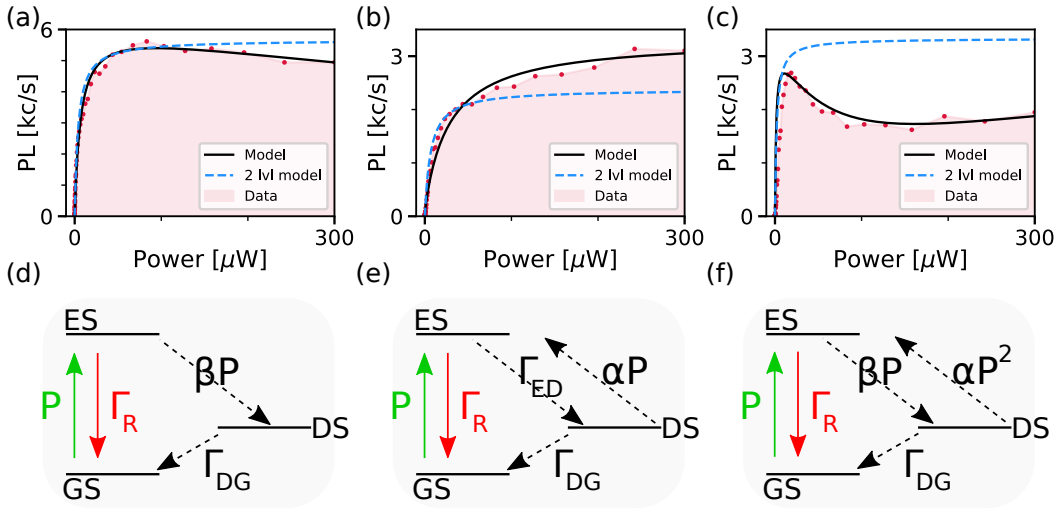


**Figure 4.15:** (a,b,c) Saturation curves obtained from a 3 level system displayed in solid black lines, with the data of the saturation curves on single W centres at T=10 K in dotted red lines. (d,e,f) Schematic of the 3 level system used to simulate the anomalous saturation behaviour of the saturation curves in (a,b,c), respectively, with the rates between the levels being indicated. The solid arrows represent radiative rates and the dashed arrows represent non-radiative rates.

*Simulations*:

To understand the different power-dependences, we model the defect by a 3 level system and we consider the transition rates coming from and going to the dark state to be either constant or linearly-dependent with power, as schematized in figure 4.15(d,e,f). The transition rate between the DS to the GS is fixed to be constant. For the W-1 behaviour, a transition rate linear with power between the ES to the DS depletes the ES, showing a decrease of PL for high powers. For the W-2 behaviour, a constant transition rate between the ES to the DS and a transition rate linear with power between the DS to the ES can reproduce the data. The later linear transition rate repopulates the ES at high power and therefore no saturation is observed. A constant transition rate between the ES to the DS was imposed as letting a linearly power-dependent rate would have been compensated with the rate from DS to the ES, resulting in a behaviour corresponding to a two-level system. For the W-3 behaviour, a more complex model is used to follow the data. A transition rate linear with power between the ES to the DS and a transition rate quadratic with power between the DS to the ES explain (i) a first decrease of the PL due to population being pumped into the dark state for medium power, but (ii) at high power, the squared power rate empties this DS to repopulate the ES resulting in an increase of the PL. We note that a transition rate quadratic with power is equivalent to having an additional level with transition rate linear with power between all the level. Thus this rate quadratic with power may be hinting to a more complex level structure for the W-3 defects.

**Temperature dependence of the saturation curves**

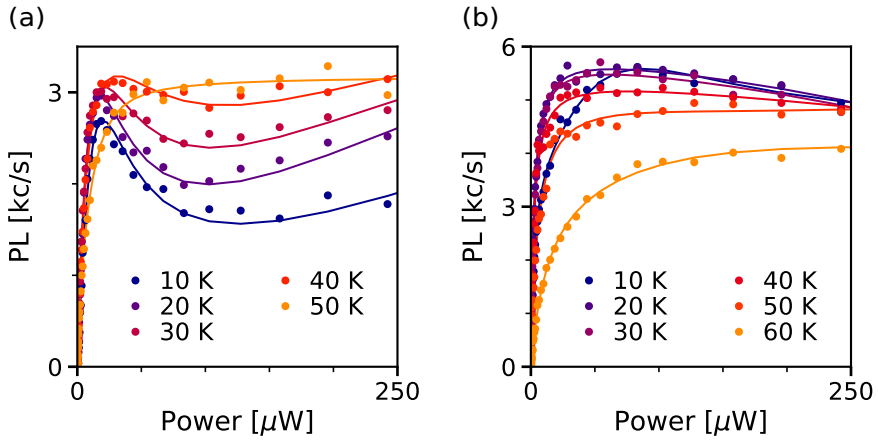


**Figure 4.16:** Saturation curves recorded on single (a) W-3 and (b) W-2 centres for different temperatures.

In addition, the dynamics of coupling of the W centre with the dark state is also temperature dependent. The coupling with the dark state vanishes by increasing the sample temperature. In figure 4.16, we observe that the anomalous saturation curve, clearly visible at T=10 K, gradually revert back to a standard saturation curve at T=50 K. This temperature dependence could indicate that either the non-fluorescent state gets unstable with increasing temperature,

or that the conversion rate into this dark form is inefficient at high temperature. Additional studies are required to fully understand these anomalous PL saturation curves.

## 4.5 Conclusion

The creation by implantation and the isolation of W centres was performed on silicon-on-insulator sample. Single W centres display a bright luminescence with around 40 % of the photons emitted in the ZPL, while the variations of the ZPL energy from one defect to defect remains under 1 meV, inferior by 6 to 20 times to all the previously observed defects in Si. The emitted photons also exhibits a linear polarization, consistent with a <111> single emission dipole. However, the study of saturation curve as well as the excited state lifetime reveals significant variations between defects, associated to a defect-dependant coupling to a dark state. Additionally, the study of the second-order autocorrelation function evolution with the laser power reveals the presence of a trapping state with a lifetime of around 300 ns. This state could be a spin triplet metastable level, but further measurements will be needed to properly identify the nature of this level. Lastly, the power-dependence of the PL intensity presents unusual behaviour evidencing the presence of a dark state potentially linked to a charge or conformation change of the defect. Further research into this dark state will be needed to identify its origin.

# Conclusion

## Summary

This thesis work has been focused on the isolation of optically active defects in silicon, fabricated by ion implantation, for quantum technologies.

In chapter 1, we have presented that silicon, the major semiconductor of the microelectronic industry, can also be used for quantum applications by exploiting electrical spin qubits and photonic qubits. Compare to these systems, optically active point defects in silicon is lagging behind for the development of quantum technologies.

In chapter 2, we have studied a carbon implanted silicon that led to the discovery of seven unidentified single defects in silicon. These defects all emit linearly polarised near-infrared single photons with quantum efficiencies above 10 %, with some even exhibiting emission on the telecom bands. In addition, some defects feature noteworthy properties, such as emission above the liquid nitrogen temperature of 77 K, up to 120 K, or a low dispersion of the emission wavelength.

In chapter 3, we have demonstrated the creation and isolation of G centres in a sample fabricated by a co-implantation method using carbon and proton in a silicon-on-insulator sample. By gradually decreasing the fluence parameters in the implantation, this fabrication method allowed the creation of ensembles down to single emitters. The investigation of single G centres revealed a photostable defect, with a short radiative lifetime of 4.5 ns and a low quantum efficiency of 0.2 %. An unusual effect, that is the reorientation of the defect under optical excitation was also explored via the study of the ZPL fine structure and polarization measurements.

In chapter 4, the isolation of W centres created by silicon-implantation have been demonstrated on silicon-on-insulator sample. Single W centres display a bright PL with linearly-polarized photons and small spread of the emission wavelength. However, the investigation of the saturation curves as well as the excited state lifetimes reveals significant variations between defects, which remains to be explained. In particular, analysing the saturation curves recorded on some W centres has allowed to evidence the coupling to a dark state potentially linked to a charge or conformation change of the defect. A study of the autocorrelation function evolution with the laser power reveals the presence of a metastable state with a lifetime of around 300 ns.

## Outlook

The isolation of point defects in silicon emitting at telecom wavelengths brings numerous prospects for quantum technologies. These defects are promising for the development of silicon-based devices, such as deterministic single photon sources or spin-photon interfaces, with a high capability for large-scale integration. However, the implementation of such devices requires three major conditions: (i) controlling the integration of single defect in nanostructures, (ii) the emission of indistinguishable photons and (iii) the optical spin-control at the single defect scale.

To enable the incorporation of defects in photonic nanostructures, such as waveguides or cavities, the creation of single defects by ion implantation must be improved. The first results on defect integration from our collaboration with Jean-Michel Gérard's team (CEA Grenoble) have enabled to show an enhancement by Purcell effect of the ZPL emission of an ensemble of G centres coupled to a silicon-based ring cavity [111]. The next step will consist in demonstrating a Purcell effect down to the single defect level. This imposes constraints on the creation of defects, such as spatial resolution or conversion yield (i.e. defects creation efficiency). In addition, while the fabrication process of the defects is reproducible, it does not enable yet deterministic defects creation (i.e. the control of the position of the defects), which need to be explored.

Indistinguishable photons are emitted photons that share the same properties (i.e. the same wavelength, the same polarisation and the same temporal and spatial mode, etc). Photon indistinguishability is needed to perform two-photon quantum interference or Hong-Ou-Mandel experiment, which is a key requirement to generate remote entanglement between distant nodes of a quantum network [47]. For solid state emitters, ensuring the emission of indistinguishable photons, or in other words, achieving Fourier transform-limited optical linewidth, is challenging [131]. Indeed, spectral fluctuations (spectral broadening or shift) can emerge from the local environment of the defects, such as local strain or local charge variations [132]. A first solution is to accelerate by Purcell effect the recombination dynamics of defects to make it faster than the environment fluctuations. Another promising solution to overcome this issue has been demonstrated in SiC, where the defects were incorporated into the intrinsic area of a p-i-n junction [51]. Applying a reverse bias allows to deplete the environment of the defect from fluctuating charges that cause random Stark effect on its emission line, thus narrowing the emission lines [51]. Since doping is well controlled in silicon, a similar experiment could be attempted for the defects reported in this thesis.

A spin-photon interface consists of single photons entangled with the spin state. The development of such device is important as, combined with the control of photon indistinguishability, one can achieve entanglement between distant spins using entanglement swapping protocols. Before the realisation of any spin-photon interface, the first step is to demonstrate the coherent control of the spin. There, it is important to have long coherence times. Due to a better isolation from their environment than electronic spins, nuclear spins are an interested quantum resource

as well. Regarding the optical spin-control at the single defect scale, the recent installation of a 3D vector magnet inside the cryostat on the experimental setup will enable to investigate optical detection of the magnetic resonance (ODMR) of the metastable spin triplet of single G defects, that was detected on G ensemble measurements [19, 20]. In addition, the exploration of the metastable state of the W centre with ODMR measurements might reveal non-singlet spin state which, associated with a higher quantum efficiency than the G centre, could be a promising defect for the development of a spin-photon interface.

# Bibliography


[1] Stuart J. Freedman and John F. Clauser. Experimental test of local hidden-variable theories. *Phys. Rev. Lett.*, 28:938–941, Apr 1972.

[2] Alain Aspect, Jean Dalibard, and Gérard Roger. Experimental test of bell's inequalities using time-varying analyzers. *Phys. Rev. Lett.*, 49:1804–1807, Dec 1982.

[3] Richard P. Feynman. Simulating physics with computers. *International Journal of Theoretical Physics*, 21(6):467–488, Jun 1982.

[4] David P. DiVincenzo. The physical implementation of quantum computation. *Fortschritte der Physik*, 48(9-11):771–783, 2000.

[5] Han-Sen Zhong, Hui Wang, Yu-Hao Deng, Ming-Cheng Chen, Li-Chao Peng, Yi-Han Luo, Jian Qin, Dian Wu, Xing Ding, Yi Hu, Peng Hu, Xiao-Yan Yang, Wei-Jun Zhang, Hao Li, Yuxuan Li, Xiao Jiang, Lin Gan, Guangwen Yang, Lixing You, Zhen Wang, Li Li, Nai-Le Liu, Chao-Yang Lu, and Jian-Wei Pan. Quantum computational advantage using photons. *Science*, 370(6523):1460–1463, 2020.

[6] R. Srinivas, S. C. Burd, H. M. Knaack, R. T. Sutherland, A. Kwiatkowski, S. Glancy, E. Knill, D. J. Wineland, D. Leibfried, A. C. Wilson, D. T. C. Allcock, and D. H. Slichter. High-fidelity laser-free universal control of trapped ion qubits. *Nature*, 597(7875):209–213, Sep 2021.

[7] Frank Arute, Kunal Arya, Ryan Babbush, Dave Bacon, Joseph C. Bardin, Rami Barends, Rupak Biswas, Sergio Boixo, Fernando G. S. L. Brandao, David A. Buell, Brian Burkett, Yu Chen, Zijun Chen, Ben Chiaro, Roberto Collins, William Courtney, Andrew Dunsworth, Edward Farhi, Brooks Foxen, Austin Fowler, Craig Gidney, Marissa Giustina, Rob Graff, Keith Guerin, Steve Habegger, Matthew P. Harrigan, Michael J. Hartmann, Alan Ho, Markus Hoffmann, Trent Huang, Travis S. Humble, Sergei V. Isakov, Evan Jeffrey, Zhang Jiang, Dvir Kafri, Kostyantyn Kechedzhi, Julian Kelly, Paul V. Klimov, Sergey Knysh, Alexander Korotkov, Fedor Kostritsa, David Landhuis, Mike Lindmark, Erik Lucero, Dmitry Lyakh, Salvatore Mandrà, Jarrod R. McClean, Matthew McEwen, Anthony Megrant, Xiao Mi, Kristel Michielsen, Masoud Mohseni, Josh Mutus, Ofer Naaman, Matthew Neeley, Charles Neill, Murphy Yuezhen Niu, Eric Ostby, Andre Petukhov, John C. Platt, Chris Quintana, Eleanor G. Rieffel, Pedram Roushan, Nicholas C. Rubin,

Daniel Sank, Kevin J. Satzinger, Vadim Smelyanskiy, Kevin J. Sung, Matthew D. Trevithick, Amit Vainsencher, Benjamin Villalonga, Theodore White, Z. Jamie Yao, Ping Yeh, Adam Zalcman, Hartmut Neven, and John M. Martinis. Quantum supremacy using a programmable superconducting processor. *Nature*, 574(7779):505–510, Oct 2019.

[8] Fabio Ansaloni, Anasua Chatterjee, Heorhii Bohuslavskyi, Benoit Bertrand, Louis Hutin, Maud Vinet, and Ferdinand Kuemmeth. Single-electron operations in a foundry-fabricated array of quantum dots. *Nature Communications*, 11(1):6399, Dec 2020.

[9] M Veldhorst, J C C Hwang, C H Yang, A W Leenstra, B de Ronde, J P Dehollain, J T Muhonen, F E Hudson, K M Itoh, A Morello, and A S Dzurak. An addressable quantum dot qubit with fault-tolerant control-fidelity. *Nature Nanotechnology*, 9(12):981–985, December 2014.

[10] David J. Christle, Abram L. Falk, Paolo Andrich, Paul V. Klimov, Jawad Ul Hassan, Nguyen T. Son, Erik Janzén, Takeshi Ohshima, and David D. Awschalom. Isolated electron spins in silicon carbide with millisecond coherence times. *Nature Materials*, 14(2):160–163, Feb 2015.

[11] Félicien Appas, Othmane Meskine, Aristide Lemaitre, Martina Morassi, Florent Baboux, Maria. I. Amanti, and Sara Ducci. Nonlinear quantum photonics with algaas bragg-reflection waveguides. *Journal of Lightwave Technology*, pages 1–11, 2022.

[12] Valerio Scarani, Helle Bechmann-Pasquinucci, Nicolas J. Cerf, Miloslav Dušek, Norbert Lütkenhaus, and Momtchil Peev. The security of practical quantum key distribution. *Rev. Mod. Phys.*, 81:1301–1350, Sep 2009.

[13] Boris Korzh, Charles Ci Wen Lim, Raphael Houlmann, Nicolas Gisin, Ming Jun Li, Daniel Nolan, Bruno Sanguinetti, Rob Thew, and Hugo Zbinden. Provably secure and practical quantum key distribution over 307 km of optical fibre. *Nature Photonics*, 9(3):163–168, Mar 2015.

[14] B. Hensen, H. Bernien, A. E. Dréau, A. Reiserer, N. Kalb, M. S. Blok, J. Ruitenberg, R. F. L. Vermeulen, R. N. Schouten, C. Abellán, W. Amaya, V. Pruneri, M. W. Mitchell, M. Markham, D. J. Twitchen, D. Elkouss, S. Wehner, T. H. Taminiau, and R. Hanson. Loophole-free bell inequality violation using electron spins separated by 1.3 kilometres. *Nature*, 526(7575):682–686, Oct 2015.

[15] Francesco Priolo, Tom Gregorkiewicz, Matteo Galli, and Thomas F. Krauss. Silicon nanostructures for photonics and photovoltaics. *Nature Nanotechnology*, 9(1):19–32, January 2014. Cited By (since 1996):3 Export Date: 5 May 2014 Source: Scopus.

[16] Daniel B. Higginbottom, Alexander T. K. Kurkjian, Camille Chartrand, Moein Kazemi, Nicholas A. Brunelle, Evan R. MacQuarrie, James R. Klein, Nicholas R. Lee-Hone, Jakub Stacho, Myles Ruether, Camille Bowness, Laurent Bergeron, Adam DeAbreu, Stephen R.

Harrigan, Joshua Kanaganayagam, Danica W. Marsden, Timothy S. Richards, Leea A. Stott, Sjoerd Roorda, Kevin J. Morse, Michael L. W. Thewalt, and Stephanie Simmons. Optical observation of single spins in silicon. *Nature*, 607(7918):266–270, Jul 2022.

[17] Gordon Davies. The optical properties of luminescence centres in silicon. *Physics Reports*, 176(3):83–188, May 1989.

[18] C. Beaufils, W. Redjem, E. Rousseau, V. Jacques, A. Yu. Kuznetsov, C. Raynaud, C. Voisin, A. Benali, T. Herzig, S. Pezzagna, J. Meijer, M. Abbarchi, and G. Cassabois. Optical properties of an ensemble of G-centers in silicon. *Physical Review B*, 97(3):035303, January 2018.

[19] K. M. Lee, K. P. O'Donnell, J. Weber, B. C. Cavenett, and G. D. Watkins. Optical detection of magnetic resonance for a deep-level defect in silicon. *Phys. Rev. Lett.*, 48:37–40, Jan 1982.

[20] K. P. O'Donnell, K. M. Lee, and G. D. Watkins. Origin of the 0.97 eV luminescence in irradiated silicon. *Physica B+C*, 116(1):258–263, 1983.

[21] W. Redjem, A. Durand, T. Herzig, A. Benali, S. Pezzagna, J. Meijer, A. Yu Kuznetsov, H. S. Nguyen, S. Cueff, J.-M. Gérard, I. Robert-Philip, B. Gil, D. Caliste, P. Pochet, M. Abbarchi, V. Jacques, A. Dréau, and G. Cassabois. Single artificial atoms in silicon emitting at telecom wavelengths. *Nature Electronics*, 3(12):738–743, December 2020.

[22] Fumio Shimura. Chapter 3 - basic crystallography. In Fumio Shimura, editor, *Semiconductor Silicon Crystal Technology*, pages 22–81. Academic Press, 1989.

[23] Walid Redjem. *Spectroscopie optique des centres G dans le silicium : des ensembles au centre unique*. PhD thesis, 2019.

[24] W. Bludau, A. Onton, and W. Heinke. Temperature dependence of the band gap of silicon. *Journal of Applied Physics*, 45(4):1846–1848, 1974.

[25] L. Eaves, R.A. Stradling, J.C. Portal, S. Askenazy, R. Barbaste, and K. Hansen. A study of intervalley scattering in n-si by stress-dependent longitudinal magnetophonon resonance. *Solid State Communications*, 15(8):1281–1285, 1974.

[26] J. D. Cuthbert. Recombination kinetics of excitonic molecules and free excitons in intrinsic silicon. *Phys. Rev. B*, 1:1552–1557, Feb 1970.

[27] David J. Lockwood. Chapter 1 light emission in silicon. In David J. Lockwood, editor, *Light Emission in Silicon: From Physics to Devices*, volume 49 of *Semiconductors and Semimetals*, pages 1–35. Elsevier, 1997.

[28] A. D. Zdetsis and C. S. Wang. Lattice dynamics of ge and si using the born-von karman model. *Phys. Rev. B*, 19:2999–3003, Mar 1979.

[29] Martin H. Sadd. Chapter 15 - micromechanics applications. In Martin H. Sadd, editor, *Elasticity (Third Edition)*, pages 465–504. Academic Press, Boston, third edition edition, 2014.

[30] Hans J. Queisser and Eugene E. Haller. Defects in semiconductors: Some fatal, some vital. *Science*, 281(5379):945–950, 1998.

[31] Bahaa E A Saleh and Malvin Carl Teich. *Fundamentals of photonics; 3rd ed.* Wiley series in pure and applied optics. Wiley, New York, NY, 2019.

[32] Mohsen K. Akhlaghi, Ellen Schelew, and Jeff F. Young. Waveguide integrated superconducting single-photon detectors implemented as near-perfect absorbers of coherent radiation. *Nature Communications*, 6(1):8233, Sep 2015.

[33] Jun Yoneda, Kenta Takeda, Tomohiro Otsuka, Takashi Nakajima, Matthieu R Delbecq, Giles Allison, Takumu Honda, Tetsuo Kodera, Shunri Oda, Yusuke Hoshi, Noritaka Usami, Kohei M Itoh, and Seigo Tarucha. A quantum-dot spin qubit with coherence limited by charge noise and fidelity higher than 99.9. *Nat Nanotechnol*, 13(2):102–106, December 2017.

[34] R. Maurand, X. Jehl, D. Kotekar-Patil, A. Corna, H. Bohuslavskyi, R. Laviéville, L. Hutin, S. Barraud, M. Vinet, M. Sanquer, and S. De Franceschi. A cmos silicon spin qubit. *Nature Communications*, 7(1):13575, Nov 2016.

[35] T. F. Watson, S. G. J. Philips, E. Kawakami, D. R. Ward, P. Scarlino, M. Veldhorst, D. E. Savage, M. G. Lagally, Mark Friesen, S. N. Coppersmith, M. A. Eriksson, and L. M. K. Vandersypen. A programmable two-qubit quantum processor in silicon. *Nature*, 555(7698):633–637, Mar 2018.

[36] Stephan G. J. Philips, Mateusz T. Madzik, Sergey V. Amitonov, Sander L. de Snoo, Maximilian Russ, Nima Kalhor, Christian Volk, William I. L. Lawrie, Delphine Brousse, Larysa Tryputen, Brian Paquelet Wuetz, Amir Sammak, Menno Veldhorst, Giordano Scappucci, and Lieven M. K. Vandersypen. Universal control of a six-qubit quantum processor in silicon. *Nature*, 609(7929):919–924, Sep 2022.

[37] A. M. J. Zwerver, T. Krähenmann, T. F. Watson, L. Lampert, H. C. George, R. Pillarisetty, S. A. Bojarski, P. Amin, S. V. Amitonov, J. M. Boter, R. Caudillo, D. Correas-Serrano, J. P. Dehollain, G. Droulers, E. M. Henry, R. Kotlyar, M. Lodari, F. Lüthi, D. J. Michalak, B. K. Mueller, S. Neyens, J. Roberts, N. Samkharadze, G. Zheng, O. K. Zietz, G. Scappucci, M. Veldhorst, L. M. K. Vandersypen, and J. S. Clarke. Qubits made by advanced semiconductor manufacturing. *Nature Electronics*, 5(3):184–190, Mar 2022.

[38] A. Crippa, R. Ezzouch, A. Aprá, A. Amisse, R. Laviéville, L. Hutin, B. Bertrand, M. Vinet, M. Urdampilleta, T. Meunier, M. Sanquer, X. Jehl, R. Maurand, and S. De Franceschi.

Gate-reflectometry dispersive readout and coherent control of a spin qubit in silicon. *Nature Communications*, 10(1):2776, Jul 2019.

[39] Y. He, S. K. Gorman, D. Keith, L. Kranz, J. G. Keizer, and M. Y. Simmons. A two-qubit gate between phosphorus donor electrons in silicon. *Nature*, 571(7765):371–375, Jul 2019.

[40] Juha T. Muhonen, Juan P. Dehollain, Arne Laucht, Fay E. Hudson, Rachpon Kalra, Takeharu Sekiguchi, Kohei M. Itoh, David N. Jamieson, Jeffrey C. McCallum, Andrew S. Dzurak, and Andrea Morello. Storing quantum information for 30 seconds in a nanoelectronic device. *Nature Nanotechnology*, 9(12):986–991, Dec 2014.

[41] Andrea Morello, Jarryd J. Pla, Patrice Bertet, and David N. Jamieson. Donor spins in silicon for quantum technologies. *Advanced Quantum Technologies*, 3(11):2000005, 2020.

[42] Serwan Asaad, Vincent Mourik, Benjamin Joecker, Mark A. I. Johnson, Andrew D. Baczewski, Hannes R. Firgau, Mateusz T. Madzik, Vivien Schmitt, Jarryd J. Pla, Fay E. Hudson, Kohei M. Itoh, Jeffrey C. McCallum, Andrew S. Dzurak, Arne Laucht, and Andrea Morello. Coherent electrical control of a single high-spin nucleus in silicon. *Nature*, 579(7798):205–209, Mar 2020.

[43] Richard E. George, Wayne Witzel, H. Riemann, N. V. Abrosimov, N. Nötzel, Mike L. W. Thewalt, and John J. L. Morton. Electron spin coherence and electron nuclear double resonance of bi donors in natural si. *Phys. Rev. Lett.*, 105:067601, Aug 2010.

[44] Takashi Kobayashi, Joseph Salfi, Cassandra Chua, Joost van der Heijden, Matthew G. House, Dimitrie Culcer, Wayne D. Hutchison, Brett C. Johnson, Jeff C. McCallum, Helge Riemann, Nikolay V. Abrosimov, Peter Becker, Hans-Joachim Pohl, Michelle Y. Simmons, and Sven Rogge. Engineering long spin coherence times of spin–orbit qubits in silicon. *Nature Materials*, 20(1):38–42, Jan 2021.

[45] Xiaogang Qiang, Xiaoqi Zhou, Jianwei Wang, Callum M. Wilkes, Thomas Loke, Sean O'Gara, Laurent Kling, Graham D. Marshall, Raffaele Santagati, Timothy C. Ralph, Jingbo B. Wang, Jeremy L. O'Brien, Mark G. Thompson, and Jonathan C. F. Matthews. Large-scale silicon quantum photonics implementing arbitrary two-qubit processing. *Nature Photonics*, 12(9):534–539, Sep 2018.

[46] R. Narkowicz, M.R. Siegrist, Ph. Moreau, J.P. Hogge, R. Raguotis, and R. Brazis. Third-Order Susceptibility of Silicon Crystals Measured with Millimeter-Wave Gyrotron. *Acta Physica Polonica A*, 119(4):509–513, April 2011.

[47] Pierre Aboussouan, Olivier Alibart, Daniel B. Ostrowsky, Pascal Baldi, and Sébastien Tanzilli. High-visibility two-photon interference at a telecom wavelength using picosecond-regime separated sources. *Phys. Rev. A*, 81:021801, Feb 2010.

[48] A. L. Migdall, D. Branning, and S. Castelletto. Tailoring single-photon and multiphoton probabilities of a single-photon on-demand source. *Phys. Rev. A*, 66:053805, Nov 2002.

[49] Joshua W. Silverstone, Damien Bonneau, Jeremy L. O'Brien, and Mark G. Thompson. Silicon quantum photonics. *IEEE Journal of Selected Topics in Quantum Electronics*, 22(6):390–402, 2016.

[50] J R Maze, A Dréau, V Waselowski, H Duarte, J-F Roch, and V Jacques. Free induction decay of single spins in diamond. *New Journal of Physics*, 14(10):103041, oct 2012.

[51] Christopher P. Anderson, Alexandre Bourassa, Kevin C. Miao, Gary Wolfowicz, Peter J. Mintun, Alexander L. Crook, Hiroshi Abe, Jawad Ul Hassan, Nguyen T. Son, Takeshi Ohshima, and David D. Awschalom. Electrical and optical control of single spins integrated in scalable semiconductor devices. *Science*, 366(6470):1225–1230, 2019.

[52] Mihika Prabhu, Carlos Errando-Herranz, Lorenzo De Santis, Ian Christen, Changchen Chen, and Dirk R. Englund. Individually addressable artificial atoms in silicon photonics, 2022.

[53] I. Gross, W. Akhtar, V. Garcia, L. J. Martínez, S. Chouaieb, K. Garcia, C. Carrétéro, A. Barthélémy, P. Appel, P. Maletinsky, J.-V. Kim, J. Y. Chauleau, N. Jaouen, M. Viret, M. Bibes, S. Fusil, and V. Jacques. Real-space imaging of non-collinear antiferromagnetic order with a single-spin magnetometer. *Nature*, 549(7671):252–256, Sep 2017.

[54] Roya Maboudian, Carlo Carraro, Debbie G. Senesky, and Christopher S. Roper. Advances in silicon carbide science and technology at the micro- and nanoscales. *Journal of Vacuum Science & Technology A*, 31(5):050805, 2013.

[55] Chunming Yin, Milos Rancic, Gabriele G. de Boo, Nikolas Stavrias, Jeffrey C. McCallum, Matthew J. Sellars, and Sven Rogge. Optical addressing of an individual erbium ion in silicon. *Nature*, 497(7447):91–94, May 2013.

[56] Milos Rancic, Morgan P. Hedges, Rose L. Ahlefeldt, and Matthew J. Sellars. Coherence time of over a second in a telecom-compatible quantum memory storage material. *Nature Physics*, 14(1):50–54, Jan 2018.

[57] Mark A. Hughes, Naitik A. Panjwani, Matias Urdampilleta, Nafsika Theodoropoulou, Ilana Wisby, Kevin P. Homewood, Ben Murdin, Tobias Lindström, and J. David Carey. Coupling of erbium-implanted silicon to a superconducting resonator. *Phys. Rev. Applied*, 16:034006, Sep 2021.

[58] Lorenz Weiss, Andreas Gritsch, Benjamin Merkel, and Andreas Reiserer. Erbium dopants in nanophotonic silicon waveguides. *Optica*, 8(1):40–41, Jan 2021.

[59] Hisashi Sumikura, Eiichi Kuramichi, Hideaki Taniyama, and Masaya Notomi. Ultrafast spontaneous emission of copper-doped silicon enhanced by an optical nanocavity. *Scientific Reports*, 4(1):5040, May 2014.

[60] Adam DeAbreu, Camille Bowness, Rohan J.S. Abraham, Alzbeta Medvedova, Kevin J. Morse, Helge Riemann, Nikolay V. Abrosimov, Peter Becker, Hans-Joachim Pohl, Michael L.W. Thewalt, and Stephanie Simmons. Characterization of the Si:se$^+$ spin-photon interface. *Phys. Rev. Applied*, 11:044036, Apr 2019.

[61] Kevin J. Morse, Rohan J. S. Abraham, Adam DeAbreu, Camille Bowness, Timothy S. Richards, Helge Riemann, Nikolay V. Abrosimov, Peter Becker, Hans-Joachim Pohl, Michael L. W. Thewalt, and Stephanie Simmons. A photonic platform for donor spin qubits in silicon. *Science Advances*, 3(7):e1700930, 2017.

[62] B. J. Coomer, J. P. Goss, R. Jones, S. Öberg, and P. R. Briddon. Interstitial aggregates and a new model for the I1/W optical centre in silicon. *Physica B: Condensed Matter*, 273-274:505–508, 1999.

[63] P. A. Stolk, H.-J. Gossmann, D. J. Eaglesham, D. C. Jacobson, C. S. Rafferty, G. H. Gilmer, M. Jaraíz, J. M. Poate, H. S. Luftman, and T. E. Haynes. Physical mechanisms of transient enhanced dopant diffusion in ion-implanted silicon. *J. Appl. Phys.*, 81(9):6031–6050, May 1997.

[64] B.C. MacEvoy and S.J. Watts. Defect Engineering Radiation Tolerant Silicon Detectors. *Solid State Phenomena*, 57-58:221–232, July 1997.

[65] Sonia M. Buckley, Alexander N. Tait, Galan Moody, Bryce Primavera, Stephen Olson, Joshua Herman, Kevin L. Silverman, Satyavolu Papa Rao, Sae Woo Nam, Richard P. Mirin, and Jeffrey M. Shainline. Optimization of photoluminescence from W centers in silicon-on-insulator. *Opt. Express*, 28(11):16057–16072, May 2020.

[66] S. Hayama, G. Davies, and K. M. Itoh. Photoluminescence studies of implantation damage centers in Si30. *J. Appl. Phys.*, 96(3):1754–1756, July 2004. Publisher: American Institute of Physics.

[67] Iván Santos, María Aboy, Pedro López, Luis A. Marqués, and Lourdes Pelaz. Insights on the atomistic origin of X and W photoluminescence lines inc-Si fromab initiosimulations. *J. Phys. D: Appl. Phys.*, 49(7):075109, 2016.

[68] L. W. Song, X. D. Zhan, B. W. Benson, and G. D. Watkins. Bistable interstitial-carbon–substitutional-carbon pair in silicon. *Phys. Rev. B*, 42:5765–5783, Sep 1990.

[69] Sylvain G. Cloutier, Chih-Hsun Hsu, and Jimmy Xu. Directly-pumped all-silicon laser. In *Integrated Photonics Research and Applications/Nanophotonics*, page NWC1. Optica Publishing Group, 2006.

[70] C. Chartrand, L. Bergeron, K. J. Morse, H. Riemann, N. V. Abrosimov, P. Becker, H.-J. Pohl, S. Simmons, and M. L. W. Thewalt. Highly enriched $^{28}\mathrm{Si}$ reveals remarkable optical linewidths and fine structure for well-known damage centers. *Physical Review B*, 98(19):195201, November 2018.

[71] G. Bohnert, K. Weronek, and A. Hangleiter. Transient characteristics of isoelectronic bound excitons at hole-attractive defects in silicon: The c(0.79 ev), p(0.767 ev), and h(0.926 ev) lines. *Phys. Rev. B*, 48:14973–14981, Nov 1993.

[72] A. N. Safonov, E. C. Lightowlers, Gordon Davies, P. Leary, R. Jones, and S. Öberg. Interstitial-carbon hydrogen interaction in silicon. *Phys. Rev. Lett.*, 77:4812–4815, Dec 1996.

[73] L. Bergeron, C. Chartrand, A. T. K. Kurkjian, K. J. Morse, H. Riemann, N. V. Abrosimov, P. Becker, H.-J. Pohl, M. L. W. Thewalt, and S. Simmons. Silicon-Integrated Telecommunications Photon-Spin Interface. *PRX Quantum*, 1(2):020301, October 2020.

[74] Michael Hollenbach, Yonder Berencén, Ulrich Kentsch, Manfred Helm, and Georgy V. Astakhov. Engineering telecom single-photon emitters in silicon for scalable quantum photonics. *Optics Express*, 28(18):26111–26121, August 2020.

[75] Alrik DURAND. *Single optically active defects in semiconductors for quantum technologies: From the NV center in diamond to single defects in silicon.* PhD thesis, 2021.

[76] Martin A. Green and Mark J. Keevers. Optical properties of intrinsic silicon at 300 k. *Progress in Photovoltaics: Research and Applications*, 3(3):189–192, 1995.

[77] Vincent Jacques. *Source de photons uniques et interferences a un seul photon. De l'experience des fentes d'Young au choix retarde.* Theses, École normale supérieure de Cachan - ENS Cachan, November 2007.

[78] Alexios Beveratos. *Réalisation expérimentale d'une source de photons uniques par fluorescence de centres colorés individuels dans le diamant ; application à la cryptographie quantique.* Theses, Université Paris Sud - Paris XI, December 2002. Jury : Izo Abram (Rapporteur) Nicolas Gisin Jean-Pierre Goedgebuer (Predsident) Philippe Grangier Jean-Philippe Poizat Jean-Francois Roch (Rapporteur).

[79] C. C Gerry and Peter Knight. *Introductory quantum optics.* Cambridge University Press, Cambridge, 2006.

[80] L. J. Martínez, T. Pelini, V. Waselowski, J. R. Maze, B. Gil, G. Cassabois, and V. Jacques. Efficient single photon emission from a high-purity hexagonal boron nitride crystal. *Physical Review B*, 94(12):121405, September 2016.

[81] A. Durand, Y. Baron, W. Redjem, T. Herzig, A. Benali, S. Pezzagna, J. Meijer, A. Yu. Kuznetsov, J.-M. Gérard, I. Robert-Philip, M. Abbarchi, V. Jacques, G. Cassabois, and A. Dréau. Broad Diversity of Near-Infrared Single-Photon Emitters in Silicon. *Physical Review Letters*, 126(8):083602, February 2021.

[82] James F. Ziegler. SRIM-2003. *Nuclear Instruments and Methods in Physics Research Section B: Beam Interactions with Materials and Atoms*, 219-220:1027–1036, June 2004.

[83] Cyrus E. Dreyer, Audrius Alkauskas, John L. Lyons, Anderson Janotti, and Chris G. Van de Walle. First-Principles Calculations of Point Defects for Quantum Technologies. *Annual Review of Materials Research*, 48(1):1–26, 2018.

[84] C. E. Jones and W. D. Compton. Recombination luminescence in irradiated silicon-effects of uniaxial stress and temperature variations †. *Radiation Effects*, 9(1-2):83–88, May 1971.

[85] K. Thonke, A. Teschner, and R. Sauer. New photoluminescence defect spectra in silicon irradiated at 100 K: Observation of interstitial carbon? *Solid State Communications*, 61(4):241–244, January 1987.

[86] Peter Pichler. *Intrinsic Point Defects, Impurities, and Their Diffusion in Silicon*. Computational Microelectronics. Springer-Verlag, Wien, 2004.

[87] S. K. Estreicher, D. West, J. Goss, S. Knack, and J. Weber. First-Principles Calculations of Pseudolocal Vibrational Modes: The Case of Cu and Cu Pairs in Si. *Physical Review Letters*, 90(3):035504, January 2003.

[88] M. D. Eisaman, J. Fan, A. Migdall, and S. V. Polyakov. Invited Review Article: Single-photon sources and detectors. *Review of Scientific Instruments*, 82(7):071101, July 2011.

[89] A. Beveratos, S. Kühn, R. Brouri, T. Gacoin, J.-P. Poizat, and P. Grangier. Room temperature stable single-photon source. *The European Physical Journal D - Atomic, Molecular, Optical and Plasma Physics*, 18(2):191–196, February 2002.

[90] A. Beveratos, R. Brouri, J.-P. Poizat, and P. Grangier. Bunching and Antibunching from Single NV Color Centers in Diamond. In Paolo Tombesi and Osamu Hirota, editors, *Quantum Communication, Computing, and Measurement 3*, pages 261–267. Springer US, Boston, MA, 2002.

[91] V. D. Tkachev and A. V. Mudryi. Piezospectroscopic effect on zero-phonon luminescence lines of silicon. *Journal of Applied Spectroscopy*, 29(6):1485–1491, December 1978.

[92] A. Sipahigil, K. D. Jahnke, L. J. Rogers, T. Teraji, J. Isoya, A. S. Zibrov, F. Jelezko, and M. D. Lukin. Indistinguishable Photons from Separated Silicon-Vacancy Centers in Diamond. *Physical Review Letters*, 113(11):113602, September 2014.

[93] R. J. Elliott, I. G. Matthew, and E. W. J. Mitchell. The polarization of luminescence in diamond. *Philosophical Magazine*, 3(28):360–369, April 1958.

[94] Lorenz Weiss, Andreas Gritsch, Benjamin Merkel, and Andreas Reiserer. Erbium dopants in silicon nanophotonic waveguides. *arXiv:2005.01775 [physics, physics:quant-ph]*, May 2020. arXiv: 2005.01775.

[95] E. M. Purcell, H. C. Torrey, and R. V. Pound. Resonance Absorption by Nuclear Magnetic Moments in a Solid. *Physical Review*, 69(1-2):37–38, January 1946.

[96] G. K. Wertheim. Energy Levels in Electron-Bombarded Silicon. *Physical Review*, 105(6):1730–1735, March 1957.

[97] G. Bemski. Paramagnetic Resonance in Electron Irradiated Silicon. *Journal of Applied Physics*, 30(8):1195–1198, August 1959.

[98] G. D. Watkins, J. W. Corbett, and R. M. Walker. Spin Resonance in Electron Irradiated Silicon. *Journal of Applied Physics*, 30(8):1198–1203, August 1959.

[99] K. Thonke, H. Klemisch, J. Weber, and R. Sauer. New model of the irradiat(aion-induced 0.97-eV ($G$) line in silicon: A ${\mathrm{C}}_{S}\ensuremath{-}{\mathrm{Si}}^{*}$ complex. *Physical Review B*, 24(10):5874–5886, November 1981.

[100] L. S. Vlasenko, Yu. V. Martynov, T. Gregorkiewicz, and C. A. J. Ammerlaan. Electron paramagnetic resonance versus spin-dependent recombination: Excited triplet states of structural defects in irradiated silicon. *Phys. Rev. B*, 52:1144–1151, Jul 1995.

[101] L. T. Canham, K. G. Barraclough, and D. J. Robbins. 1.3-um light-emitting diode from silicon electron irradiated at its damage threshold. *Applied Physics Letters*, 51(19):1509–1511, November 1987.

[102] Efraim Rotem, Jeffrey M. Shainline, and Jimmy M. Xu. Enhanced photoluminescence from nanopatterned carbon-rich silicon grown by solid-phase epitaxy. *Applied Physics Letters*, 91(5):051127, July 2007.

[103] A. Docaj and S. K. Estreicher. Three carbon pairs in Si. *Physica B: Condensed Matter*, 407(15):2981–2984, August 2012.

[104] H. Wang, A. Chroneos, C. A. Londos, E. N. Sgourou, and U. Schwingenschlögl. G-centers in irradiated silicon revisited: A screened hybrid density functional theory approach. *Journal of Applied Physics*, 115(18):183509, May 2014.

[105] Dilyara Timerkaeva, Claudio Attaccalite, Gilles Brenet, Damien Caliste, and Pascal Pochet. Structural, electronic, and optical properties of the C-C complex in bulk silicon from first principles. *Journal of Applied Physics*, 123(16):161421, March 2018.

[106] Péter Udvarhelyi, Bálint Somogyi, Gerg ő Thiering, and Adam Gali. Identification of a telecom wavelength single photon emitter in silicon. *Phys. Rev. Lett.*, 127:196402, Nov 2021.

[107] P. Becker, H.-J. Pohl, H. Riemann, and N. Abrosimov. Enrichment of silicon for a better kilogram. *physica status solidi (a)*, 207(1):49–66, 2010.

[108] Kamyar Saeedi, Stephanie Simmons, Jeff Z. Salvail, Phillip Dluhy, Helge Riemann, Nikolai V. Abrosimov, Peter Becker, Hans-Joachim Pohl, John J. L. Morton, and Mike L. W. Thewalt. Room-Temperature Quantum Bit Storage Exceeding 39 Minutes Using Ionized Donors in Silicon-28. *Science*, 342(6160):830–833, November 2013.

[109] V. Mazzocchi, P. G. Sennikov, A. D. Bulanov, M. F. Churbanov, B. Bertrand, L. Hutin, J. P. Barnes, M. N. Drozdov, J. M. Hartmann, and M. Sanquer. 99.992% $^{28}$Si CVD-grown epilayer on 300 mm substrates for large scale integration of silicon spin qubits. *Journal of Crystal Growth*, 509:1–7, March 2019.

[110] Dilla D. Berhanuddin, Manon A. Lourenço, Russell M. Gwilliam, and Kevin P. Homewood. Co-Implantation of Carbon and Protons: An Integrated Silicon Device Technology Compatible Method to Generate the Lasing G-Center. *Advanced Functional Materials*, 22(13):2709–2712, 2012.

[111] B. Lefaucher, J. B. Jager, V. Calvo, A. Durand, Y. Baron, F. Cache, V. Jacques, I. Robert-Philip, G. Cassabois, T. Herzig, J. Meijer, S. Pezzagna, M. Khoury, M. Abbarchi, A. Dréau, and J. M. Gérard. Cavity-enhanced zero-phonon emission from an ensemble of g centers in a silicon-on-insulator microring. 2022.

[112] C P Foy, M C do Carmo, G Davies, and E C Lightowlers. Uniaxial stress measurements on the 0.97 eV line in irradiated silicon. *Journal of Physics C: Solid State Physics*, 14(1):L7–L12, January 1981.

[113] Gordon Davies, Shusaku Hayama, Leonid Murin, Reinhard Krause-Rehberg, Vladimir Bondarenko, Asmita Sengupta, Cinzia Davia, and Anna Karpenko. Radiation damage in silicon exposed to high-energy protons. *Phys. Rev. B*, 73(16):165202, April 2006.

[114] B. Surma, P. Kaminski, A. Wnuk, and R. Kozlowski. Some new photoluminescence features of W line for neutron-irradiated MCz-Si and FZ-Si. In *2008 IEEE Nuclear Science Symposium Conference Record*, pages 2561–2564, October 2008.

[115] Ms Skolnick, Ag Cullis, and Hc Webber. Defect photoluminescence from Si laser annealed over a wide temperature range. *Journal of Luminescence*, 24-25:39–42, November 1981.

[116] Jiming Bao, Malek Tabbal, Taegon Kim, Supakit Charnvanichborikarn, James S. Williams, Michael J. Aziz, and Federico Capasso. Point defect engineered Si sub-bandgap light-emitting diode. *Opt. Express*, 15(11):6727–6733, May 2007.

[117] Sonia Buckley, Jeffrey Chiles, Adam N. McCaughan, Galan Moody, Kevin L. Silverman, Martin J. Stevens, Richard P. Mirin, Sae Woo Nam, and Jeffrey M. Shainline. All-silicon light-emitting diodes waveguide-integrated with superconducting single-photon detectors. *Appl. Phys. Lett.*, 111(14):141101, October 2017.

[118] A. N. Tait, S. M. Buckley, J. Chiles, A. N. McCaughan, S. Olson, S. Papa Rao, S. W. Nam, R. P. Mirin, and J. M. Shainline. Microring resonator-coupled photoluminescence from silicon W centers. *J. Phys. Photonics*, 2(4):045001, July 2020.

[119] G. Davies, E. C. Lightowlers, and Z. E. Ciechanowska. The 1018 meV (W or I1) vibronic band in silicon. *J. Phys. C: Solid State Phys.*, 20(2):191–205, January 1987.

[120] R. Jones, T. A. G. Eberlein, N. Pinho, B. J. Coomer, J. P. Goss, P. R. Briddon, and S. Öberg. Self-interstitial clusters in silicon. *Nuclear Instruments and Methods in Physics Research Section B: Beam Interactions with Materials and Atoms*, 186(1):10–18, 2002.

[121] M. Gharaibeh, S. K. Estreicher, and P. A. Fedders. Molecular-dynamics studies of self-interstitial aggregates in Si. *Physica B: Condensed Matter*, 273-274:532–534, 1999.

[122] Giorgia M. Lopez and Vincenzo Fiorentini. Structure, energetics, and extrinsic levels of small self-interstitial clusters in silicon. *Phys. Rev. B*, 69(15):155206, April 2004.

[123] A. Carvalho, R. Jones, J. Coutinho, and P. R. Briddon. Density-functional study of small interstitial clusters in Si: Comparison with experiments. *Phys. Rev. B*, 72(15):155208, October 2005.

[124] D. A. Richie, Jeongnim Kim, Stephen A. Barr, Kaden R. A. Hazzard, Richard Hennig, and John W. Wilkins. Complexity of Small Silicon Self-Interstitial Defects. *Phys. Rev. Lett.*, 92(4):045501, January 2004.

[125] Yoann Baron, Alrik Durand, Péter Udvarhelyi, Tobias Herzig, Mario Khoury, Sébastien Pezzagna, Jan Meijer, Isabelle Robert-Philip, Marco Abbarchi, Jean-Michel Hartmann, Vincent Mazzocchi, Jean-Michel Gérard, Adam Gali, Vincent Jacques, Guillaume Cassabois, and Anaïs Dréau. Detection of single w-centers in silicon. *ACS Photonics*, 9(7):2337–2345, Jul 2022.

[126] Kay D Jahnke, Alp Sipahigil, Jan M Binder, Marcus W Doherty, Mathias Metsch, Lachlan J Rogers, Neil B Manson, Mikhail D Lukin, and Fedor Jelezko. Electron–phonon processes of the silicon-vacancy centre in diamond. *New J. Phys.*, 17(4):043011, April 2015.

[127] Clotilde Lethiec, Julien Laverdant, Henri Vallon, Clémentine Javaux, Benoît Dubertret, Jean-Marc Frigerio, Catherine Schwob, Laurent Coolen, and Agnès Maître. Measurement of Three-Dimensional Dipole Orientation of a Single Fluorescent Nanoemitter by Emission Polarization Analysis. *Phys. Rev. X*, 4(2):021037, May 2014.

[128] Elke Neu, Mario Agio, and Christoph Becher. Photophysics of single silicon vacancy centers in diamond: implications for single photon emission. *Optics Express*, 20(18):19956–19971, August 2012.

[129] F. Fuchs, B. Stender, M. Trupke, D. Simin, J. Pflaum, V. Dyakonov, and G. V. Astakhov. Engineering near-infrared single-photon emitters with optically active spins in ultrapure silicon carbide. *Nature Communications*, 6(1):7578, Jul 2015.

[130] Lucio Robledo, Hannes Bernien, Toeno van der Sar, and Ronald Hanson. Spin dynamics in the optical cycle of single nitrogen-vacancy centres in diamond. *New Journal of Physics*, 13(2):025013, feb 2011.

[131] Brahim Lounis and Michel Orrit. Single-photon sources. *Reports on Progress in Physics*, 68(5):1129–1179, April 2005.

[132] Lucio Robledo, Hannes Bernien, Ilse van Weperen, and Ronald Hanson. Control and Coherence of the Optical Transition of Single Nitrogen Vacancy Centers in Diamond. *Physical Review Letters*, 105(17):177403, October 2010.

# Abstract

The second quantum revolution, which began in the 1980s, aims to exploit the properties of quantum mechanics to design and build innovative devices. Optically active point defects in semiconductors are one of the studied quantum systems and have the particular feature of behaving like artificial atoms in the solid state. This implies that, isolated on an individual scale, they exhibit single photon emission that can be used for quantum communications. In addition, some defects have a detectable and controllable electronic or nuclear spin state that can be used as a quantum memory or sensor. Silicon is the main semiconductor of the electronics industry and the ideal platform for large scale nanofabrication of quantum circuits. However, fluorescent defects in this low-bandgap semiconductor have been little studied for quantum applications, with the first isolation of an optically active defect only recently reported.

The study of these defects initially focused on the G centre, a carbon-based defect, which exhibits photoluminescence emission in the wavelengths used in optical fibre telecommunications, and has a non-zero spin state that can be exploited for quantum technologies. In this context, carbon-implanted silicon samples were explored, not only ensuring the creation and detection of single G centres, but also revealing multiple unidentified individual fluorescent defects emitting in the near infrared. Alongside this exploration, silicon-implanted samples were analysed, allowing the first isolation of the W centre, an intrinsic defect in silicon. On these different emitters, optical spectroscopy studies coupled with single photon emission analysis have revealed properties not accessible by ensemble measurements.

The observation of individual defects embedded within silicon on insulator wafers opens the possibility of exploring defect-based quantum technologies in silicon, such as integrated quantum photonics and quantum communications. The next step would be to demonstrate control of the spin states, which could lead to the development of an efficient spin-photon interface operating at the telecommunications wavelength.

# Résumé

La deuxième révolution quantique, née dans les années 1980, vise à exploiter les propriétés de la mécanique quantique pour concevoir et construire des dispositifs innovants. Les défauts ponctuels optiquement actifs dans les semiconducteurs font partie des systèmes quantiques étudiés et ont la particularité de se comporter comme des atomes artificiels à l'état solide. Cela implique que, isolés à l'échelle individuelle, ils présentent une émission de photons uniques qui peut être utilisée pour les communications quantiques. De plus, certains défauts présentent un état de spin électronique ou nucléaire détectable et contrôlable qui peut être utilisé comme mémoire ou capteur quantique. Le silicium est le principal semiconducteur de l'industrie électronique et la plateforme idéale pour la nanofabrication à grande échelle de circuits quantiques. Cependant, les défauts luminescents de ce semiconducteur à faible bande interdite ont été peu étudiés pour les applications quantiques, avec le premier isolement d'un défaut optiquement actif n'ayant été rapporté que récemment.

L'étude de ces défauts s'est d'abord concentrée sur le centre G, un défaut à base de carbone, qui présente une émission de photoluminescence aux longueurs d'onde utilisées dans les télécommunications par fibre optique, et possède un état de spin non nul qui peut être exploité pour les technologies quantiques. Dans ce contexte, des échantillons de silicium implantés en carbone ont été explorés, assurant non seulement la création et la détection de centres G uniques, mais révélant également de multiples défauts fluorescents individuels non identifiés émettant dans le proche infrarouge. Parallèlement à cette exploration, des échantillons de silicium implanté ont été analysés, permettant la première isolation du centre W, un défaut intrinsèque du silicium. Sur ces différents émetteurs, des études de spectroscopie optique couplées à l'analyse de l'émission de photons uniques ont révélé des propriétés non accessibles par des mesures d'ensemble.

L'observation de défauts individuels intégrés dans des plaquettes de silicium sur isolant ouvre la possibilité d'explorer les technologies quantiques basées sur les défauts dans le silicium, telles que la photonique quantique intégrée et les communications quantiques. Une prochaine étape consisterait à démontrer le contrôle des états de spin, ce qui pourrait conduire au développement d'une interface spin-photon efficace fonctionnant à la longueur d'onde des télécommunications.